EXPERIMENTS AND MODELING OF A TURBULENT JET IGNITION SYSTEM FOR INTERNAL COMBUSTION ENGINES

By

Masumeh Gholamisheeri

A DISSERTATION

Submitted to
Michigan State University
in partial fulfillment of the requirements
for the degree of

Mechanical Engineering-Doctor of Philosophy

2017

ABSTRACT

EXPERIMENTS AND MODELING OF A CONTROLLED TURBULENT JET IGNITION SYSTEM FOR INTERNAL COMBUSTION ENGINES

By

Masumeh Gholamisheeri

This thesis experimentally, computationally and analytically examines the transient jet used to ignite combustible mixtures during Turbulent Jet Ignition (TJI). The TJI system is a prechamber initiated combustion enhancement system that can be used in place of a spark plug in a spark ignition (SI) engine. In TJI the ignition source, which originates in the prechamber, enters the main chamber through a connecting nozzle(s) as a transient high temperature jet of reacted mixture, reacting mixture and active radicals. TJI is capable of enabling low temperature combustion, through either lean or dilute combustion.

For this work, TJI experiments were performed in an optically accessible Rapid Compression Machine (RCM). High speed visualization was performed via an SA4 high speed color camera and the images were compared with Computational Fluid Dynamics (CFD) modeling results. Comparison was also made between the experimental and numerical pressure data.

A significant portion of this work is dedicated to the CFD modeling of the TJI process and for the first time a theoretical study of the jet flow field, density gradients, turbulence intensity, and temperature fields in both the prechamber and the main chamber was performed. The influences of nozzle size and mixture stoichiometry on jet penetration speed and combustion performance were investigated. Experiments were completed for turbulent jet ignition system orifice diameters of 2.0, 2.5 and 3.0 mm each at lean-to-stoichiometric equivalence ratios of ϕ =0.67, 0.8 and 1.0. The hot jet velocity at the orifice exit was calculated, for the first time, using mathematical correlations. The Mach number and Reynolds number were also computed. The high speed

imaging shows the influence of orifice diameter on flame propagation and the shape and structure of vortices resulting from the turbulent jet. Results revealed a direct relationship between orifice exit area reduction and a decrease in hot jet penetration speed. There was also a reduction in hot jet penetration speed with an increase in the equivalence ratio. Moreover, the jet was turbulent with calculated Reynolds numbers of around 20,000 or greater. Normalized transient results are presented that produce good agreement between the various model predictions. A discussion is provided of a new correlation model for the transient TJI process.

In a separate set of experiments, the impact of an auxiliary fueled prechamber on the burn rate and on the lean or dilute limit extension of the RCM was investigated. Nitrogen was used as the diluent and the nitrogen dilution limit was found to be 35% of system mass. Both experimental and numerical results confirmed the idea of combustion enhancement of diluted mixtures by the prechamber auxiliary injection events.

To model the turbulent jet of the TJI system, Reynolds Averaged Navier-Stokes (RANS) and Large Eddy Simulation (LES) turbulence models and the SAGE chemistry solver were used. To determine the effect of mechanism reduction, the pressure traces were computed using four (4) comprehensive chemical kinetic mechanisms (San Diego, Aramco, GRI, and NUI) and one (1) reduced chemical kinetic mechanism, which are all compared with the experimental pressure data. Results indicate that none of the mechanisms are in complete agreement, however they are in good agreement with the experimental burn rate, peak pressure and ignition delay predictions. The numerical iso-surface temperature contours (1200, 800, 2000, and, 2400 K) were obtained which enable 3-D views of the flame propagation, the jet discharge, the ignition and extinction events, and the heat release process.

To my Mother and my Father I am so much of what I learned from you Thank you endlessly

ACKNOWLEDGEMENTS

When I came to the United States, I would not imagine the incredible prosperity and growth I will experience during my PhD research and by living in the US which turned to be my second home.

I started my PhD research under the supervision of Dr. Elisa Toulson, and I was very lucky to have an understanding, helpful, compassionate, optimistic and knowledgeable advisor as her. Without her insight, I would never been able to complete this thesis.

Also, I am very grateful for having Dr. Gerald Gentz and Bryce Thelen the senior graduate students as my mentors and friends who I could share difficult, stressful and also enjoyable and happy moments of graduate life with. I was very lucky to have a chance to know them and I greatly appreciate their friendship.

I would like to thank my PhD committee members, Prof. Indrek Wichman for his contribution in my research, my publications, countless revisions to the papers we have written together and his wise lifetime advices and Prof. Harold Schock for his guidance, providing constructive feedbacks and career advice, and also Dr. Denis Miller for his insightful evaluation and his time.

I would also like to acknowledge the invaluable contribution and support of many other people in the department. They include Thomas Stuecken, Kevin Moran and Brian Rowley for their excellent technical assistance in experimental part of this research.

My greatest appreciation goes to my parents and my family who supported me over the years and helped me to recognize my potentials. Without their love and motivation, I would not be able to chase my dreams. My sisters and brothers deserve my wholehearted thanks as well.

Saving the most important for last I would like to sincerely thank my best friend and my life partner, Saleh Rezaeiravesh, for his endless love, patience and encouragement throughout my entire study. Saleh was the first one who passionately thought me how to do research and for this, I am indebted to him my PhD. Most importantly, he opened my eyes to so many beauties in life, the beauty of love, care, endeavor and hope. Thank you for your immeasurable sacrifice, your patient ear and quiet understanding and your affection and love.

TABLE OF CONTENTS

LIST OF TABLES	X
LIST OF FIGURES	xi
Chapter 1 Introduction	1
1-1 Turbulent Jet Ignition System	2
1-2 Research Questions and Objectives	4
Chapter 2 Literature Review	6
2-1 Ignition Processes	6
2-2 Turbulent Combustion	8
2-3 Lean Burn Combustion	10
2-4 Turbulent Jet Ignition System	13
2-5 Round Turbulent Jet	24
2-6 Numerical Modeling Background	30
Chapter 3 Experimental Set-up	37
3-1 Combustion Visualization and High Speed Imaging	40
Chapter 4 Numerical Procedure	42
4-1 Turbulent Transport	44
4-2 Computational Grid	50
4-3 Combustion Modeling	52
4-4 Mechanism Reduction	53
4-5 Monitor Points	55
4-6 Simulation Geometry	56
Chapter 5 CFD Modeling of a Methane Fueled Turbulent Jet Ignition System v Dilution in a Rapid Compression Machine	
5-1 Results	60
5-2 Chapter Summary	71
Chapter 6 Study of the Physics of a Premixed, Variable Inlet Density and Flow Confined Turbulent Jet	
6-1 Theory	76

6-1-1 Correlation I: Laminar Jet Analysis [131] and Inverse Ratio Correlation	76
6-1-2 Correlation II: Similarity Analysis, [86]	78
6-1-3 Correlation III: Non-Vaporizing Spray Penetration Correlation, [74]	79
6-2 Results	80
6-2-1 Jet Penetration Illustration	83
6-2-2 Penetration Speed Measurements	86
6-2-3 Orifice Exit Velocity Estimation	93
6-3 Chapter Summary	96
Chapter 7 Theoretical Study of Turbulent Jet Flow Field in a Methane Fueled Turbulent Ignition System	
7-1 Theory	100
7-1-1 Generalized TJI Injection Model Derived From First Principles	100
7-2 Results	101
7-2-1 Pressure Traces	101
7-2-2 Hot Jet and Flow Velocity	105
7-2-3 Line-of-Sight Penetration Measurements	109
7-2-4 Orifice Exit Velocity Estimation	112
7-2-5 Pressure Normalization	114
7-3 Chapter Summary	118
Chapter 8 RANS Modeling of a Homogeneously Charged Turbulent Jet Ignition S	•
0.4.75 - 1	
8-1 Results	
8-2 Chapter Summary	133
Chapter 9 LES Modeling of a Homogeneously Charged Turbulent Jet Ignition Sys	stem 135
9-1 Results	136
9-2 Chapter Summary	147
Chapter 10 Summary and Concluding Remarks	150
10-1 Recommendations for Future Work	156
APPENDICES	158
Appendix A Uncertainty Analysis	159

В	BIBLIOGRAPHY	166
	Appendix D Crevice Volume Effect	104
	Appendix C Integrated Heat Release	163
	Appendix B Laminar Flame Speed Calculation	162

LIST OF TABLES

Table 3-1- RCM experimental set-up	40
Table 5-1 Test specifications.	61
Table 6-1- Experimental images of hot jet penetration into the main chamber for various orifice diame (d=2.0, 2.5, 3.0 mm) at a constant equivalence ratio condition (ϕ =0.8)	
Table 6-2- Experimental images of hot jet penetration into the main chamber for various equivalence ratios (ϕ =1.0, 0.8, 0.67) for an orifice diameter of 2.5 mm.	
Table D 1- Unburned mass and pressure rise results.	164

LIST OF FIGURES

Figure 1-1- Schematic picture of the TJI (isometric view on the right) and the initial jet as it enters the main chamber (front view on the left).
Figure 2-1- Calculated (line) and measured (points) ignition delay times in hydrocarbon-air mixtures [34].
Figure 2-2- Typical Three-Way-Catalyst plot vs. air-fuel ratio [50]
Figure 2-3- Schlieren records of Single Orifice PJC systems, orifice diameter=2.5 mm [59]
Figure 2-4- Schlieren records of a single orifice PJC systems, orifice diameters: a&b: 6 mm; c&d: 4 mm [59]
Figure 2-5- Section view image of a Turbulent Jet Igniter centrally installed in the test engine's four valve, pent roof combustion system [31]
Figure 2-6- Detailed images of the Turbulent Jet Ignition prechamber and nozzle in the 4-valve pent roof combustion system [31].
Figure 2-7- Turbulent jet plume structures, 1- stretch and extinction of intense shear zone, 2- large scale vortices, 3- entrainment process [59]
Figure 2-8- Sectioned view of the PPJB, with significant features labeled [70]23
Figure 2-9- Schematic description of a jet penetrating a fluid at rest. The virtual origin is located at x=0, 5d/2 upstream from the nozzle exit plane [73]
Figure 3-1- Schematic of RCM test facility
Figure 3-2- Cross sectional view of RCM combustion cylinder with TJI installed. a) No injector installed, b) Dual-Mode TJI
Figure 3-3- Optical set-up for color imaging. Imaging is end-on
Figure 4-1- Energy spectrum decomposition, associated with the Reynolds Averaged Numerical Simulation from Sagaut 1998 [94]
Figure 4-2- Energy spectrum decomposition, associated with Large Eddy Simulation. From Sagaut 1998 [94]. Compare with Figure 4-1
Figure 4-3- An example of generated grid with fixed embedding at the spark event
Figure 4-4- An example of generated grid with adaptive mesh refinement near the flame boundary during combustion
Figure 4-5- Location of the monitor points in the main chamber
Figure 4-6- Cavity geometry of RCM combustion chamber and TJI system assembly, generated in SolidWorks Left (end-on-view); right (3/4 view)

Figure 4-7- Surface file of RCM combustion chamber plus TJI system
Figure 4-8- Piston motion function used to define the piston location at each time step. TDC is afterward at 31 msec.
Figure 4-9- Clip plane location used for the simulation contours passing through the pre and main chambers and the nozzles
Figure 5-1- Experimental traces of the main chamber mean pressures
Figure 5-2- Numerical traces of the main chamber mean pressure. The projected pressure losses are shown in dashed lines. (The progress of numerical simulations were run up to the completion of combustion and did not include the entire heat loss process)
Figure 5-3- Optical images achieved during the experimental tests compared to the OH radical mass fraction contours of the simulation for λ =1.0 and no N_2 dilution.
Figure 5-4- OH radical mass fraction contours of the simulation for λ =1.0 and 20% N_2 dilution65
Figure 5-5- Optical images achieved during the experimental tests compared to the OH radical mass fraction contours of the simulation for λ =1.0 and 35% N_2 dilution
Figure 5-6- Optical images achieved during the experimental tests compared to the OH radical mass fraction contours of the simulation for λ =1.0 and 40% N_2 dilution with 4% auxiliary air/fuel injection in the prechamber
Figure 5-7- Turbulent kinetic energy contours of the simulations for λ =1.0, a comparison between various diluted mixtures.
Figure 6-1- Close-up view of TJI with nozzles installed
Figure 6-2- Recorded pressure traces in both pre and main chambers together with the spark trigger signal for the 3.0 mm orifice at ϕ =0.8. The inlay shows images of the locations of the jet. The images correspond to the time sequence of Table 7-1. (t=0.1 ms, t=0.25)
Figure 6-3- Jet tip penetration speed versus normalized jet penetration length at φ=0.8
Figure 6-4- Jet tip penetration speed and normalized jet penetration length versus time at ϕ =0.8, here, D is the main chamber bore.
Figure 6-5- Dependence of jet penetration length on time, (a) short ($s=t$), and (b) long ($s=t1/2$), limits, for $\phi = 0.8$. Note that correlation (a) remains linear throughout but correlation (b) breaks down as time increases and the hot jet approaches the opposite wall90
Figure 6-6- Jet tip penetration speed versus normalized jet penetration length for all nine cases. Here, <i>D</i> is the main cylinder bore.
Figure 6-7- Jet tip penetration speed versus x/d (d is the nozzle diameter) for three nozzle diameters at ϕ =0.893
Figure 6-8- Jet exit velocity based on various correlations for three nozzle diameters at ϕ =0.8. None of the three correlations is consistently accurate over the entire range of the data

Figure 7-1- A comparison between the simulation and experimental pressure traces for a nozzle diameter=3.0 mm at λ =1.25
Figure 7-2- A comparison between all simulation and experimental pressure results for λ = 1.25103
Figure 7-3- A comparison between the simulation pressure with five mechanisms and the experiment. Here the nozzle diameter=3.0 mm and λ = 1.25
Figure 7-4- A comparison between the simulations at various lambda values (λ =1.0, 1.25 and 1.5) and experimental pressures for λ =1.25 and d=3.0 mm
Figure 7-5- RANS simulation of time-dependent velocity profile at each monitor point over the span of the jet impingement period, d= 2.5 mm, $\lambda=1.25$
Figure 7-6- Time-dependent velocity profile at monitor points over the span of the jet impingement period, for all nozzle configurations, $\lambda=1.25$.
Figure 7-7- Schematic of the spherical monitor point in the domain
Figure 7-8- Velocity and mass flow rate variation at the nozzle throat for orifice diameters of d=2.0, 2.5 and 3.0, λ = 1.25
Figure 7-9- Modeling and experimental line-of-sight penetration speed and normalized penetration location of the reacting jet versus time
Figure 7-10- Jet exit velocity based on Control Volume correlation compared to the modeling results for three nozzle diameters at λ =1.25
Figure 7-11- Normalized exit velocity versus normalized time. A comparison between Control Volume analysis and modeling which shows that the normalized experiment and simulation trends are similar. 113
Figure 7-12- Location of the start of combustion and peak pressure for experimental and numerical pressure traces.
Figure 7-13- Comparison between the simulation's temperature contours and the experimental chemiluminescence images at similar burn duration times. Nozzle diameter=3.0 mm, λ = 1.25116
Figure 7-14- Comparison between the simulation's temperature contours and the experimental chemiluminescence images at similar burn duration times. Nozzle diameter=2.5 mm, λ = 1.25117
Figure 7-15- Comparison between the simulation's temperature contours and the experimental chemiluminescence images at similar burn duration times. Nozzle diameter= 2.0 mm , $\lambda = 1.25117$
Figure 8-1- A comparison between all the RANS simulation and experiment's pressure results, λ =1.25. Note that the deviation of the simulations and experiments becomes large in the active combustion stage, where the pressure rises to its peak value
Figure 8-2- A comparison between all the RANS simulation and experiment's pressure results, λ =1.25 in compression (left) and combustion (right) stages.
Figure 8-3- A comparison between RANS simulation pressures of pre and main chambers and experimental measurements, nozzle diameter=3.0 mm and λ =1.25

Figure 8-4- A comparison between main chamber LES simulation pressure and experimental measurements, nozzle diameter= 2.0 mm and $\lambda=1.25$.
Figure 8-5- Experimental 0-10% and 10-90% burn durations, λ =1.25
Figure 8-6- Normalized combustion period pressure plots, indicating similarity of the normalized profiles
Figure 8-7- Comparison between the RANS simulations temperature contours and the experimental chemiluminescence images at similar burn duration times. $d=3.0 \text{ mm}$, $\lambda=1.25$
Figure 8-8- Comparison between the RANS simulations temperature contours and the experimental chemiluminescence images at similar burn duration times. $d=2.5$ mm, $\lambda=1.25$
Figure 8-9- Comparison between the RANS (third row) and LES (second row) simulations temperature contours and the experimental chemiluminescence images (first row) at similar burn duration times. $d=2.0$ mm, $\lambda=1.25$.
Figure 8-10- Comparison between the simulation's turbulent kinetic energy contours at similar burn duration times, λ =1.25.
Figure 8-11- Comparison between the simulation's turbulent dissipation rate contours at similar burn duration times, λ =1.25
Figure 9-1- Pressure trace comparison between experimental measurements and numerical simulations, $\lambda=1.0$.
Figure 9-2- Pressure trace comparison between experimental measurements and numerical simulations, $\lambda=1.25$.
Figure 9-3- Isometric view of three clip planes showing their placement relative to each other
Figure 9-4- Chemiluminescence images of combustion (1st row) and LES temperature and mid-range isosurface contours (2nd, 3rd and 4th rows, respectively), $d=2.0$ mm, at $\lambda=1.25$
Figure 9-5- Chemiluminescence images of combustion (1st row) and LES temperature and mid-range isosurface contours (2nd, 3rd and 4th rows, respectively), $d=2.5$ mm, at $\lambda=1.25$
Figure 9-6- Chemiluminescence images of combustion (1st row) and LES temperature and mid-range isosurface contours (2nd, 3rd and 4th rows, respectively), d=3.0 mm, at λ =1.25
Figure 9-7- Combustion completion and heat release process illustrated with iso-surface contours, d=2.0 mm, λ =1.25.
Figure 9-8- OH mass fraction contours for d=2.0, 2.5 and 3.0 mm, from top to the bottom, respectively, at λ =1.25.
Figure B-1- Methane Laminar Flame Speed at λ=1.25 and compressed temperature of 750 K
Figure C-1- Integrated heat release curve from RANS simulation

KEY TO ABBREVIATIONS

AFR Air-Fuel Ratio

AKTIM Arc and Kernel Tracking Ignition Model

AMR Adaptive Mesh Refinement

BD Burn Duration

BDC Bottom Dead Center

CAD Computer-Aided Design

CFD Computational Fluid Dynamics

CFL Courant-Friedrichs Lewy

CFM Coherent Flame Model

CH* Methylidyne Radical

CO Carbon Monoxide

CO₂ Carbon Dioxide

CV Control Volume

Da Damköhler Number

DISC Direct Injection Stratified Charge

DI-SI Direct Injection-Spark Ignition

DNS Direct Numerical Simulation

DRGEPSA Direct Relation Graph with Error Propagation and Sensitivity Analysis

EGR Exhaust Gas Recirculation

EOI End Of Injection

HAJI Hydrogen Assisted Jet Ignition

HPCC High Performance Computing Center

HC Hydrocarbon

HCN Hydrogen Cyanide, (Prussic Acid)

H₂O Hydrogen Monoxide

H₂O₂ Hydrogen Peroxide

JPIC Jet Plume Injection Combustion

LAG Lavinnia Aktyvatsia Gorenia (Avalanche Activated Combustion)

LDA Laser Doppler Anemometry

LES Large Eddy Simulation

LFS Laminar Flame Speed

LIF Laser Induced Fluorescence

LPG Liquefied Petroleum Gas

LTC Low Temperature Combustion

NOx Oxides of Nitrogen

N₂O Nitrous Oxide

NO Nitric Oxide

N₂ Nitrogen

NIF Near and Intermediate Field

O₂ Oxygen

OH* Hydroxyl Radical

PDF Probability Density Function

PISO Pressure Implicit with Splitting of Operator

PIV Particle Image Velocimetry

PJC Pulsed Jet Combustion

PPJB Piloted Premixed Jet Burner

RANS Reynolds Averaged Navier Stokes

RCM Rapid Compression Machine

Re Reynolds Number

RNG Re-Normalization Group Theory

SI Spark Ignition

STL STereoLithography

TJI Turbulent Jet Ignition

TDC Top Dead Center

TCI Turbulent Chemistry Interaction

TKE Turbulent Kinetic Energy

TWC Three-Way Catalytic

UDF User Defined Function

UHC Unburned Hydrocarbons

λ Relative Air-to Fuel Ratio: Actual/Stoichiometric

 ϕ (1/ λ) Fuel-Air Equivalence Ratio

Chapter 1 Introduction

Increases in engine efficiency and decreases in pollutant emissions are two main concerns of the automotive industry for several reasons. The first reason is fuel costs and the desire to reduce foreign oil dependency. The second reason is regulations for emissions such as unburned hydrocarbons, carbon monoxide and nitrogen oxides. Based on the limitations mentioned, improvements in engine combustion are challenging. This encourages new technologies such as low temperature combustion (LTC) strategies that promise to increase thermal efficiency while decreasing pollution. In lean burn processes, fuel is burned with excess air, which has many advantages over conventional stoichiometric combustion [1]. Excess air reduces the combustion temperature which leads to lower NOx emissions because nitrogen oxidizes at high temperatures [2]. In addition, the use of excess air in engine operation enables reduced throttling compared to stoichiometric operation, reducing pumping losses. With lean combustion, the flame temperature decreases because of the lower reactant concentration and the higher specific heat of the combustion products. Dilution of the fuel-air mixture with exhaust gas recirculation (EGR) has a similar effect on flame temperature, playing the role of a heat sink for the heat of combustion [1, 3-5]. Despite all of the advantages of lean combustion, it is incompatible with three-way catalyst operation, where stoichiometric operation is required. However, the development of lean burn NOx emission control technologies increases interest in lean burn technologies [1, 6-8].

Maintaining combustion stability with lean or dilute combustion strategies can be more difficult to achieve with fuels that have narrow flammability limits. Combustion instability leads to increased HC emissions and reduces the laminar flame speed of lean mixtures. As a result, it affects flame kernel growth and flame propagation. Consequently, ignition enhancement techniques in

which additional ignition energy or distributed ignition sources are used, are of great interest [1, 9, 10].

Combustion enhancement systems for spark ignited engines have been studied for decades, with reviews written by Dale and Oppenheim [9] and Dale et al. [11]. Enhanced ignition systems include technologies such as microwave spark ignition [12], plasma-assisted ignition, [13, 14], divided chamber stratified charge [15] and prechamber ignition systems. Among all of these prechamber ignition systems, Turbulent Jet Ignition (TJI) is of great interest because it can enable low temperature combustion, through both lean and/or dilute combustion.

1-1 Turbulent Jet Ignition System

The TJI system is a prechamber initiated combustion enhancement system that can be used in place of a spark plug in a spark ignition (SI) engine. The prechamber is a small volume chamber where an injector and spark plug, or an alternative ignition system, are located. This prechamber is connected to the main combustion chamber through either one or multiple small orifices. The combustion that initiates in this prechamber increases the mixture pressure, which is the necessary driving force for the flow of gases from the prechamber into the main chamber. The entrained turbulent jet increases the turbulence and mixing rate in the main chamber and as a result, the dilute fuel-air mixture in the main chamber has a higher chance of igniting through the action of spatially distributed ignition sites. The unsteady turbulent jet plays the dominant role in combustion duration, flame propagation and burn rate. Figure 1-1 shows a schematic of the TJI assembly (cross sectional isometric view) and the front view of the initial jet as it enters into the main chamber.

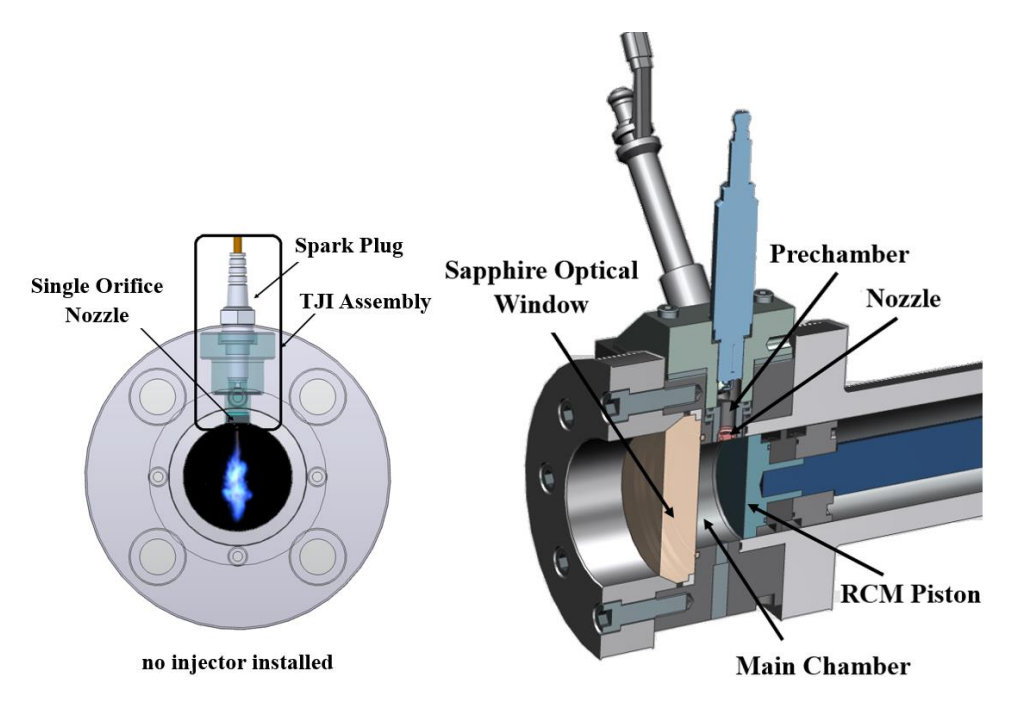


Figure 1-1- Schematic picture of the TJI (isometric view on the right) and the initial jet as it enters the main chamber (front view on the left).

Once the initial flame kernel develops in the prechamber, a part of the unburned charge is forced into the main combustion chamber thereby increasing the turbulence of the flow field. Ignition of the main chamber charge starts when the jet penetrates into the main chamber acting as a distributed energy source. All of the design parameters of TJI system such as prechamber size and shape, number of orifices and orifice cross sectional area are important to the jet structure and hence, they affect combustion. The prechamber size and orifice diameter were examined in several studies [16-18] and it was determined that if the orifice diameter was too small, (d<1 mm), the jet was not capable of igniting lean mixtures in the main chamber. In addition, smaller orifices, although having greater jet penetration, experienced higher heat losses [1]. The commonly used orifice diameters for prechamber ignition systems in general and TJI systems in particular are in the range of 1-4 mm [1, 19]. Murase and Hanada [16] showed that the faster pressure rise is attainable with the smaller orifice diameter (~2.5 mm compared to 4 mm) which greatly enhances the combustion process.

Since the discharging jet has variable jet density and flow rate, analysis of the jet structure and calculation of the Reynolds and Mach number is challenging and system optimization greatly depends on consideration of all effective parameters.

1-2 Research Questions and Objectives

Although TJI has been investigated over many years and broad experimental and computational studies have been performed [1, 19-32], many research questions remained unanswered. The work presented here can be divided into two categories, (1) analytical considerations of the jet flow structure and (2) numerical modeling of the turbulent jet and its comparison with the experimental results. Some major research questions are as follows;

- 1- What are the orifice diameter and equivalence ratio effects on the turbulent jet structure as it enters into the main chamber? How do they influence the flame propagation, burning rate, entrainment rate, and hence combustion enhancement?
- 2- How is the turbulent jet characterized using the flow characteristic parameters such as the Reynolds number and Mach number?
- 3- How many flow regions does the jet experience as it travels toward the main chamber end wall. Does it become fully developed?
- 4- Does any correlation exist in the literature to estimate the nozzle exit velocity, since the velocity measurement is not viable in the main chamber?
- 5- How accurately does the numerical modeling predict the combustion process? What is the difference between the reduced and full chemical kinetic mechanisms?
- 6- What are the values of turbulent intensity, density, temperature and important intermediate species concentrations, in the main and prechamber?

7- What is the impact of auxiliary fueling of the prechamber on the burn rate, and on the lean/dilute limit extension of the RCM?

The goal of the work presented in this thesis is to answer the above questions while enhancing the scientific knowledge of the ignition process in the Turbulent Jet Ignition system.

Chapter 2 Literature Review

2-1 Ignition Processes

Ignition, a time dependent process, starts with reactants and evolves toward the formation of a steady flame. Some examples of ignition include induced ignition in gasoline engines, auto ignition in diesel engines and photo-ignition, which is caused by photolytic generation of radicals [33]. Two parameters related to the ignition are minimum ignition energy and ignition delay time.

Although the amount of fuel consumed and hence the released energy is small during the ignition delay time period, the radical pool population increases at an exponential rate. Thus, the temperature remains nearly constant [33]. When the radical pool becomes sufficiently large, it consumes a fraction of the fuel releasing thermal energy allowing ignition to take place. Many criteria influence the definition of induction time such as consumption of fuel, formation of CO and OH, and the increase of pressure and temperature. Figure 2-1 shows the ignition delay time of several hydrocarbons and their exponential dependence on the reciprocal temperature (τ =A exp(+B/T)), which reflects the temperature dependence (Arrhenius law) of the underlying elementary reactions occurring during the induction period [33].

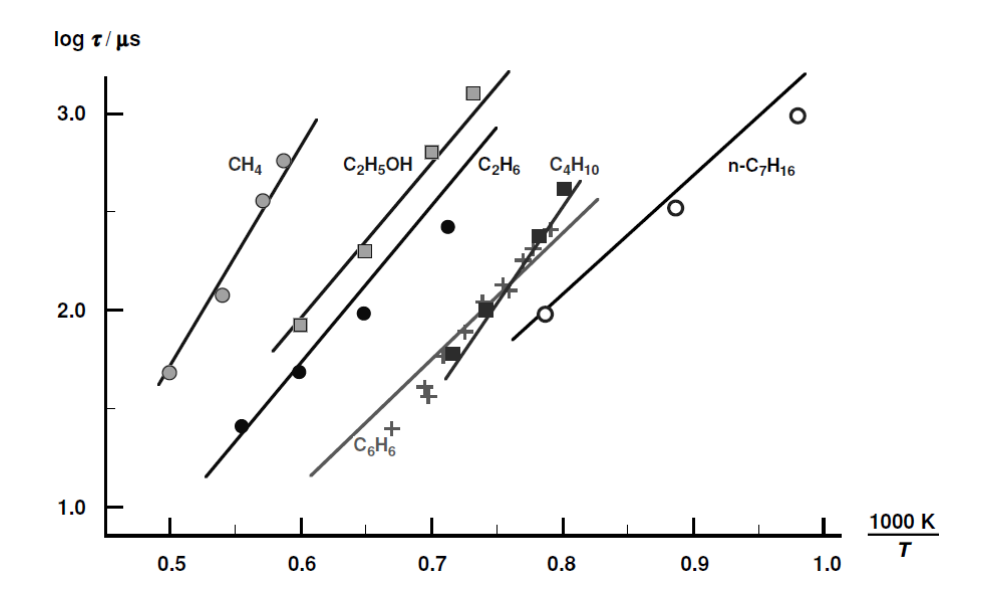


Figure 2-1- Calculated (line) and measured (points) ignition delay times in hydrocarbon-air mixtures [34]. The minimum ignition energy is the minimum required for ignition. If a small volume of a combustible mixture is heated to a sufficiently high temperature the mixture can ignite. Pressure and the change of specific heat per unit volume influence the ignition energy. However, minimum ignition energy is almost independent of the ignition duration and the minimum ignition energy densities are nearly independent of the composition within the ignition limits [33].

An example of an ignition source is the spark plug in a spark ignition engine. The deposition of energy caused by the electrode gap discharge into the source volume results in the formation of a plasma [34]. Usually the spark ignition process is divided into three phases: break down, arc and glow discharge [34]. Many parameters such as spark energy, gas composition, heat losses, and the flow field influence the energy discharge in the small gap between the electrodes. In addition, in the first phase, expansion of the plasma channel emits a shock wave which dominates the properties of the combustible mixture. The plasma channel induces a characteristic flow field and a growing hot channel that promotes ignition. A large part of the discharged energy is lost by heat conduction, the expanding blast wave and radiation while a small part remains for starting ignition.

However, after the breakdown, the chemical reactions overcome the heat losses by producing sufficient energy and the kernel grows beyond the critical size, which prevents quenching [33].

Xue et al. [35] provided details on the shape of the initial kernel as a function of the distance between the electrodes in a quiescent mixture. For a given mixture equivalence ratio, insufficient ignition energy results in extinction. However, in a typical application of the spark ignition process, the ignition kernel is embedded in a turbulent flow field. Consequently, the initial flame kernel is subjected to strain and can subsequently extinguish. Xue et al. [35] stated that two ignition processes with the same parameters can differ considerably because of the stochastic nature of turbulence.

Chemical reactions in a premixed gas usually cause flame propagation and preserve a gradient of temperature and species concentrations and molecular transport. This is called deflagration. In contrast to the deflagration process is the detonation process which is caused by pressure waves and sustained by the chemical reaction and the corresponding heat release. Detonation processes are unfavorable and are consciously avoided in internal combustion engines [33].

2-2 Turbulent Combustion

Turbulent combustion is divided into premixed and non-premixed cases. The process in which fuel and oxidizer are mixed by turbulence, before combustion is initiated, in a spark ignition engine, places this case in the category of premixed turbulent combustion. Energy deposited from the spark generates a flame kernel that initially grows by laminar and eventually by turbulent flame propagation [36-38].

On the other hand, combustion in a diesel engine takes place in a non-premixed condition. In a non-premixed system, the reactants are initially separated and interact through the molecular

process of diffusion and bulk convective motion [39]. Non-premixed combustion is usually termed as "diffusional combustion". However, since diffusion suggests the importance of the transport mechanism and is needed during the transport of thermal energy and combustion products into the reaction zone, premixed combustion includes diffusional processes as well.

The ratio of turbulent to chemical time scales is another criterion used to classify turbulent combustion. The turbulent Damkohler number is the ratio of the characteristic flow time, τ_{flow} , to the characteristic chemical time, τ_c , $Da = \frac{\tau_{flow}}{\tau_c}$, where the characteristic flow time is defined as the ratio of the integral length scale of turbulence and the instantaneous velocity ($\tau_{flow} = \frac{\Lambda}{u}$) and the characteristic chemical time is the ratio of the laminar flame thickness and the laminar flame speed ($\tau_c = \frac{\delta_L}{s_L}$) [36]. In order to define regimes of premixed turbulent combustion in terms of velocity and length scale ratios, diagrams have been proposed by Borghi [40, 41], Peters [42] and Poinsot [43]. The turbulent time scale is short when turbulence is intense and the chemical time scale also becomes short when the temperature is high. The case with short turbulent and long chemical time scales is called slow chemistry while the case of comparatively long turbulence and short chemical time scales is called fast chemistry. Spark ignition combustion is in the category of premixed fast chemistry [36].

Another general but more confusing terminology is homogeneous versus heterogeneous combustion. Combustion is homogeneous when reactants are initially in the same fluid gas phase. When reactants exist in different phases, at the location of reaction, combustion is called heterogeneous. In the TJI system, although the chamber mixture is initially premixed and homogeneous, injection of the liquid fuel spray produces fuel vapor pockets through the vaporization process and increase the likelihood of local heterogeneous combustion.

2-3 Lean Burn Combustion

Internal combustion engine improvements aim at improving efficiency while minimizing the emission of pollutants. Thermodynamic analysis of a spark ignited engine is based on the Otto cycle, for which an increase of the compression ratio increases the engine efficiency ($\varepsilon \approx 1 - \frac{1}{C_R^{(k-1)}}$; $k = \frac{c_p}{c_v}$) [44]. However, the upper limit of this increase depends on the onset of knock which is the sudden ignition of the high temperature end gases in the engine cylinder. High pressure peaks introduced by engine knock cause damage to the piston and the engine [29, 33].

Another method to improve the maximum thermal efficiency of the Otto cycle is through the lean burn combustion in gasoline spark ignited engines. Lean burn typically occurs at partial engine loads and is a powerful means to reduce engine pumping losses. The effective parameter in engine efficiency is the increase of specific heats of the working fluid. Since burning lean contributes to an increase of the ratio of the specific heats in the mixture, it indirectly increases the efficiency [44]. In addition, a significant amount of the engine power is used for pumping during the throttling processes. The throttle valve located in the engine's intake is responsible for controlling the amount of air that enters the engine. Burning lean allows a similar amount of air to enter the engine at both the lower and higher load points. As a result, pumping work reduces while the load is still limited by the amount of fuel.

Lean combustion is also advantageous for nitric oxide (NOx) emission reduction. NO and NO₂ collectively called NOx are the major contributors to photochemical smog and ozone pollution, which participates in the chain reaction for removing ozone from the stratosphere resulting in increased ultra violet radiation to the earth's surface [45]. Consequently, it is important to

understand the underlying chemical kinetic mechanisms that generate NOx and the interaction of these kinetics with the fluid dynamics in order to minimize NOx emission.

Bowman [46] identified four different routes in the formation of NOx as the thermal route, the prompt route, the N₂O route and the fuel bound nitrogen route. These are briefly explained below.

Elementary reactions form the thermal NO, or Zeldovich NO mechanism (postulated by Zeldovich [47]). The high activation energy of the reaction between the O radical and the N_2 atom, is due to the strong triple bond in N_2 , which causes these reactions to be sufficiently fast only at high temperatures, leading to the name "thermal NO".

Another route for NO formation is the prompt or Fenimore NO mechanism, [48]. Measuring NO above a hydrocarbon flat flame, Fenimore noted that in contrast to the Zeldovich mechanism prediction, NO did not approach zero as the probe approached the flame from the downstream side. Prompt NO results from the radical CH which was previously considered to be an unimportant transient species. Nitrogen from the air reacts with the CH as an intermediate only at the flame front, and forms HCN, which further reacts with NO; $CH+N_2 \rightarrow HCN+N \rightarrow NO$, N_2 . In contrast to the thermal NO, the activation energy of the above reaction is low and therefore prompt NO occurs at comparatively low temperature (~ 1000K)

Similar to the thermal mechanism, O atoms attack molecular nitrogen in the nitrous oxide (N_2O) mechanism but the presence of a third molecule, M, results in the formation of N_2O [33], $N_2+O+M\rightarrow N_2O+M$. Subsequently, N_2O reacts with O to form NO [49], via $N_2O+O\rightarrow NO+NO$. This mechanism is a major source of NO in lean premixed gas turbine engines [33].

The fourth route of NO formation is fuel-bound nitrogen (FBN). Some fuels (like coal) contain chemically bound nitrogen. During the gasification process of coal, nitrogen-containing compounds evaporate and form gas phase NO.

Among different mechanisms of NOx formation, the Zeldovich [33] or thermal mechanism in which N₂ atoms dissociate and collide with O radicals, also requires higher temperature. This is the most common mechanism in SI engine operation. Since the flame temperature decreases in lean combustion, lower amounts of NOx form through the Zeldovich mechanism and NOx emissions are reduced.

Two possible methods of NOx reduction are combustion modification and post combustion processing. Combustion devices require modifications in order to minimize the NO emission. Lean burn combustion devices such as TJI systems, which will be explained later, are an example of device modification. The presence of excess air in lean burn technologies results in a further reduction of NO formation through the thermal NO mechanism, by suppressing the peak temperature. Injection of an inert diluent or water is also beneficial as this can reduce the temperature through added heat capacity. Exhaust gases are reasonably inert, and the process of using exhaust gas as an inert diluent is called exhaust gas recirculation (EGR) [33].

Currently the main post process NO reduction method in SI is the catalytic converter, which employs a combination of metals acting as catalysts for the reactions converting HC to CO_2 and H_2O , CO to CO_2 and NO to N_2 .

The implementation of lean combustion is not easy due to several drawbacks. First, it is hard to ignite a lean mixture due to their lowest flame speed compared to stoichiometric mixtures. This increases cycle to cycle variation. In addition, lean burn technology is not compatible with the

three-way catalytic (TWC) converter, which is commonly used in all gasoline vehicle exhaust systems. Shelef and McCabe [50] provided a TWC efficiency plot based on the air/fuel ratio (AFR), see Figure 2-2. As can be seen in the figure, deviation from stoichiometric conditions greatly influences the performance of the TWC.

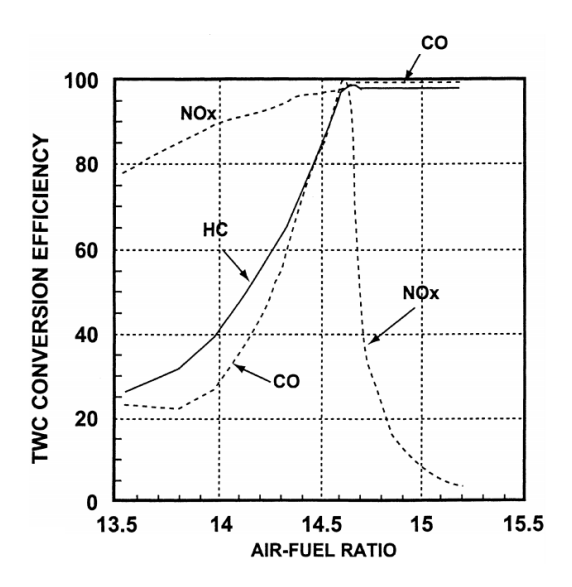


Figure 2-2- Typical Three-Way-Catalyst plot vs. air-fuel ratio [50].

In order to operate the NOx emission reduction process when excess oxygen is available, after treatment technologies can be used [51, 52]. These technologies have improved greatly.

2-4 Turbulent Jet Ignition System

Ignition enhancement methods aim to increase the ignition energy to improve burning characteristics of the fuel. When a system runs lean, a long duration, wide dispersion, high energy ignition source is required. Due to the low flame velocity of lean mixtures, it is important to initiate combustion at multiple sites to increase burn rate [1]. Combustion enhancement systems for spark ignited engines have been studied for decades. Dale and Oppenheim [9] and Dale et al. [11]., performed a complete review of combustion enhancement systems for homogeneous fueled internal combustion engines. Among all, technologies such as microwave spark ignition [12],

plasma-assisted ignition, [13, 14], divided chamber stratified charge [15], prechamber ignition systems were highlighted. Prechamber ignition systems are of great interest because they are capable of producing low temperature lean and/or dilute combustion.

A comprehensive review of the literature of prechamber ignition systems is presented by Toulson et al. [1]. This review covers systems ranging from the two-stroke Ricardo Dolphin engine [53], the three-valve engines of Summers [54] and Mallory [55], the LAG engine of Gussuk [56, 57] to the flame jet ignition system of Oppenheim et al. [58]. In fact, the jet ignition concept was first introduced in 1950's by the Russian Noble prize winner Nikolai Semenov, and was given the name of LAG (Lavinnia Aktyvatsia Gorenia) which translates to "Avalanche Activated Combustion" [1, 56, 57]. LAG is a divided chamber stratified charge ignition system in which the ultra-lean mixture ignited by a chemically reacting jet of fuel rich combustion products. With the LAG system, a small prechamber is used for the initial combustion and the pressure rise in the prechamber forces the combustion products to enter the main chamber through a small orifice(s) in a form of hot turbulent jet(s) which burn the lean mixture of main chamber that is entrained by the jet(s) [56, 57]. Following LAG, Oppenheim et al. [59-61] developed an ignition device that worked with the same concept termed Jet Plume Injection and Combustion (JPIC). JPIC was introduced as a radial refinement of Direct Injection stratified Charge (DISC). This system consisted of a fuel injector connected to a Pulsed Jet Combustion (PJC) generator. JPIC produced stratification in the composition of the charge as well as in the scale and intensity of turbulence. In order to show the salient features of the fluid mechanical phenomena of the JPC process, Maxson et al. [59] recorded a series of Schlieren images shown in Figure 2-3 and Figure 2-4.

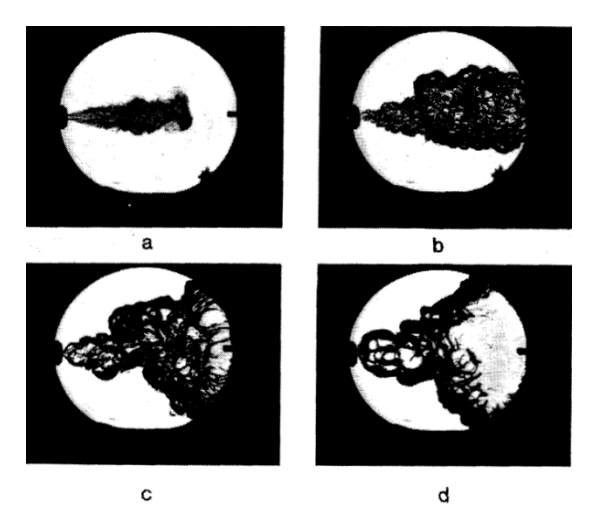


Figure 2-3- Schlieren records of Single Orifice PJC systems, orifice diameter=2.5 mm [59].

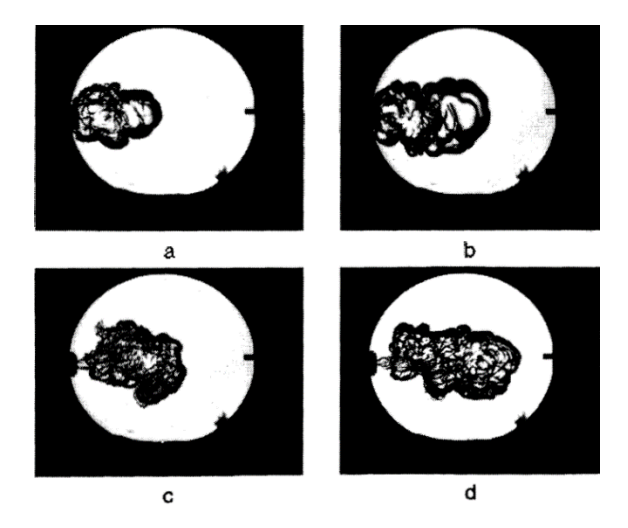


Figure 2-4- Schlieren records of a single orifice PJC systems, orifice diameters: a&b: 6 mm; c&d: 4 mm [59].

The authors showed that PJC was capable of shortening the pressure rise time while increasing the amplitude of the pressure pulses.

Later, Watson et al. [62-64] developed the concept of Hydrogen Assisted Jet Ignition (HAJI) at the University of Melbourne. The HAJI design also consisted of a small prechamber and orifices, spark plug and direct injector with hydrogen as the prechamber fuel. Hydrogen improved the lean limit up to λ =2.5, with Liquefied Petroleum Gas (LPG) as the main chamber fuel. Toulson et al. [63] studied LPG as an alternative prechamber fuel to enable a single fuel system, which showed

significant lean limit improvement up to λ =2.35 for both LPG and Gasoline as the main chamber fuels. Additional studies on prechamber ignition systems were carried out by Watson et al. [37, 38].

The newest refinement of the jet ignition concept is the turbulent jet ignition system. Combustion in the unfueled TJI system, similar to conventional spark ignition engines, occurs in the premixed mode which is one of the two categories of turbulent reacting flows [42]. The prechamber is a small volume chamber where an injector(s) and spark plug, or an alternative ignition system, are housed. This prechamber is connected to the main combustion chamber through either one or multiple narrow orifices. The combustion that initiates in this prechamber, increases the mixture pressure which drives the flow of gases from the prechamber into the main chamber. The entrained turbulent jet increases the turbulence and mixing rate in the main chamber. As a result, the main chamber dilute fuel-air mixture has a higher chance of igniting through the action of spatially distributed ignition sites. The unsteady turbulent jet plays a dominant role in combustion duration, flame propagation and burn rate.

Early studies on various features of the TJI system (such as comparison of the knock limit of conventional spark ignition and prechamber jet ignition combustion, and flame kernel development for spark initiated prechamber combustion) were performed by Attard et al. [20, 26, 27, 29-32] at MAHLE. The turbulent jet ignition system that was used by MAHLE was installed in a four valve, pent roof engine. Schematic pictures of the turbulent jet igniter are shown in Figure 2-5 and Figure 2-6.

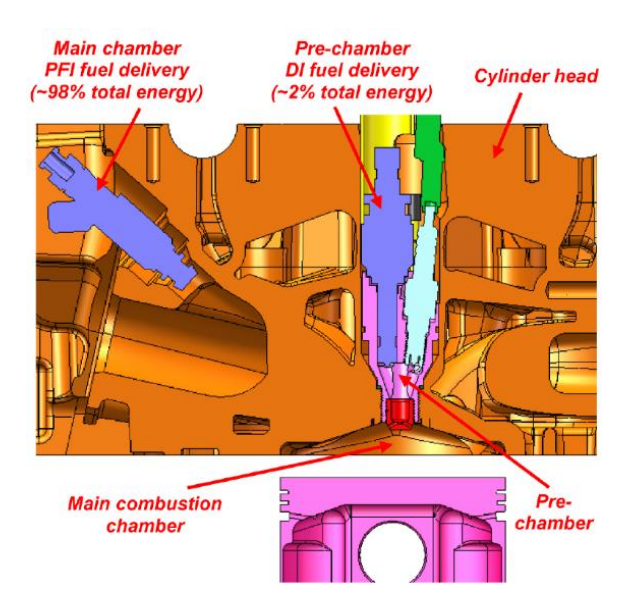


Figure 2-5- Section view image of a Turbulent Jet Igniter centrally installed in the test engine's four valve, pent roof combustion system [31].

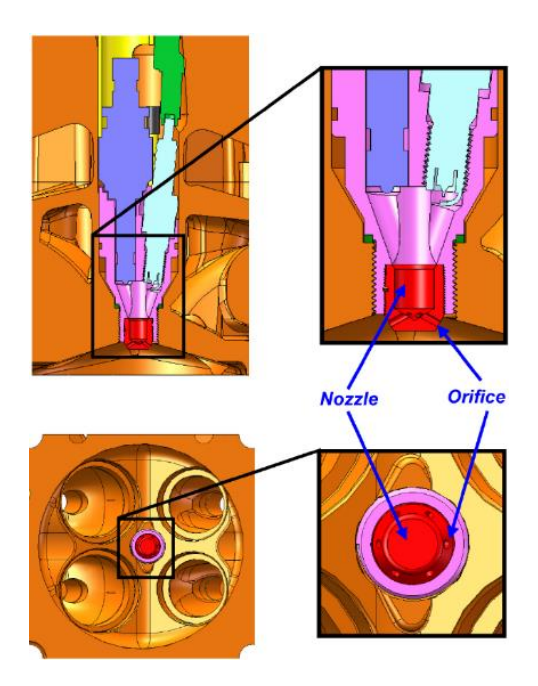


Figure 2-6- Detailed images of the Turbulent Jet Ignition prechamber and nozzle in the 4-valve pent roof combustion system [31].

A parameter that strongly affect the turbulent jet structure is the nozzle orifice area. A recent study on the influence of the nozzle orifice was performed by Gentz et al. [19], using combustion visualization and characterization of TJI in a Rapid Compression Machine (RCM). The RCM, a

device often used to study the fuel ignition behavior at high temperature and pressure, produces conditions similar to those experienced in engine combustion [65]. All of the experiments by Gentz et al. were performed in the RCM facility at Michigan State University (MSU). More details of the MSU RCM facility are provided in the Experimental Set-up Section.

Gentz et al. [19] showed that for near-stoichiometric conditions, a wider nozzle produced more spatially distributed jets, resulting in faster combustion. However, at leaner conditions, a smaller diameter orifice that yielded a faster and more vigorous jet was required to initiate combustion. These opposing trends suggest that there may exist an optimum nozzle diameter.

Similar to Gentz et al. [19], Shah et al. [66] investigated the effect of prechamber volume as well as orifice area on the flame development angle, combustion duration, heat release, lean limit extension and NOx emission. Shah et al.'s [66] experiments were performed in a 2L engine modified to include a prechamber equipped with a spark plug, fuel injector and pressure transducer. They tested three prechamber volumes and three orifice areas. Based on their results, increasing the prechamber volume reduced the flame dispersion angle and the combustion duration while increasing the heat release in the main chamber. However, further increases in the prechamber volume produced detrimental effects on combustion such as the decrease in combustion duration and increase in the rate of heat release. These countervailing trends suggested the existence of an optimum prechamber size. In order to measure the heat release of the prechamber, the pressure difference between the pre and main chambers was analyzed. It was found that a smaller prechamber resulted in a shorter jet, due to the lower pressure in the prechamber. The smaller prechamber also increased the combustion efficiency. The authors determined that the prechamber size is optimized when complete prechamber ejection occurs. However, in terms of NOx emissions

a larger prechamber volume coupled with a smaller orifice area was more effective in emission control [66].

The prechamber size and orifice diameter were examined in several studies [16-18]. It was determined that if the orifice diameter was too small, (d<1mm), the jet was not capable of igniting lean mixtures in the main chamber. In addition, smaller orifices, although having greater jet penetration, gave higher heat losses [1]. The commonly used orifice diameters for prechamber ignition systems in general, and TJI systems in particular, are in the range of 1-4 mm [1, 19]. Murase and Hanada [67] showed that the faster pressure rise is attainable with the smaller orifice diameter (\sim 2.5 mm compared to 4 mm) and it greatly enhances combustion. In order for sufficient pressure rise in the prechamber, a large orifice diameter (d>3 mm) should be avoided [67]. Another parameter affecting combustion in a TJI system is the variation in the pressure rise in prechamber that occurs because of the distance between the spark plug and the orifice exit.

Sadanandan et al. [68] performed an experimental and numerical investigation of hydrogen-air mixture ignition by jets of hot gases. High speed laser induced fluorescence (LIF) imaging of the hydroxyl radical (OH) and laser Schlieren methods were used to study the spatial and temporal evolution of ignition. The hydroxyl radical (OH) is an important intermediate species that is formed during combustion and is an indicator of the reaction zone. Their results show that the change in the ignition distance (from the spark plug to the nozzle inlet) changes the in pressure ratio over the nozzle. Two of the adjustable parameters of the experiments were the pressure difference between chambers and the nozzle diameter. Their results showed that it was necessary for the nozzle diameter leading to 100 % ignition to increase with increasing pressure difference, in order to decrease the outflow velocity and to increase the temperature of the hot jet. In addition, an increase of the ignition distance from the nozzle exit inside the jet was mainly caused by the

higher pressure difference leading to a higher outflow velocity and mixing rate. With increasing distance from the nozzle outlet, velocity and mixing decreased and chemical reactions led to an ignition location which nearer to the jet axis than the sides. In conclusion, the OH-LIF emission did not happen at the jet boundaries but well within the jet near the tip [68].

The next parameter influencing combustion in the TJI system is dilution. Silke et al. [69] investigated the effect of diluent gases on ignition delay in a RCM and a shock tube. The gases under study were helium, argon, xenon and nitrogen. The effect of dilution in the RCM and shock tube were not similar and sometimes opposite. For instance, argon accelerated ignition in the RCM but decelerated ignition in the shock tube under some conditions. The authors explained this opposite effects by the difference in time scales involved in these two devices. Results of experiments and modeling showed extreme heat loss in the post compression period, particularly for helium. Besides, ignition delay depends on the type of diluent used. Helium showed a stronger diluent effect due to higher thermal heat capacity and/or thermal conductivity. In fact, helium is able to carry heat to the chamber walls at a much higher rate, cooling faster, and thus lengthening the ignition delay.

In the shock tube, the reaction is adiabatic but the higher heat capacity of a diatomic gas has an adverse effect on ignition delay. Silke et al.'s simulation results showed that the type of fuel and diluent as well as their concentrations have a dominant effect on the ignition delay. However, the diluent effect was shown to disappear at higher temperatures. The chemistry dominates the reactive systems in the two temperature regimes and neutralize the dilution effect. Ignition enhancement of highly diluted mixtures, through the use of auxiliary fuel and air injection into the prechamber is investigated in this thesis and will be discusses more in Chapter 5.

The turbulent jet of the TJI system has a structure similar to the Pulsed Jet Combustion (PJC) system [60]. Maxson et al. [59] defined three stages for the PJC process as the "jet", the "plume" and the "puff". A graphical picture of the turbulent jet plume is show in Figure 2-7.

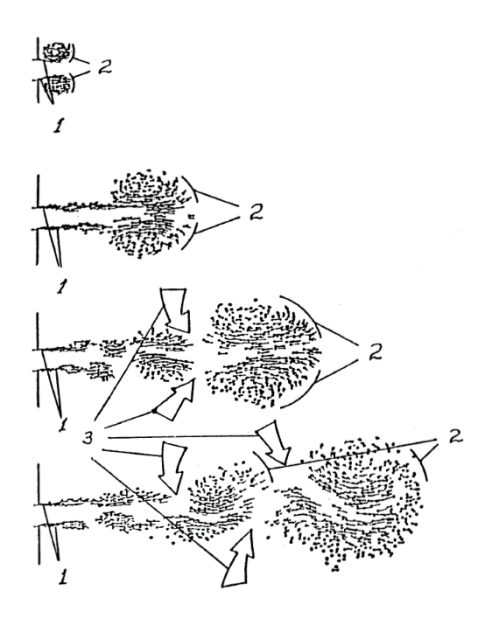
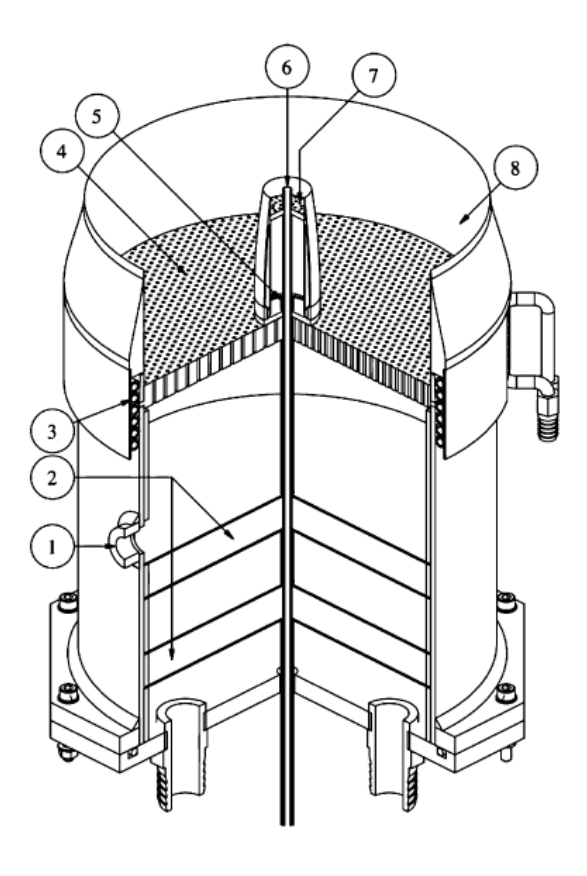


Figure 2-7- Turbulent jet plume structures, 1- stretch and extinction of intense shear zone, 2- large scale vortices, 3- entrainment process [59].

The "jet" is defined as the initial core of the jet that consists of the incomplete combustion products at high temperature in which the mixing is disabled by shear at the orifice exit. This produces a time delay for the onset of combustion. The most active stage of PJC is the "plume", where the large scale structures of the turbulent field in the combustion chamber enhance combustion. Finally, the turbulent cloud of products surrounded by the flame front is termed the "puff." Maxson et al. stated that a 2.0 *mm* single orifice diameter, produced unreliable operation of the system. The triple orifice system showed better performance. They also investigated the performance of two simultaneously opposed jets and observed a higher rate of pressure rise with the opposed jet system than the single jet [59].

The TJI system configuration also has similarities with the Piloted Premixed Jet Burner (PPJB) [70]. The initial characteristics of a PPJB and the finite rate chemistry effects in highly turbulent lean premixed combustion were investigated by Dunn et. al [70]. The configuration of PPJB is shown in Figure 2-8. PPJB consists of a central jet of high velocity lean premixed methane/air mixture piloted by a low-velocity stoichiometric premixed pilot of hot reaction products from a stoichiometric fuel/air mixture (methane was used as the fuel in [70]). A large diameter coflow of lean premixed hydrogen-air combustion products surrounds the pilot and the central jet, isolating them from the surrounding air stream. The coflow-stream isolates the flame from the surrounding air-stream to eliminate potential quenching and dilution. Under certain conditions, the central jet combustion experiences an extinction-reignition process. The interpretation of this process was that the intense turbulent mixing after the nozzle drives an initial extinction process which reduces luminosity, with reignition occurring downstream in the region of lower turbulent mixing. Reignition causes the flame luminosity to increase.



Balloon number	Description
1	Flashback over-pressure sensing port
2	Glass bead filled cavities
3	Cooling water coil
4	Coflow perforated baseplate
5	Pilot mixture feed exit
6	Central jet exit
7	Pilot perforated baseplate
8	Coflow collar

Figure 2-8- Sectioned view of the PPJB, with significant features labeled [70].

Chen and Ihme [71] applied a three stream flamelet/progress variable model to the Sydney piloted premixed jet burner (PPJB). In order to extend the applicability of their formulation to partially premixed combustion, a prior model was evaluated with experimental data. They introduced a Dirichlet distribution to describe the interaction between the two mixture fractions that are associated with the fuel, pilot and coflow streams. The three stream combustion model was applied to a LES model of all four burner configurations examined by Dunn et al. [70].

Rowinski and Pope [72] used the joint velocity-turbulent frequency-composition PDF method to study piloted premixed jet flames. The mean and *rms* mixture fraction field calculations showed good agreement with experiments, however, the reaction progress was over-predicted depending on the jet velocities. The numerical method included a particle solver coupled with a finite volume solver for the equations of mass, momentum, energy and state. The finite volume solver interacts with a particle solver by receiving turbulent quantities and reaction source terms while providing the mean flow velocity and pressure. This study showed that the increase in central jet velocity results in reduced burner flow time scales and hence a Damköhler number reduction.

The major difference between TJI and PPJB is that with PPJB the high velocity central jet enters into a laterally confined open-ended environment whereas the central TJI jet enters into a bounded combustion chamber in which the jet does not become fully developed. Secondly, the PPJB central jet is a cold mixture of methane/air in [70] and the surrounding pilot and coflow mixtures are hot products of methane/air and hydrogen/air, respectively. By contrast, the TJI central jet mixture consists of hot products of fuel/air combustion that enter into a colder quiescent fuel/air mixture. While the nozzle exit velocity and density of the PPJB are fixed, the nozzle exit velocity of the jet in TJI is highly transient.

2-5 Round Turbulent Jet

Round turbulent jet flows have been extensively studied experimentally and numerically. A schematic description of a jet penetrating into a fluid at rest is shown in Figure 2-9 [73].

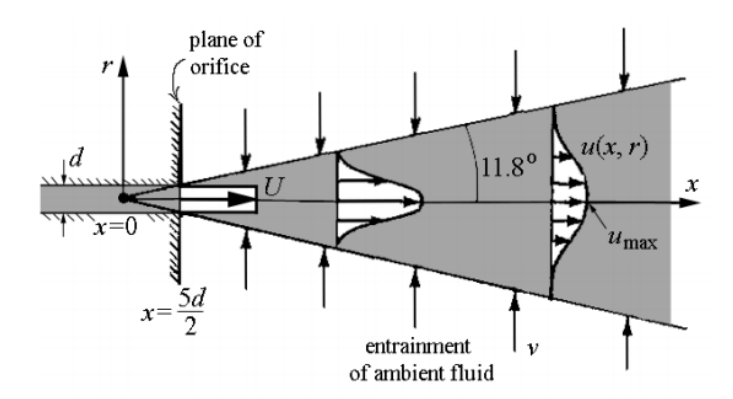


Figure 2-9- Schematic description of a jet penetrating a fluid at rest. The virtual origin is located at x=0, 5d/2 upstream from the nozzle exit plane [73].

In Figure 2-9 a polar coordinate system is used to describe the round jet, the x-direction being aligned with the flow direction. For a constant orifice diameter, d, the jet exit velocity is defined as v_e . Cushamn-Roisin [73] stated that because the initial jet diameter is not zero but consists of a finite size orifice or opening, the stream-wise distance, x, should be measured from a virtual source inside the nozzle at a distance 5d/2 upstream from the nozzle exit (see Figure 2-9). Naber and Siebers [74] gave a slightly different definition for the virtual origin, which depends on the orifice exit diameter, density ratio and jet cone angle of the outer boundary of the jet (a measure of spray dispersion). As the fluid exits the orifice, it experiences different flow regions starting with a developing regime an initial slug flow velocity profile (see Figure 2-9, at the orifice) and ranging to a fully developed region with a self-similar velocity profile [75] that is independent of the initial profile.

Based on the characteristics of the velocity field, Fellouah et al. [76] identified three separate and distinct flow regions. The near-field, where x/d is between zero and six, is the initial flow or development regime with a top-hat velocity profile. The flow characteristics here match those at the nozzle exit. In the far-field region, where x/d is greater than 25, the flow is fully developed.

This region is the self-similar region where the thin shear layer approximations hold (with appropriate scaling). The intermediate field occurs between the near-field and the far-field. In this transition region the developing jet has characteristics of both the near and the far fields [77]. The near- and intermediate- fields together comprise the developing portion of the jet, referred to as the near and intermediate field (NIF)

As described by Ball et al. [75], an unstable laminar shear layer is produced near the orifice exit of a non-reacting axisymmetric jet. This shear layer grows rapidly to form ring vortices, and generates a flow exchange from the irrotational ambient air into the jet and vice-versa. The turbulent jet in the TJI system is not simple and cannot be described easily because it consists of burning gases that enter a stagnant, homogeneous, and not-yet-reacting surrounding fluid. Here, the hot gas jet not only flows into the surrounding mixture but also serves as its ignition source. In addition, the TJI jet is transient.

To shed light on the influence of Reynolds number on the near and intermediate field regions of a round jet, Fellouah et al. [78] used flying and stationary hot wire measurements. Their experiments used the Reynolds number range $6,000 \le Re_D \le 100,000$ in order to explore the idea of mixing transition proposed by Dimotakis [79]. The mixing transition was highly spatial and Re dependent. Fellouah et al. [78] did not examine reacting jets.

Hrycak et al. [80] experimentally examined the nominal and the actual length of the potential core of an axisymmetric jet and showed that in the potential core region, the nominal core length is independent of Reynolds number except in the transition region.

Another dominant parameter of the turbulent jet is the entrainment rate and spray dispersion. The local entrainment rate in the initial region of the axisymmetric air jet was studied by Hill [81] who

used the porous wall technique introduced by Ricou and Spalding [82]. Here, the jet flows through a chamber that is open at one end to atmospheric pressure. Hill showed that the local entrainment rate, although independent of the Reynolds number for $Re_D>60,000$, which is about half of the value specified by Fellouah et al. [78], depends on the axial distance from the jet exit. Hill's results show that the jet flow reaches the fully developed condition at an axial distance of about thirteen nozzle diameters from the exit, between the top hat (6) and the self-similar (25) regions described by Fellouah et al. [78].

Penetration and dispersion of diesels sprays have similarities with reacting transient compressible gas jets (i.e., the turbulent jet of the current study). Studies on various aspects of gas and liquid sprays are abundant. An example is the study of a helium spray in an air chamber (Johansen et al. [83]). Schlieren visualization was used to investigate the mean coefficient of variation of the penetration length, jet width, and jet angle for the transient compressible gas jet in direct injection gas fuel engines. The dispersion of the penetration length agreed with a normal distribution and the Turner jet model agreed with the observed jets. The jet underwent transition to self-similarity within 20 nozzle diameters. The jet angle approached a constant value and agreed well with a normal distribution.

Johansen et al. [83] found that if the jet is under expanded, a structure of expansion and shock waves will likely occur at the nozzle exit. These expansion and shock waves are required for the jet to reach the ambient pressure. Expansion waves may occur in the present TJI system as well.

Naber and Siebers [74] performed experiments in a constant volume combustion vessel using Schlieren imaging to investigate the influence of ambient gas density and fuel vaporization on the penetration and dispersion of diesel sprays. The range of gas density was higher than the TDC

conditions of current heavy-duty diesel engines. The orifice diameter varied between 0.19 and 0.3 mm. Time resolved extinction/Schlieren imaging was used for the analysis of the transient spray penetration data. Two sets of non-vaporizing and vaporizing spray experiments were performed in [74], where the vessel was filled with either nitrogen or a helium/nitrogen (60%/40%) mixture. The primary variable was gas density (3-200 kg/m³ for non-vaporizing tests and 3-60 kg/m³ for vaporizing tests). Other parameters were tip orifice diameter and injection pressure. The ambient temperature was either 300 K or 450 K for non-vaporizing tests. The range was 600-1400 K for vaporizing tests.

The authors derived a data correlation based on integral control surface techniques to explain the effects of ambient gas density on the jet. Their results showed two distinct periods, an initially very slow penetration period followed by a sudden transition to a fast penetration. The local air entrainment rate along a spray is proportional to the ambient air density (ρ_a) , the orifice diameter (d_0) , the injected fuel velocity (U_f) and the tangent of the spray dispersion angle $(\theta/2)$;

entrainment
$$\propto \rho_a.d_0.U_f.\tan(\frac{\theta}{2}),$$
 2-1

where increases in ambient gas density increase the spray dispersion angle, and the spray will behave like an incompressible jet. Their results also showed that spray penetration decrease as the ambient density increases.

Their results also showed that as the ambient density increases, the dispersion angle increases because the fuel momentum is transferred to a larger quantity of air. This results in lower overall spray velocity and a slower penetration. The penetration reduction by vaporization increases with an increase in orifice diameter and fuel density. It decreases with ambient gas density and

dispersion angle. Vaporization reduced penetration and dispersion by up to 20% relative to non-vaporizing sprays.

Another parameter that was introduced was the transition time, similar to the "break up time", that had been introduced by Hiroyasu and Arai [84]. This is the time when the transition is made from a linear dependence of penetration on time to a square root dependence. More details of the Naber and Siebers model are provided in the current study. The break up time is explained in section 6-1-3.

A follow up of [74] was the study of the transient gas jets by the use of a simple one dimensional jet model performed by Musculus and Kattke [85]. They proposed a simplified model based on a control volume analysis for steady injection assuming a constant jet spreading angle, constant injection velocity and no velocity slip between the injected fuel and the ambient gas. The main model assumptions were that the jet was a non-vaporizing liquid, the flow was assumed to be incompressible, and the viscous forces were small compared to the pressure forces. In addition, axial mixing of momentum due to the molecular and turbulent diffusion was neglected. Although this model captured the important physics of diesel jets, it was not capable of predicting jets with unsteady injection rates.

Musculus and Kattke's results showed that as the injection velocity decreases at the end of injection (EOI), the entrainment (i.e., increase in radial velocity) rate increases to compensate for the decrease in upstream axial mass flux into the large structures of the jet. The model showed that the increased entrainment, termed as the "entrainment wave," travels downstream two times faster than the initial jet propagation. This produces increased mixing. The entrainment waves are also responsible for the rapid stagnation of the mixture near the injector, spatial shifting in the location of the onset of soot formation and a soot formation increase after EOI. Also, they decrease the

penetration of short injections and split the liquid part of the vaporizing spray. Soot formation also strongly depends on the time between the end of injection and ignition, called the "ignition dwell." The increase of ignition dwell moves the location of initial soot formation downstream following the entrainment waves.

Although the rapid increase of mixing after EOI is beneficial for soot reduction, it would be detrimental to UHC and CO emissions if mixtures are too lean for complete combustion [85]. The authors also investigated the fast ramp-down of injection rate at EOI. This created a stronger entrainment wave and, consequently, a leaner mixture near the injector.

A physical model that predicts the velocity distribution in round jets with time varying injection profiles was developed by Abani and Reitz [86]. The approach introduced an effective injection velocity within the jet based on a representative response time. It was assumed that the instantaneous injection velocity affected the velocity within the jet with an exponential response function and that the response time was related to the fluid particle's residence time within the jet, consistent with the theory of the translation of jet vortex rings from Helmholtz's analysis [87]. In this work the authors tested various injection profiles and ambient densities. They obtained a steady state solution for the velocity profile within a turbulent gas jet using similarity analysis of the 2D axisymmetric Navier-Stokes equations. This model was used to study transient jet and spray injection processes and to predict the jet tip penetration speed of the current study, see section 6-1-2.

2-6 Numerical Modeling Background

Combustion processes in SI engines and/or TJI systems have been broadly investigated experimentally. However, numerical modeling of these processes is more challenging than many

classic or modern fluid mechanics problems due to the reacting nature of the flow and the presence of combustion in complicated geometries. Hence, the number of computational and analytical studies on the reacting jet of the TJI system is limited. An exception is the review by Haworth [88] on turbulent combustion modeling for reciprocating-piston IC engines. Here turbulent combustion models were explained and multidimensional case studies were provided as illustrative examples. Haworth categorized the engine combustion system by the way the reactants were ignited and by the degree of homogeneity of the fuel-air mixture (homogeneous charge versus stratified charge). Four basic IC engine combustion systems (homogeneous-charge spark-ignition, stratified-charge spark-ignition, homogeneous-charge compression-ignition and stratified charge-compression-ignition) were discussed in detail including the numerous required closure models.

Numerical simulations can be performed by using either of these three major simulation approaches; Direct Numerical Simulation (DNS), Large Eddy Simulation (LES) and Reynolds Averaged Numerical Simulation (RANS) that will be explained later. In industry, most of the CFD simulations are carried out using the RANS approach, which is computationally less expensive but gives lower accuracy than the LES approach. Also, RANS depends strongly on the turbulence model, the numerical parameters, and the numerical integration schemes being used.

Models of ignition and flame propagation in various combustion devices, use different methods and approaches. D'Errioc et al. [89] used two approaches to model flame propagation in a heavy duty diesel engine. Both were implemented into the Lib-ICE code, based on the OpenFOAM technology [90], with detailed chemistry and a turbulence-chemistry interaction model. In one model the diesel spray flame was assumed to be an ensemble of diffusion flames created during injection. These flames evolved in mixture fraction space according to the conditionally averaged value of the scalar dissipation rate. The second model employed tabulated kinetics from perfectly

stirred reactor calculations. Here the flame structure was described using multiple homogeneous reactors with the turbulent-chemistry interaction regulated by a presumed β -PDF. At constant-volume conditions both models predicted auto-ignition and flame stabilization. In engine simulations both models reproduced experimental in-cylinder pressure profiles.

Numerous studies have been devoted to the problem of flame kernel formation, mixing and ignition phenomena as well as flame propagation in laminar and turbulent flows. A coherent model that accounts for all relevant physical and chemical conditions, independent of parameter variations, especially in spark ignition engines does not exist. As described by Boudier et al. [91], during the spark, energy is deposited in the turbulent gas resulting in the initiation of chemical reactions and a flame kernel due to a sufficiently high temperature. In laminar flows, asymptotic and numerical methods and experiments are normally used to study flame kernel growth. However, the effect of turbulence on ignition processes is still largely unknown. Boudier et al. [91] coupled a flame ignition model in a premixed turbulent flow to a flamelet model for turbulent combustion in order to describe flame ignition and propagation in a spark ignition piston engine. The authors compared their modeling results with experimental data (Schlieren visualization, Laser Doppler Anemometry (LDA) and pressure measurements) and obtained acceptable agreement.

For the simulation of combustion in direct injection-spark ignition (DI-SI) engines, Colin et al. [92] made improvements to the classical coherent flame model (CFM) and produced the extended coherent flame model (ECFM). They included the influences of small scale stratification into the ECFM model using a variance/scalar dissipation model with a probability density function approach for fuel stratification. For initiation of combustion at the spark plug, the spark ignition model AKTIM (arc and kernel tracking ignition model) was modified to account for turbulent flame wrinkling. In addition, a model to predict knock in SI engines was described. Their models

were validated by Laser-Influenced Fluorescence (LIF) measurements in an optical engine together with a gasoline direct injected Mitsubishi engine. The AKTIM spark ignition model describes the initiation of combustion by the spark plug. Although the model performs accurately in some simple homogeneous engine test cases, it lacks predictability when engine parameter variations on spark ignition are performed [92, 93]. In order to model the electrical circuit of a the spark ignition system and to compute the breakdown and glow energy, Falfari and Bianchi [94] set up a 1D/Lagrangian ignition model coupled to a CFD solver to compute the initial flame kernel radius and temperature based on the physical mixture properties and spark plug characteristics. This model was validated using experimental tests by Herweg and Maly [95].

To test a zero-dimensional approach, Mittal et al. [96] numerically modeled n-heptane RCM experiments under conditions of two-stage ignition and in the negative temperature coefficient (NTC) regime. The zero-dimensional approach (based on adiabatic volume expansion) performs well in predicting the first stage ignition delays. The discrepancy between model and experiments was pressure dependent and decreased with increased compression pressure. Although using the improved zero-dimensional approach (incorporating multiple zones, including the core region, boundary layer and crevice, and allowing for the exchange of mass and energy) might be viable compared to the full CFD RCM simulation, this model introduces additional uncertainties due to heat loss to the wall and the coupling of the pressure drop with the chemical reactions and heat release.

Xu et al. [97] implemented an ignition model in STAR-CD in conjunction with the G-equation combustion model to study combustion in a lean burn gasoline engine. The results agreed well with the cylinder pressure and the heat release rate for the most operating conditions.

A comparative study between the RANS and LES simulations of cold flow analysis for a single cylinder engine was performed by Gupta et al. [98]. The comparison was made of the cycle averaged velocity and turbulence predictions and particle image velocimetry (PIV) measurements (as the reference data). They compared the effect of full and partial geometry (with and without intake and exhaust plenums) as well as the RANS and LES simulations in terms of their capability to predict the mean flow and the turbulence flow field. The simulations were performed using CONVEGE commercial software [99].

Their results showed that the RANS partial geometries predict higher velocity magnitudes and a wobbly jet structure; on the other hand, full geometries predict lower velocity magnitudes with more stable jet structures. Comparing the turbulence predictions and mean flow, the RANS simulation with partial geometry showed a better performance. Between the two models, the RNG k- ε model partial geometry simulation gave better turbulence distributions compared with the standard k- ε model. In terms of the qualitative structures of the flow structures, the RNG k- ε model gave acceptable results but for accurate details, LES modeling was needed. In addition, both LES and RANS gave reasonably accurate predictions of turbulence magnitude. However, the turbulence distribution and local structures were captured better by LES [98].

Regardless of the numerical scheme, mesh resolution plays an important role in numerical simulations. Pomraning et al. [100], performed a comprehensive study demonstrating the importance of mesh resolution in a RANS combustion simulation. In this study a 3-D simulation of chemically reacting turbulent flows in a diesel engine and the simulation of premixed combustion in a gasoline engine were completed. They showed that insufficient mesh resolution produces sub-grid terms that have to be modeled. On the other hand, sufficient mesh resolution and detailed chemistry yields accurate combustion modeling. In general, insufficient resolution

produces sub-grid terms that are even more important than turbulence-chemistry interaction (TIC) effects.

In a recent study, Chinnathambi et al. [101] performed a RANS simulation of auxiliary fuel injected TJI combustion system using CONVERGE [99]. The modeling results were compared with experimental data from a production based single cylinder thermodynamic engine under normally aspirated and boosted conditions at 2500 rpm engine speed. While the overall equivalence ratio of the main chamber was λ =1.8, direct injection of liquid gasoline in the prechamber created locally rich conditions at the time of spark. Their results showed that the prechamber peak pressure is a function of pre chamber volume, combustion condition and the nozzle diameter. They found that jets composed of hotter but complete combustion products are generated when a stoichiometric or slightly lean mixture is burned in the prechamber. In addition, as the nozzle's role is to accelerate the burning mixture and to quench the flame along the nozzle hole, the length and diameter of the nozzles are important TJI parameters. They mentioned that it is possible to target the jet penetration distance by varying the prechamber volume.

Chinnathambi et al. [101] used H₂O₂ as a precursor to locate the onset of knock. Further breakdown of H₂O₂ yielded smaller species such as OH, which was produced in the hotter regions. Due to the pressure created by the normal velocity of the flame propagation, an initial jet of unburned charge was pushed out of the nozzle followed by a jet of hot combustion products. This initial jet enhances the development of small turbulent structures in the main chamber. The hot jet was also a source of thermal energy in the main chamber which enhances active radical participation during chain branching ignition. The authors observed that richer than stoichiometric prechamber gases resulted in more active radicals compared to a double mass leaner prechamber charge.

Regarding the TJI system, Thelen et al. [27, 28, 29, 30], performed a propane-fueled TJI combustion simulation. RCM experiments used for validation. The simulation used RANS turbulent models to solve for the flow field and it used the SAGE chemistry solver with a detailed chemical kinetic mechanism for propane as the fuel. The simulation was validated and compared with the experimental TJI data for the MSU rapid compression machine. Chemistry has a considerable influence on in-cylinder pressure. In addition, Thelen's simulation permitted additional measurements of the initial stage of the TJI combustion process and gave insight into the flame behavior as it grew in the prechamber and passed through the nozzle. The latter quantifier could not be experimentally measured in the MSU RCM.

Similar to Thelen et al. [24], a mismatch of in-cylinder pressure between experimental and simulation results was reported by Brett et al. [102], who extended the Chemkin models [103] to study methane autoignition using thermodynamic and transport property databases. Pressure traces from the model and the experiment were compared, showing that the post compression peak pressures were over predicted by the models with an increasing deviation for higher peak pressures. The experimental ignition delay times exceeded predicted values when the model's compressed temperatures were below 1000 K. The experimental ignition delay only moderately exceeded predicted values for peak temperatures above 1000 K. In other words, ignition delays were predicted better than pressure rises.

Chapter 3 Experimental Set-up

The experiments for this thesis were performed on a RCM. This RCM was designed, built and characterized at Michigan State University (MSU) [104]. RCMs are often used to study the fuel decomposition and ignition behavior at high temperatures and pressures. The RCM provides an environment similar to an IC engine combustion chamber, while minimizing numerous complexities of an actual engine cylinder environment [65]. A schematic of RCM is shown in Figure 3-1.

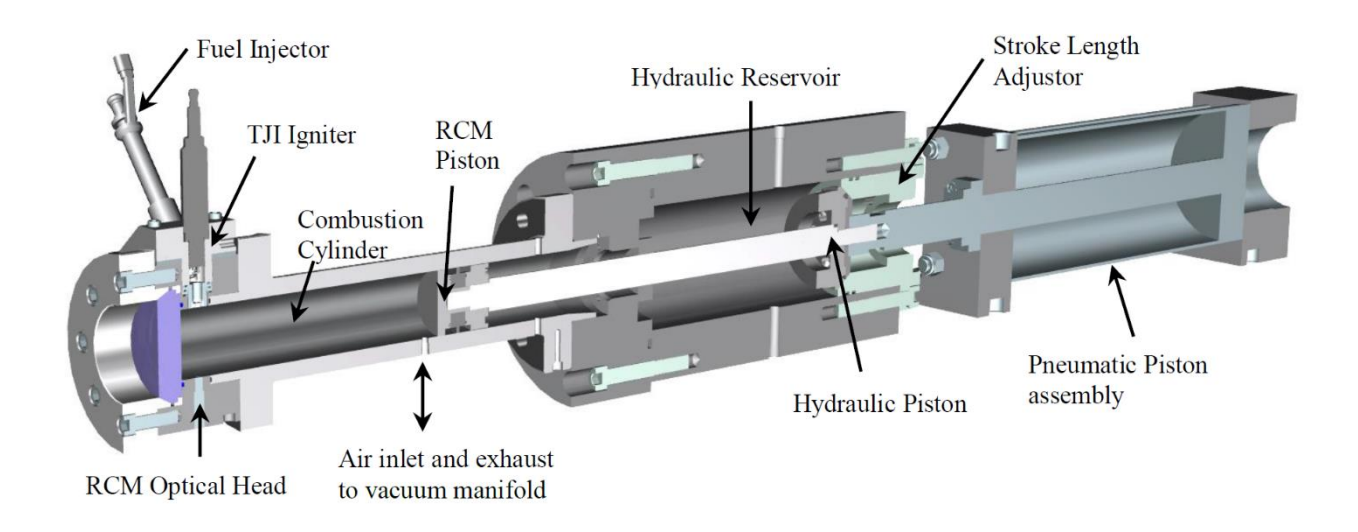


Figure 3-1- Schematic of RCM test facility.

The RCM consists of three pistons, the pneumatic piston, the hydraulic piston and the combustion chamber piston which are all on the same shaft. The combustion cylinder piston compresses the homogeneous fuel-air mixture and stops at top dead center (TDC) enabling combustion to occur at constant volume. The compression ratio of the RCM can be varied through the use of shims, which can adjust both the stroke length and/or the clearance volume yielding compression ratios in the range of 6-12. In general a creviced piston can be used to minimize the fluid motion and decouple the fluid dynamics from the chemical kinetics for autoignition studies. On the other hand,

a flat piston can be used where turbulence is desired. In this thesis, a flat piston is used. In the following experiments the presence of turbulent vortices increases the mixing rate and improves the combustion burn rate due to the higher entrainment of the main chamber mixture into the discharging jet.

In order to control and change the prechamber stoichiometry, air and fuel injectors are located in the prechamber. Figure 3-2 shows two schematics of the RCM combustion chamber and TJI system; (a) the prechamber spark plug TJI system with no injectors and (b) the dual-mode TJI device with air and fuel injectors. Dual-Model TJI facilitates prechamber stoichiometry control using separate air and fuel injection events during the compression stroke. It should be mentioned that the idea of Dual-Mode TJI has been patented by MSU [105].

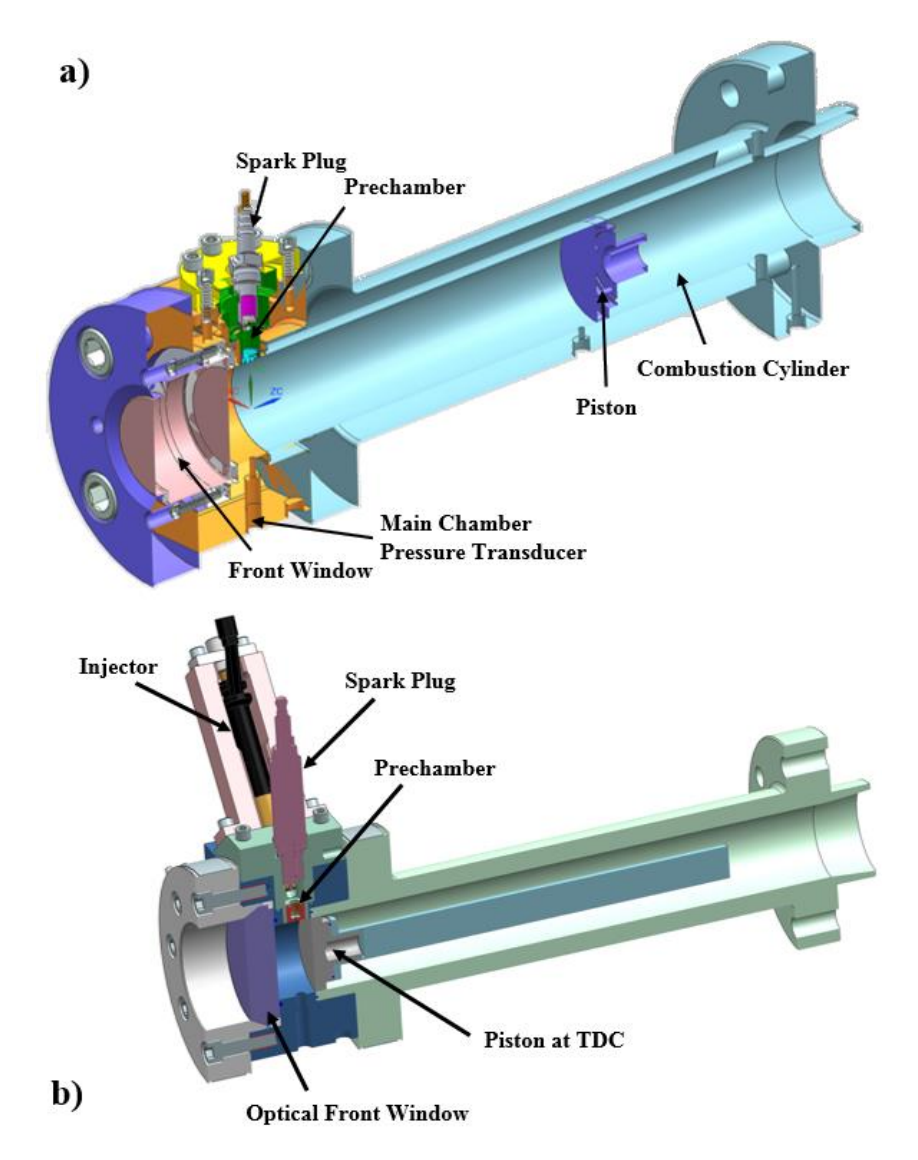


Figure 3-2- Cross sectional view of RCM combustion cylinder with TJI installed. a) No injector installed, b) Dual-Mode TJI.

In order to simulate the temperature in an engine, the combustion chamber walls were initially preheated to 80 °C (353 K) via band heaters that are installed on the RCM. LabView software monitors and controls the cylinder wall temperature. LabView software also records pressure data and generates/gathers control signals for the injection and spark events.

An insulation jacket reduces the heat transfer to the surroundings and maintains a quasi-steady temperature during the runs. In order to record the pressure data during combustion, a type 6125C

pressure transducer is installed in the main chamber and a 14 mm Kistler spark plug is installed in the prechamber. For a clear view of the entire cylinder bore, a sapphire (or fused silica, depending on the application) window is installed onto the combustion chamber and facilitates the combustion imaging with the high speed camera. Details of the RCM test facility are provided in Table 3-1.

Table 3-1- RCM experimental set-up

rable 3-1- RCM experimental set-up		
Cylinder Wall Temperature	80 °C	
Compression Ratio	8.5	
Cylinder Capacity	460 cm ³	
Clearance Volume	54 cm ³	
Piston Stroke Length	203.2 mm	
Cylinder Bore	50.5 mm	
Fuel Used	Methane	
TJI Prechamber Volume	4.75 cm ³	
Auxiliary Fuel Injector	Bosch Direct	
	Injector	

3-1 Combustion Visualization and High Speed Imaging

Combustion visualization of the experiments is performed with a Photron SA4 high speed color camera. Frame rates were between 10,000 and 20,000 frames per second with resolution was set at 512×512. A Nikon f/2.8 objective lens is coupled to the camera to record the combustion process.

A schematic picture of the camera and side view of the RCM is shown in Figure 3-3.

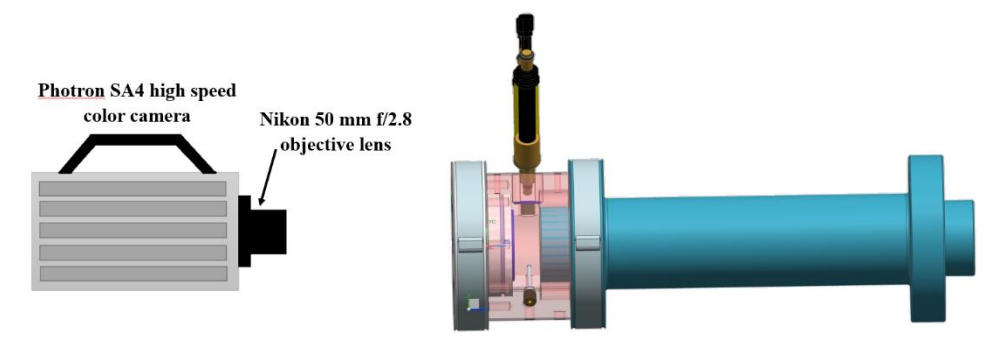


Figure 3-3- Optical set-up for color imaging. Imaging is end-on.

In each experimental test, the combustion chamber walls are pre heated to the desired temperature, normally 80 °C. Spark and auxiliary injection timing are set with the LabView control system. For a precise amount of fuel and air in the combustion chamber at the start of the test residual gases are vacuumed out of the system and the fuel and air (or diluent gas) are interred into the combustion chamber. The hydraulic chamber is then pressurized to 1000 psi to build a holding pressure and to prevent the piston from moving prior to the test. The pneumatic piston is pressurized to 140 psi. The camera begins recording once the control signal is sent. A control signal is then sent by LabView to the solenoid valve to vent the hydraulic fluid, which begins the compression process. The combustion piston stops at TDC producing a compressed air-fuel mixture at elevated pressure and temperature.

Shortly after compression (~1-5 ms at TDC) a control signal triggers the camera and the spark. (In some tests, separate signals are sent to the injector(s)). After the test, the piston is brought back to BDC manually and the gases are vacuumed out to prepare the system for the next test.

Chapter 4 Numerical Procedure

In order to gain a better understanding of combustion in the TJI system, Computational Fluid Dynamics (CFD) can be used to obtain valuable information. This includes the flow velocity, the turbulent intensity of the jet and the flame characteristics that are not easily experimentally measurable. According to Sagaut [106], CFD is "the study of the fluids in flow by numerical simulations". One major concern in finding appropriate algorithms for numerical solutions to the equations is to reduce the levels of error.

The fluid flow in the combustion cylinder of the RCM is a compressible, chemically reacting, transient flow that requires a 3-D simulation. In addition, moving boundaries (piston motion) makes the geometry complicated. Conservation of mass, balance of momentum and energy conservation describe the dynamics of the fluid flow and are solved in combination with constitutive equations for the transport of passive scalars, chemical species, and turbulence. The compressible equations for mass and momentum transport are as follows;

$$\frac{\partial \rho}{\partial t} + \frac{\partial \rho u_i}{\partial x_i} = S \tag{4-1}$$

$$\frac{\partial \rho u_i}{\partial t} + \frac{\partial \rho u_i u_j}{\partial x_j} = -\frac{\partial P}{\partial x_i} + \frac{\partial \sigma_{ij}}{\partial x_j} + S_i,$$

$$4-2$$

where the stress tensor is given by

$$\sigma_{ij} = \mu \left(\frac{\partial u_i}{\partial x_j} + \frac{\partial u_j}{\partial x_i} \right) + (\mu - 2/3\mu) \left(\frac{\partial u_k}{\partial x_k} \delta_{ij} \right).$$
 4-3

In these equations, u is the velocity, ρ is the density, S is the source term, P is the pressure, μ is the viscosity, $\dot{\mu}$ is the dilatation viscosity (set to zero) and δ_{ij} is the so-called Kronecker delta [107]. Mass and momentum equations contain a source term. The source term S for the mass equation may be attributed to evaporation and other sub models, while the momentum equation source term S_i comes from the gravitational acceleration, spray coupling, the mass source, etc. Since a

turbulence model is activated in the simulation of the flow, the turbulent viscosity is used in the place of viscosity, which is a function of the turbulent model constant, C_{μ} , the turbulent dissipation rate, ϵ , and the turbulent kinetic energy, k. viz.,

$$\mu_t = \mu + C_\mu \rho \frac{k^2}{\varepsilon}. \tag{4-4}$$

To solve for the compressible flow, an equation of state is also needed. For these simulations, the Redlich-Kwong equation of state [108] is used in which the compressibility factor is a function of temperature, pressure, critical temperature, and critical pressure. Details of this equation can be found in [99]. It should be noted that in order to satisfy the equation of state, Converge uses the PISO algorithm [109].

The compressible form of the energy equation is

$$\frac{\partial(\rho e)}{\partial t} + \frac{\partial(\rho e u_j)}{\partial x_j} = -P \frac{\partial u_j}{\partial x_j} + \sigma_{ij} \frac{\partial u_i}{\partial x_j} + \frac{\partial}{\partial x_j} \left(K \frac{\partial T}{\partial x_j} \right) + \frac{\partial}{\partial x_j} \left(\rho D \sum_m h_m \frac{\partial Y_m}{\partial x_j} \right) + S, \tag{4-5}$$

where $Y_{\rm m}$ is the mass fraction of specie m, $h_{\rm m}$ is the species enthalpy, D is the mass diffusion coefficient, e is the specific internal energy, T is the temperature and S is the source term [107]. Again, similar to the viscosity, the mixture conductivity is replaced with the turbulent conductivity;

$$K_t = K + C_p \frac{\mu_t}{P_r},\tag{4-6}$$

where K_t is the turbulent conductivity and Pr is the Prandtl number. The first term on the right hand side of Eq. 4-5 is the pressure work term. This term is zero for incompressible flows. The second term is viscous dissipation, which accounts for the dissipation of the kinetic energy into heat by the action of viscosity. The third term is the heat added to the fluid per unit mass (Fourier's Law). The fourth term, the species diffusion term, accounts for energy transport due to species diffusion. The last term, the source term, accounts for the external energy sources (such as the

deposited energy from the spark), chemistry (e.g., combustion) and turbulent dissipation for turbulent flows.

Next is the species transport equation, which solves for the mass fraction of all species in the domain. The compressible form of the species conservation equation is given by [99],

$$\frac{\partial \rho_m}{\partial t} + \frac{\partial \rho_m u_j}{\partial x_j} = \frac{\partial}{\partial x_j} \left(\rho D \frac{\partial Y_m}{\partial x_j} \right) + S_m, \tag{4-7}$$

where

$$\rho_m = \rho Y_m. 4-8$$

The molecular mass diffusion coefficient, D, is calculated by

$$D = \frac{\vartheta}{Sc},\tag{4-9}$$

where Sc is the Schmidt number and ϑ is the viscosity. Similar to the turbulent viscosity and conductivity, when a turbulent model is active, the turbulent mass diffusion coefficient should be used,

$$D_t = \frac{\vartheta_t}{Sc_t}.$$

The source term S_m in Eq. 4-7 accounts for evaporation, chemical reactions (combustion) and other sub-models [99]. In addition, a passive equation can be coupled to the species balance equations in order to solve for a passive scalar, if necessary (e.g., soot models).

4-1 Turbulent Transport

Due to the non-uniform mixing in the combustion chamber prior to ignition, the turbulent flow is highly transient. Subsequently, inhomogeneity of the equivalence ratio during ignition in the prechamber can produce variations in the ignition characteristics and flame propagation rate [110]. To solve the unsteady Navier-Stokes equations with the maximum quality of the results, all space-

time scales of the solution must be taken into account. If the simulation is discretized in steps Δx in space and Δt in time, they must be smaller than the characteristic length and time scales associated with the smallest dynamically active scales of the exact solution.

With Direct Numerical Simulation (DNS) all flow scales can be resolved, however, the excessive computational cost is a preventive reason for using DNS in practical engine simulations. To compute the solution, it is necessary to reduce the number of operations and no longer solve the dynamics of all scales of the exact solution. This leads to a new, coarser level of description of the fluid system. For this reason the RANS and Large Eddy Simulation (LES) approaches are more commonly used for complicated engine combustion simulations.

The non-linearity of the Navier-Stokes equations reflects the dynamic coupling that exists among all scales of the solution, which implies that these scales cannot be calculated independently. If a quality representation of the resolved scales is desired, their interactions with the scales that are not resolved must be considered in the simulation. This is achieved by introducing additional terms in the equations governing the evolution of the resolved scales. If the statistical average of the solution is calculated directly, the method is called Reynolds Average Numerical Simulation (RANS),

$$u(x,t) = \langle u(x,t) \rangle + \dot{u}(x,t), \tag{4-11}$$

where u(x,t) is the exact solution of u, $\langle u(x,t) \rangle$ is the statistical average and u(x,t) is the fluctuation part that will be included by a turbulent model. The statistical average is often associated with the time averaging;

$$\langle u(x,t)\rangle \approx \tilde{u}(x) = \lim_{T \to \infty} 1/T \int_0^T u(x,t)dt$$
 4-12

The statistical character of the RANS solution approach prevents a fine description of the physical mechanisms. The RANS approach applies ensemble averaging to the governing equations, hence,

the local unsteadiness of the flow is not predicted [106]. A symbolic representation of the energy spectrum decomposition associated with RANS is shown by Sagaut [106] and repeated here in Figure 4-1.

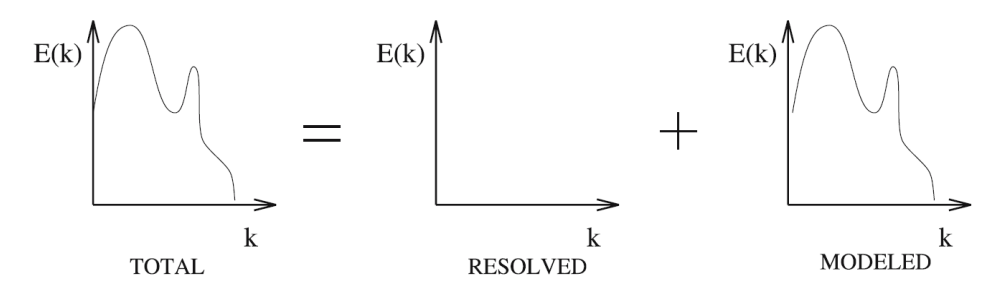


Figure 4-1- Energy spectrum decomposition, associated with the Reynolds Averaged Numerical Simulation from Sagaut 1998 [94].

Many global flow characteristics such as spray penetration, ignition delay time, pressure data and heat release rates can be fairly well predicted by RANS approaches. For this reason the RANS RNG k- ε turbulence model [111] was chosen for the simulation of the TJI system. In order to provide closure to the Reynolds stress term, the transport equations for the turbulent kinetic energy, k, and the turbulent dissipation, ε , that are provided here, must be solved along with the concept of an eddy viscosity.

$$\frac{\partial \rho k}{\partial t} + \frac{\partial \rho u_i k}{\partial x_i} = \sigma_{ij} \frac{u_i}{\partial x_j} + \frac{\partial}{\partial x_j} \left(\frac{\mu}{P r_{tke}} \frac{\partial k}{\partial x_j} \right) - \rho \varepsilon + S, \tag{4-13}$$

$$\frac{\partial \rho \varepsilon}{\partial t} + \frac{\partial (\rho u_i \varepsilon)}{\partial x_i} = \frac{\partial}{\partial x_j} \left(\frac{\mu}{P r_{\varepsilon}} \frac{\partial \varepsilon}{\partial x_j} \right) - c_{\varepsilon 3} \rho \varepsilon \frac{\partial u_i}{\partial x_i} + \left(c_{\varepsilon 1} \frac{\partial u_i}{\partial x_j} \sigma_{ij} - c_{\varepsilon 2} \rho \varepsilon + S \right) \frac{\varepsilon}{k} - \rho R,$$

$$4-14$$

where the stress tensor is

$$\sigma_{ij} = 2\mu_t S_{ij} - \frac{2}{3} \delta_{ij} \left(\rho k + \mu_t \frac{\partial u_i}{\partial x_i} \right)$$
 4-15

The turbulent viscosity, μ_t , is calculated from Eq. 4-4. The quantities $c_{\epsilon 1}$, $c_{\epsilon 2}$, $c_{\epsilon 3}$ are the model constants. More information on the turbulent models is provided in [99].

In addition to the RANS model, an LES turbulence model is used to perform numerical simulations. LES utilizes space-averaged (filtered) equations to model small eddies with large eddies solved directly. Based on Sagaut [106], the LES approach relies on the definition of large and small scales. In general, a set of *ad hoc* governing equations is solved on a computational grid that is too coarse to represent the smallest physical scales. In the explicit Large Eddy Simulation approach, an extra forcing term referred to as a sub-grid model is introduced in the governing equations to cancel the resolution error. The symbolic representation of the energy spectrum decomposition in the solution where an LES approach is used is shown in Figure 4-2.

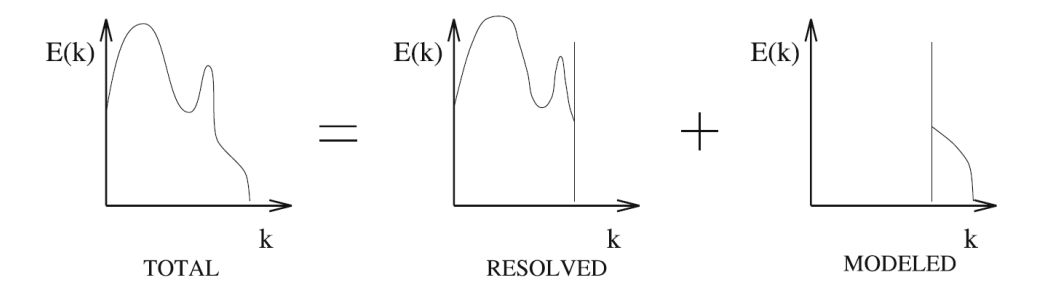


Figure 4-2- Energy spectrum decomposition, associated with Large Eddy Simulation. From Sagaut 1998 [94]. Compare with Figure 4-1.

In order to handle the equations and derive the subgrid models, scale separation is achieved mathematically, normally using band-pass filtering. For easier analysis, homogeneous isotropic filters are used in the current framework. The properties of an isotropic filter are independent of the position and orientation of the spatial frame of reference, meaning that it is applied to an unbounded domain and the cutoff scale is constant and identical in all spatial directions [106]. Three typical filters that are normally used are the top-hat, Gaussian and sharp Fourier cut-off filters [112]. In LES the scales of turbulent flow are separated by using a scale high-pass filter i.e. low-pass in frequency. The mathematical representation of the filter is a convolution product,

$$\overline{\Phi}(x,t) = \int_{-\infty}^{\infty} \int_{-\infty}^{\infty} \Phi(\xi,t) G(x-\xi,t-t) dt d^{3}\xi,$$
4-16

where $\overline{\Phi}(x,t)$ is the resolved part of a space-time variable $\Phi(x,t)$. The convolution kernel, G is the characteristic of the filter used and is associated with the cutoff scales in space $(\overline{\Delta})$ and time $(\overline{\tau}_c)$. More details of the convolution product in Fourier space and other filters are found in [106]. Since LES implies spatial filtering of the governing equations, the large flow structures are captured based on the filter size. The unresolved scale flow structures are modelled. Various LES modeling approaches can be found in [106, 113].

To obtain the large-eddy simulation formulation, the homogeneous filter verifying the properties of linearity, conservation of constants and commutation with derivation is applied to the Navier-Stokes equations. The filtered Navier-Stokes equations in physical space are as follows,

$$\frac{\partial \overline{u}_i}{\partial t} + \frac{\partial}{\partial x_j} \left(\overline{u_i u_j} \right) = -\frac{\partial \overline{P}}{\partial x_i} + \nu \frac{\partial}{\partial x_j} \left(\frac{\partial \overline{u}_i}{\partial x_j} + \frac{\partial \overline{u}_j}{\partial x_i} \right), \tag{4-17}$$

$$\frac{\partial \overline{u}_i}{\partial x_i} = 0. 4-18$$

Here \bar{P} is the filtered pressure, $\bar{u_i}\bar{u_j}$ is the non-linear term of the filtered momentum equation and must be expressed as a function of \bar{u} and u, which are related as $u = u - \bar{u}$. In order to decompose the non-linear term, Leonard decomposition [114] may be used. The non-linear terms can be expressed in the form of a triple summation. After some rearrangement and various simplifications, the filtered momentum equations are expressed as

$$\frac{\partial \overline{u}_i}{\partial t} + \frac{\partial}{\partial x_j} \left(\overline{u}_i \overline{u}_j \right) = -\frac{\partial \overline{P}}{\partial x_i} + \nu \frac{\partial}{\partial x_j} \left(\frac{\partial \overline{u}_i}{\partial x_j} + \frac{\partial \overline{u}_j}{\partial x_i} \right) - \frac{\partial \tau_{ij}}{\partial x_j}.$$

$$4-19$$

All terms that are not exclusively dependent on the large scales are grouped together in the sub grid tensor

$$\tau_{ij} = \overline{u_i u_j} - \overline{\overline{u}_i \overline{u}_j}. \tag{4-20}$$

More details on the sub grid tensor can be found in [106].

Among the many turbulence closure models, the Smagorinsky model was chosen for use in this thesis. The Smagorinsky model [115] is expressed as

$$\vartheta_{sgs}(x,t) = (C_s \bar{\Delta})^2 (2|\bar{S}(x,t)|^2)^{1/2}.$$
4-21

Here C_s is a theoretical constant whose value can be adjusted to improve the results. For the case of isotropic homogeneous turbulence, C_s =0.2 was used [116]. Deardorff [117] used C_s =0.1 for a plane channel flow. When the field gradient is non-zero, enforcement of the local equilibrium relation, requires reduction of the value of the constant, as noted here.

In order to solve the governing equations, the finite volume method is used in Converge, which numerically solves the integral form of the conservation equations and as a result, conserves the transport quantities for regular and irregularly shaped cells. However, it is hard to obtain higher order accuracy (i.e., above 2nd order accuracy). In addition, the pressure-velocity coupling in Converge is achieved using the predictor-corrector technique of Pressure Implicit with Splitting of Operators (PISO) (Issa [109]). In order to find the limit for the maximum time step used in Converge, several criteria are used. Three Courant-Friedrichs-Lewy (CFL) [118] numbers related to the convection, diffusion, and speed of sound are used to limit the time step size and to determine if under-relaxation is required. In addition, when the simulation has combustion, the time step will also be controlled by a chemical time scale which relates to the initial cell temperature and the change in temperature due to combustion. These numbers should be defined carefully in order to stabilize the numerical scheme without losing accuracy. Details of the numerical scheme and PISO algorithm are found in [99].

4-2 Computational Grid

The innovative gridding method of Converge allows the use of orthogonal grids which simplify the code numerics, while reducing the time and complexity of grid generation. Converge performs the actual grid generation internally at runtime and the user only needs to prepare surface file, based on the STereoLithography (STL) file of the geometry of interest from a Computer-Aided Design (CAD) package. Converge employs the cut cell Cartesian method which cuts the cells that are intersected by the surface. Two methods of grid refinement are provided in Converge, fixed embedding and Adaptive Mesh Refinement (AMR). Fixed local grid refinement is desirable to refine the grid in critical sections such as around the spark plug, injectors, and on the walls. This resolves the local complex flow behavior while other parts of the domain remain at the base grid size. For the purpose of the simulations a sphere shaped fixed embedding is introduced around the spark plug that is activated before the spark event and deactivated after the spark event. In addition, cone shaped embedding is introduced around the injectors during injection. Grid refinement around the spark plug is shown in Figure 4-3.

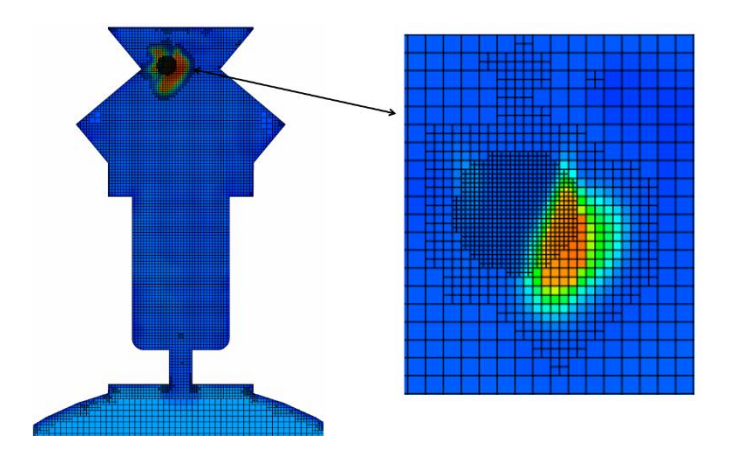


Figure 4-3- An example of generated grid with fixed embedding at the spark event.

Adaptive mesh refinement is used temporarily to refine the grids where high gradients of temperature or velocity appear. Grid scaling is a powerful tool to reduce the computer run time as it facilitates higher resolution where the flow structures need to be resolved in order to have higher accuracy, while a coarser grid is used where lower resolution is sufficient [99]. The AMR technique is helpful to refine the mesh at the flame front and during jet penetration while the cells away from the high velocity gradient regions or combustion vicinity remains at the base grid size. As a result, the total cell count for the simulation remains reasonable and the computer run time does not increase dramatically. An example of adaptive mesh refinement is shown in Figure 4-4.

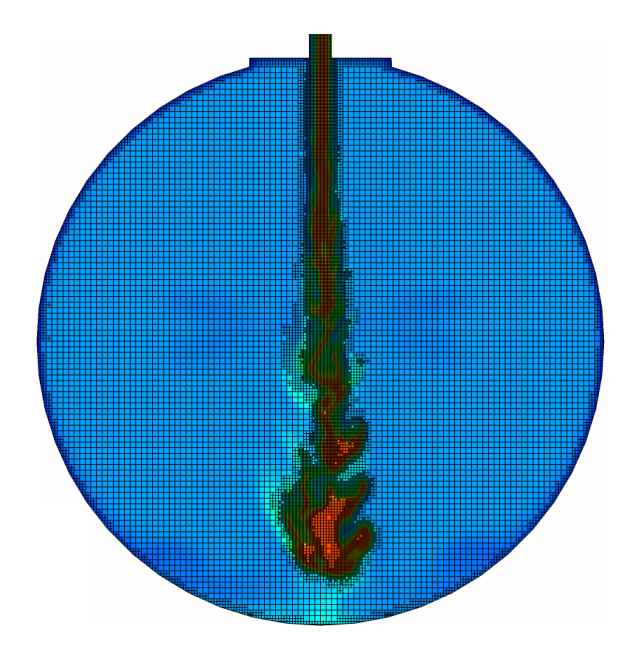


Figure 4-4- An example of generated grid with adaptive mesh refinement near the flame boundary during combustion.

The grid scaling tool in Converge facilitates the grid refinement or coarsening based on the grid scale level, using the following equation:

$$dx_{new} = dx_{orig} \times 2^{-(grid\ scale\ level)},$$
4-22

where dx_{new} is the new base cell size and dx_{orig} is the original base cell size in the code.

4-3 Combustion Modeling

Converge uses a detailed transient chemistry solver (SAGE) [119] to evaluate detailed chemistry in combustion simulations. The chemical kinetic mechanism enters the code in CHEMKIN-formatted files. To reduce the computational time for chemistry, Converge is equipped with a multi-zone method in which the computational cells with similar cell temperature, pressure and composition fall into the same category regardless of their original location in the domain. The set of chemistry equations is solved for each category and the updated cells are remapped to their original domain locations. Consequently, the computational time reduces substantially as the chemistry equations are solved for a group of cells and not for each cell individually.

Converge uses a well stirred reactor model in every individual cell. In other words, every computational cell is assumed to be a homogeneous zero-dimensional reactor given a mean quantity that is used to solve for chemistry. The validity of this approach is explained in detail in [100].

Since the number of species and reactions are a major concern, four detailed mechanisms, Sandiego [120], Aramco [121], GRI [122] and NUI [123], and a reduced mechanism were used and compared. Respectively, for the Sandiego, Aramco, GRI and NUI mechanisms, the number of reactions are 247, 1542, 325 and 1593 and the number of species are 50, 253, 53 and 293. In addition, the NUI mechanism was reduced using the Converge mechanism reduction tool for a range of temperatures, pressures and equivalence ratios. The final reduced mechanism has 122 reactions and 23 species. During mechanism reduction an effort was made to retain species such as OH and CH radicals, nitrogen components, CH₄, CO₂, O₂, H₂O and N₂ in the mechanism, in order for the reduced mechanism to be suitable for high N₂ dilution. The validity of the reduced

mechanism is restricted to the application for which it has been derived and is greatly dependent on the stoichiometry and pressure range [124]. Modeling the chemical reactions accurately is as important as turbulence modeling. To show the importance of the mechanism, various cases were run. The differences between the abovementioned mechanisms with regards to the burn duration and peak pressure were then compared. See section 7-2-1.

It is worth mentioning that since the full mechanism itself over predicts the experimental pressure traces at high pressures, the reduced mechanism may show the same discrepancies. The effects of reduced mechanisms were investigated by Honnet [125] and various ignition parameters were explored. It has been stated [125] that a reduced mechanism of 19 global reactions and 23 species could have the exact same burning velocity and ignition delay time as a full mechanism for a mixture of methane, oxygen and argon at stoichiometric conditions. Both detailed and reduced mechanisms were in a good agreement with the measurements [125].

4-4 Mechanism Reduction

The aforementioned mechanism reduction was performed using the zero dimensional utility tools in Converge. The computational time taken to obtain numerical solution is linearly proportional to the number of reactions or the square of the number of species. It is feasible to make the mechanism computationally efficient by reducing the number of species and reactions while maintaining solution accuracy. The Converge mechanism reduction tool runs in a zero-dimensional spatially uniform chemical reactor. The precision of quantitative agreement between the reduced and full mechanisms sets the limit on mechanism reduction. Converge uses a Direct Relation Graph with Error Propagation and Sensitivity Analysis (DRGEPSA) [126] to generate reduced mechanisms.

Automatic mechanism reduction is based on the DRG theory as devised by Lu and Law [127]. Based on DRG, a user-defined threshold is defined to determine which species are retained in the reduced mechanism. The DRGEPSA consists of two phases: (1) DRGEP and (2) Sensitivity Analysis (SA). For a given range of initial temperatures, pressure and equivalence ratios, a set of sample points are selected at 10K intervals. For each sample point, model coefficients are calculated and a skeletal mechanism is generated. Autoignition simulations are performed for each of the resulting skeletal mechanisms and the maximum errors in the ignition delay values are compared with detailed chemistry values. The smallest mechanism with the minimum ignition delay error is defined as the optimal mechanism. The sensitivity analysis reduces the size of the mechanism and calculates the error in ignition delay caused by the removed species from the DRGEP-generated skeletal mechanism. Additional details of the DRG method can be found in [99].

In order to make sure that the reduction technique does not affect the results, the ignition delay analysis was performed and pressure traces were compared with the experimental measurements and four other full mechanisms.

To start combustion, the spark was modeled as a two-step source of energy (100 mJ) added in a small sphere (radius of 0.5 mm) over the time intervals 0.1 and 1 ms. The internal energy was added to the energy equation during the run and the modeled spark timing was set equal to its experimental counterpart. Spherical embedding was employed around the spark plug gap to resolve the local computational domain.

4-5 Monitor Points

To record the flow variables and temperature fields in the CFD simulations, monitor points were placed in the nozzle throat and main chamber. Monitor points are locations where customized output values are collected. They can be a single point or a sphere of a defined radius. The location of the monitor points and flow variables monitored during the run, such as velocity magnitude or density, are defined as User-Defined-Functions (UDF) in Converge. Figure 4-5 shows the location of the monitor points in the main chamber and nozzle throat. Here, the entrained jet velocity in the main chamber (aligned with the nozzle flow axis) and flow velocity in the nozzle throat were recorded at the monitor points, see Chapter 8. Furthermore, the line-of-sight jet penetration speed was compared with measurements from the experimental images.

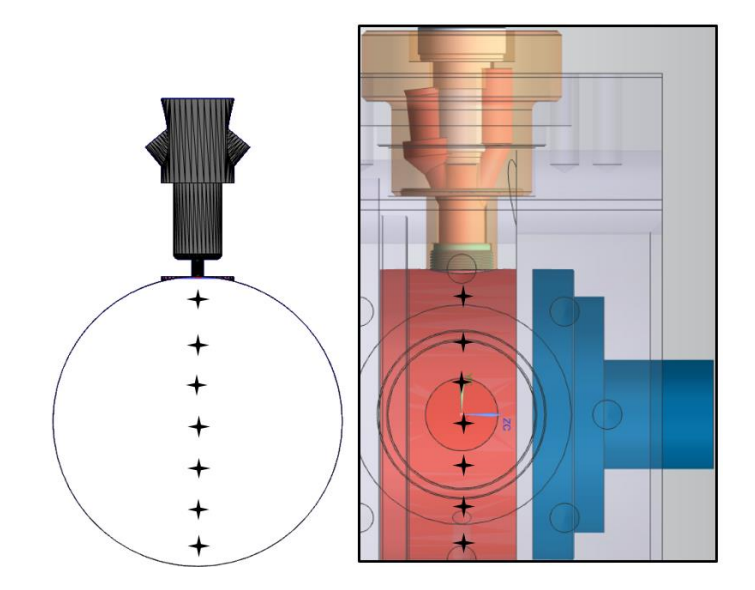


Figure 4-5- Location of the monitor points in the main chamber.

4-6 Simulation Geometry

Cavity geometry of the RCM combustion chamber at BDC (right), and its front view (left), generated in SolidWorks is shown in Figure 4-6. The cavity model defines the fluid domain within the RCM and TJI system.

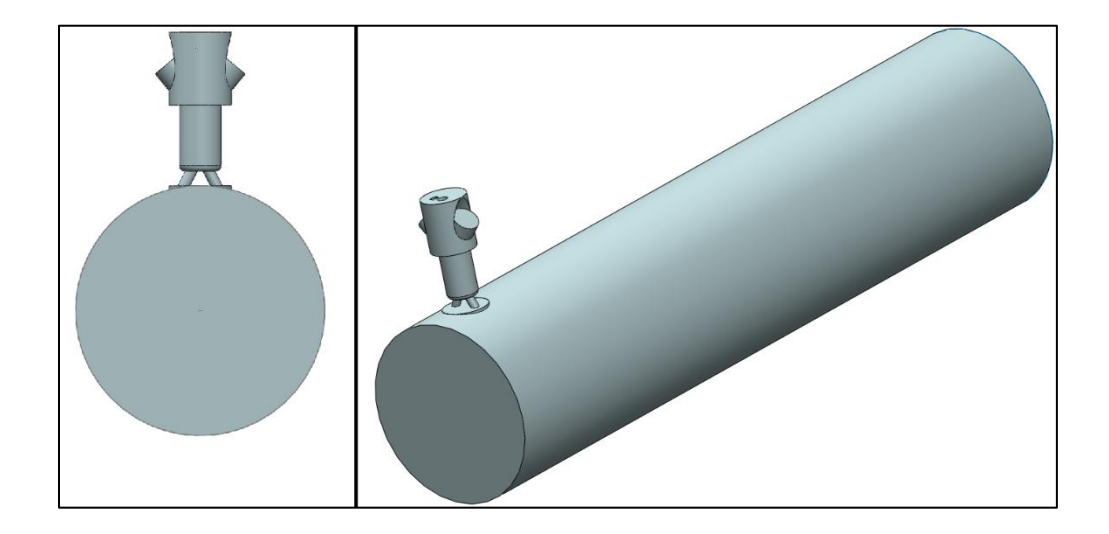


Figure 4-6- Cavity geometry of RCM combustion chamber and TJI system assembly, generated in SolidWorks Left (end-on-view); right (3/4 view).

The STL file then is transferred to the Converge visual studio and the triangulated surface file is generated and boundaries are defined as shown in Figure 4-7. Converge uses the supplied closed triangulated surface to cut the cells that are intersected by the surface [99]. It should be noted that the surface file is modified to simplify the geometry to a more convenient form for CFD simulation.

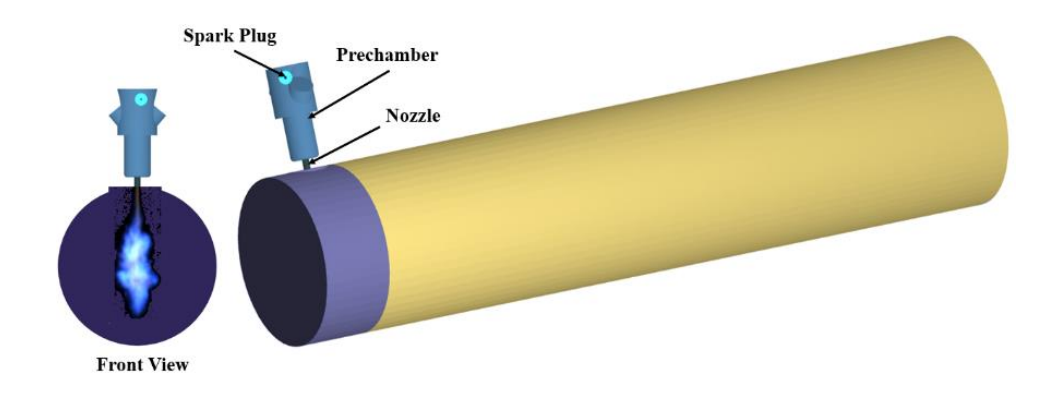


Figure 4-7- Surface file of RCM combustion chamber plus TJI system.

The absence of combustion during the compression stroke enables the simulation of the compression process to take place with a coarser grid (i.e., $4\times4\times4$ mm grid size) up to the point where the piston stops at TDC. Following compression, the field variables at TDC are mapped to a finer base grid size of $2\times2\times2$ mm.

The initial conditions for the simulations are provided in Chapter 5 to Chapter 9. The initial pressure and temperature remain constant at 1.04 bar and 80 °C, respectively, similar to the experimental test conditions. A no-slip velocity and isothermal temperature conditions are chosen for all boundaries.

The piston velocity profile is extracted from the measured pressure traces assuming an isentropic compression process and known initial volume (V₀) and pressure (P₀) as well as compressed pressure (P). Once the time dependent volume is calculated from the polytropic expression ($V(t) = V_0[P_0/P_0(t)]^{1/n}$), the time varying velocity calculation is simple: $v(t) = \left[\frac{dV(t)}{dt}\right]\pi D^2/4$, where D is the diameter of the reaction chamber. The assumption of polytropic compression was used in previous RCM studies [23, 24, 96, 128]. An example of the piston movement profile is shown in Figure 4-8. The (0,0) on the plot is an indication of piston location at BDC position. The piston reaches TDC 31 msec later.

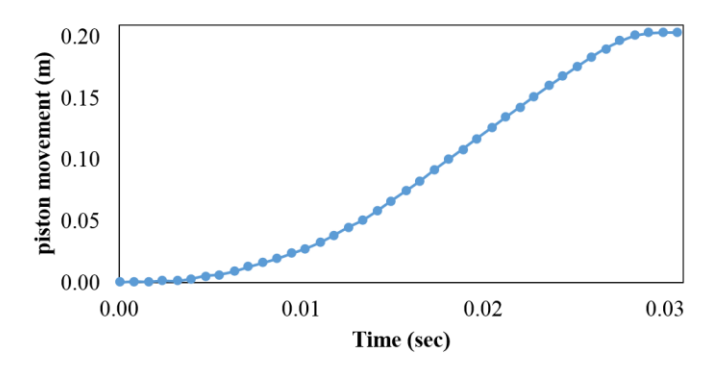


Figure 4-8- Piston motion function used to define the piston location at each time step. TDC is afterward at 31 msec.

The gaseous phase injection process is simulated as a single hole inlet and the duration of injection, injector back pressure, and the amount of injected mass were matched to the experiments. To model this, an inlet boundary condition is assumed at the location of the injectors that is as wide as the injector hole area, and the profile of injected mass is supplied as an inlet condition. Methane was injected in the gaseous phase in the experiments and is modeled in the form of gas in this thesis. For this reason the droplet break-up, spray and collision models available in Converge were not employed.

Figure 4-9 shows the planar surface located in the y-z plane that passes through the centerline of the orifices. Contours of the numerical results that are provided in the following chapter are shown on this plane. It is also an example of grid refinement due to fixed embedding in the vicinity of the walls. The x-direction is aligned with the combustion cylinder where the piston is moving toward the negative x direction.

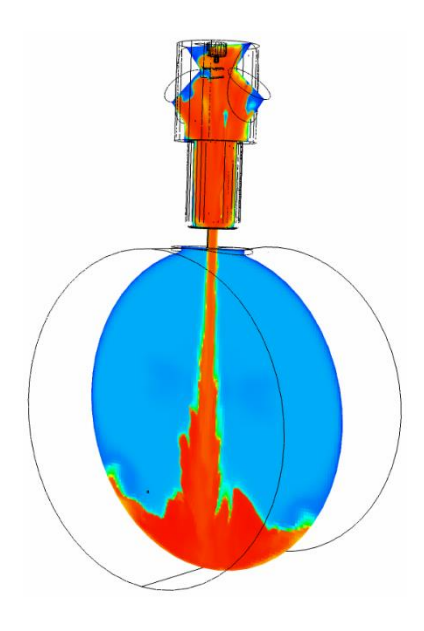


Figure 4-9- Clip plane location used for the simulation contours passing through the pre and main chambers and the nozzles.

Chapter 5 CFD Modeling of a Methane Fueled Turbulent Jet Ignition System with N_2 Dilution in a Rapid Compression Machine

Three-dimensional numerical simulation of the turbulent jet ignition combustion process of a premixed methane-air mixture in a Rapid Compression Machine (RCM) was performed using the Converge computational software. A RANS model, which included a k-ɛ turbulence model to solve the mean flow and the SAGE chemistry solver with a reduced methane mechanism to solve the chemistry, was used to model the turbulent jet ignition system.

This thesis investigates the impact of an auxiliary fueled prechamber on the burn rate and on the lean or dilute limit extension of the RCM. The numerical results are compared to data and optical images obtained from high speed imaging of combustion in the optically accessible RCM.

5-1 Results

The simulations of the present study were run in parallel using up to 80 processors on Michigan State University's High Performance Computing Center (MSU HPCC). Maximum cell counts vary during the simulation based on changes in geometry and the amount of AMR used. Specifications of the simulation cases are summarized in Table 5-1. As mentioned before, initial conditions of the simulations, such as the initial pressure, temperature and mixture fractions were adjusted to the conditions of the experimental tests. One purpose of the experiments was to find the N₂ dilution limit, consequently only tests with 35 % and 40 % dilutions are performed in the RCM. A second purpose was to show the effect of the prechamber auxiliary injection on combustion. As a result, a set of experiments with 40% N₂ dilution were performed in which 4% auxiliary air and fuel at stoichiometric conditions were injected into the prechamber during the compression stroke. The initial pressure of the combustion cylinder at BDC was 1.04 bar, the initial temperature was 80 °C

and the overall air-fuel ratio for all of the tests was stoichiometric (note the AFR of stoichiometric methane is \sim 17)

Table 5-1 Test specifications.

λ	% N ₂ dilution	% Aux_injection
1	0	0
1	20	0
1	35	0
1	40	0 and 4

The percentage of nitrogen dilution and the auxiliary injected mass are calculated from Eqs. 5.1 and 5.2 respectively.

$$N_2 dilution \quad \% = \frac{m_{_{N2}}}{m_{_{air}} + m_{_{CH4}} + m_{_{N2}}} \times 100 \,, \label{eq:N2}$$

Auxiliary_injection
$$\% = \frac{(m_{CH4} + m_{air})_{injected}}{(m_{air} + m_{CH4} + m_{N2})_{total}} \times 100$$
.

Here m_{air} , m_{CH4} and m_{N2} are the initial mass of air, fuel and nitrogen, respectively, and are calculated based on the initial pressure, volume, temperature and λ using the ideal gas equation of state. Note also that the additional N_2 used for the dilution does not contribute to the calculation of the equivalence ratio.

Figure 5-1 shows the main chamber pressures of the experimental tests with different percentages of nitrogen dilution. The compressed pressure is ~ 15.5 bar and the combustion peak pressure depends on the percentage of N_2 dilution in the mixture. The dilution limit for successful combustion achieved experimentally was 35%, however, increase of the N_2 dilution significantly increased the ignition delay time and decreased the combustion peak pressure. Further increases

of N₂ dilution to 40% resulted in unstable combustion with only 30% of the attempted tests being successful. The pressure trace for this case also shows a very long ignition delay time. Injection of a very small amount of fuel and air into the prechamber creates a less diluted environment in the prechamber, which facilitates prechamber combustion and accelerates flame propagation. Accordingly, main chamber combustion improves significantly. Although auxiliary injection enhances the diluted mixture combustion, the injection timing and ideal amount of fuel and air to be injected play a vital role in combustion improvement.

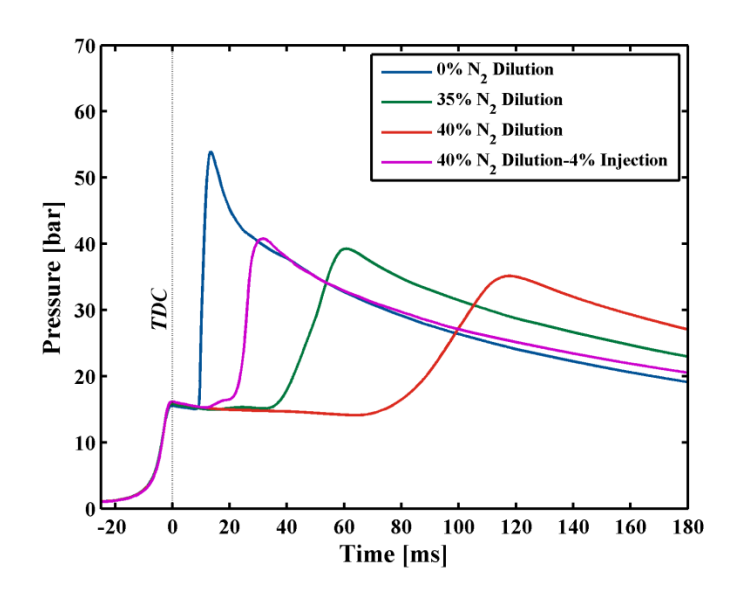


Figure 5-1- Experimental traces of the main chamber mean pressures.

Figure 5-2 shows the mean pressure traces in the main chamber from the CFD simulations. While the spark timing varies from case to case, the time datum in this figure is set to correspond to TDC. The simulation pressures show similar behavior to the corresponding experimental results (Fig. 5-1) and are in complete agreement in compression and the early stages of combustion. However, the maximum experimental pressure rise is less than the corresponding numerical values for several reasons. One reason is the existence of crevice volumes in the experimental set up, which trap unburned fuel that does not combust. In the simulation, the crevices are removed as they

increase the computational cost. Further details are provided in Appendix D. Another reason mentioned previously, is that the kinetic model loses accuracy at higher pressures.

Similar to Figure 5-3, numerical results in Figure 5-4 show that the stoichiometric condition has the highest peak pressure and diminished ignition delay time compared to the N_2 diluted mixtures. The peak pressure decreases as the percentage of dilution increases. Numerical results show that the increase in dilution from 20 to 35 percent results in a change in combustion rate and consequently ignition delay time. Increasing dilution to 40% yields no combustion, in agreement with the majority (70%) of the experimental results for this case. The N_2 dilution limit was found to be \sim 35% in both the numerical and experimental results. Similar to the experiments, ignition enhancement was achieved by injecting a small percentage of the fuel and air into the prechamber. Although the combustion peak pressure and burn rate are not close to the case of the stoichiometric condition, the improvement is noticeable. The effect of injection timing and the amount of injected mass on the combustion process of an iso-octane fueled prechamber with a premixed main chamber charge is a topic of current and future study.

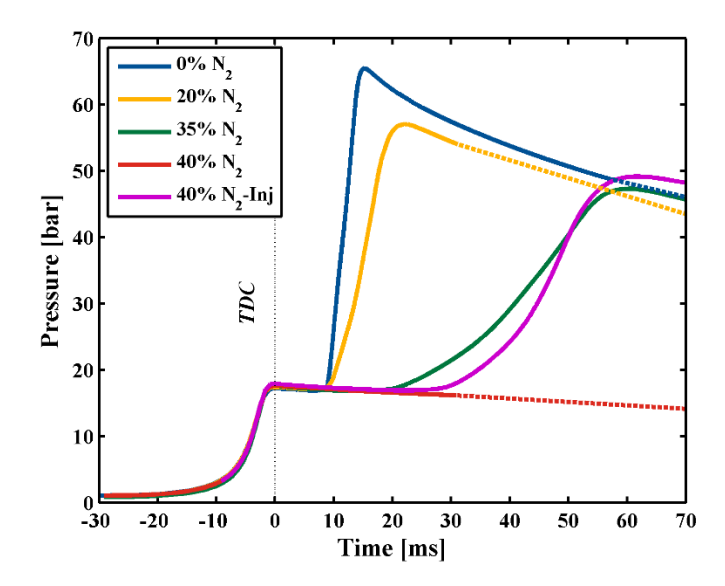


Figure 5-2- Numerical traces of the main chamber mean pressure. The projected pressure losses are shown in dashed lines. (The progress of numerical simulations were run up to the completion of combustion and did not include the entire heat loss process).

RANS simulations of the TJI process were carried out up to 90 ms. Numerical images of the OH radical mole fractions are shown in Figure 5-3 to Figure 5-6. The contours are compared to the experimental images and show the different stages of jet penetration in the main chamber, flame surface development, and ignition processes. In order to facilitate the comparison of the experimental images to the numerical contours, a time datum was chosen to coincide with the first image in which the hot gas jet enters into the main chamber. It should be noted that utilization of image enhancement improves the visibility of the initial faint jet at the moment of entrance.

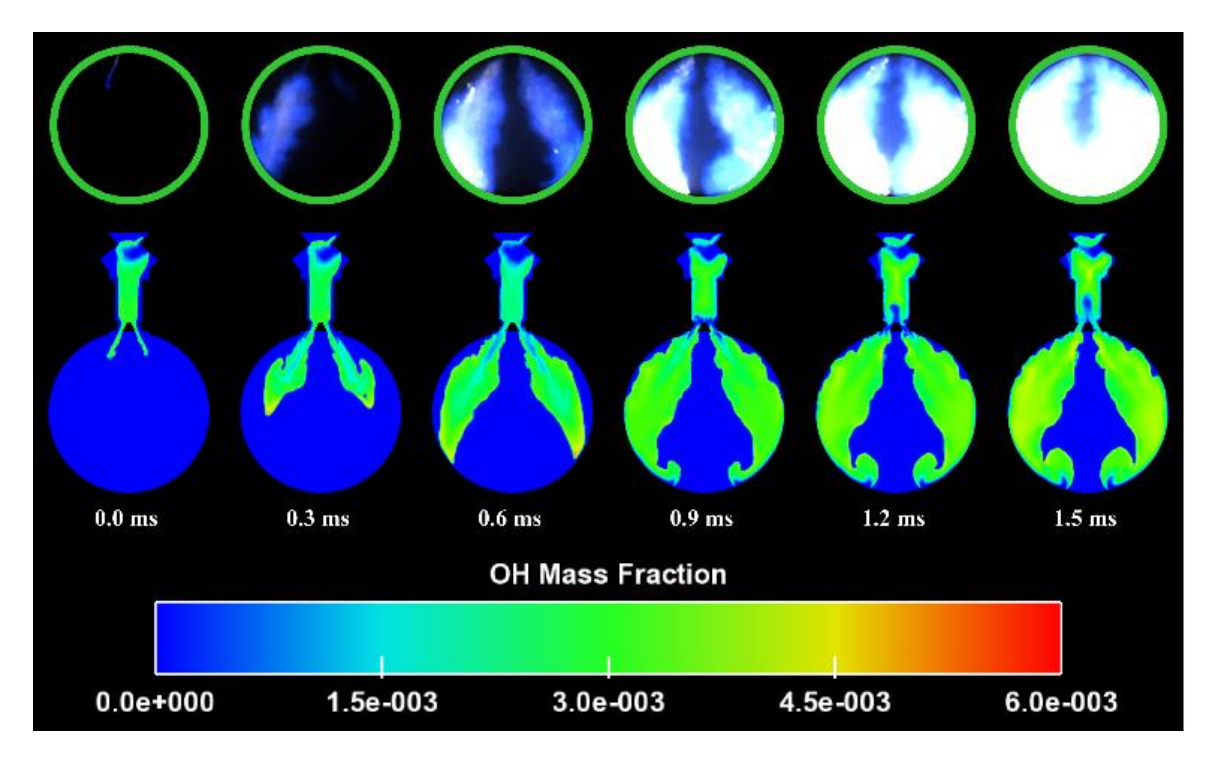


Figure 5-3- Optical images achieved during the experimental tests compared to the OH radical mass fraction contours of the simulation for λ =1.0 and no N_2 dilution.

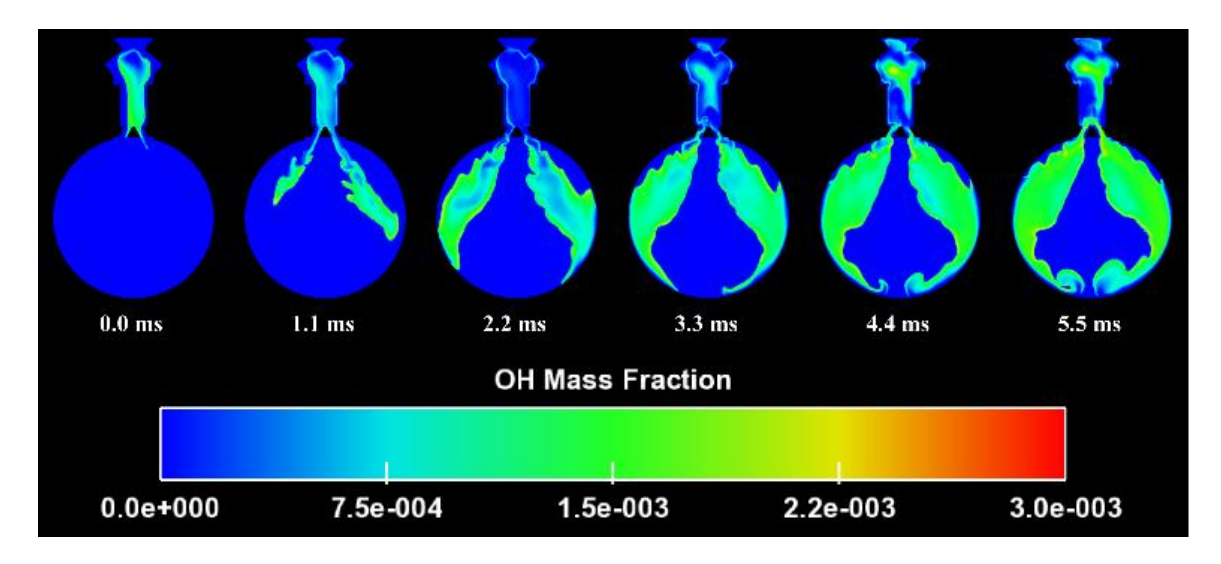


Figure 5-4- OH radical mass fraction contours of the simulation for λ =1.0 and 20% N_2 dilution.

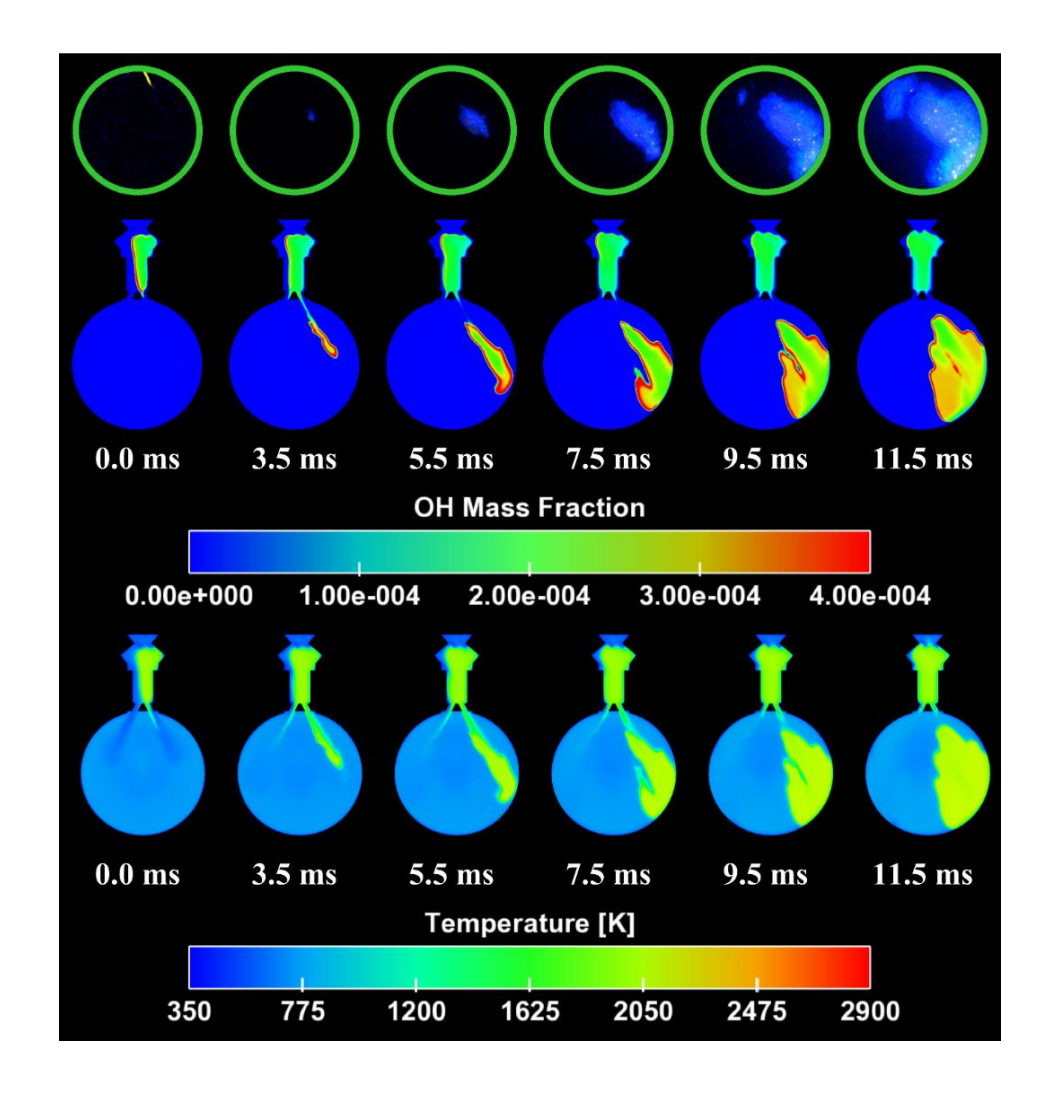


Figure 5-5- Optical images achieved during the experimental tests compared to the OH radical mass fraction contours of the simulation for λ =1.0 and 35% N_2 dilution.

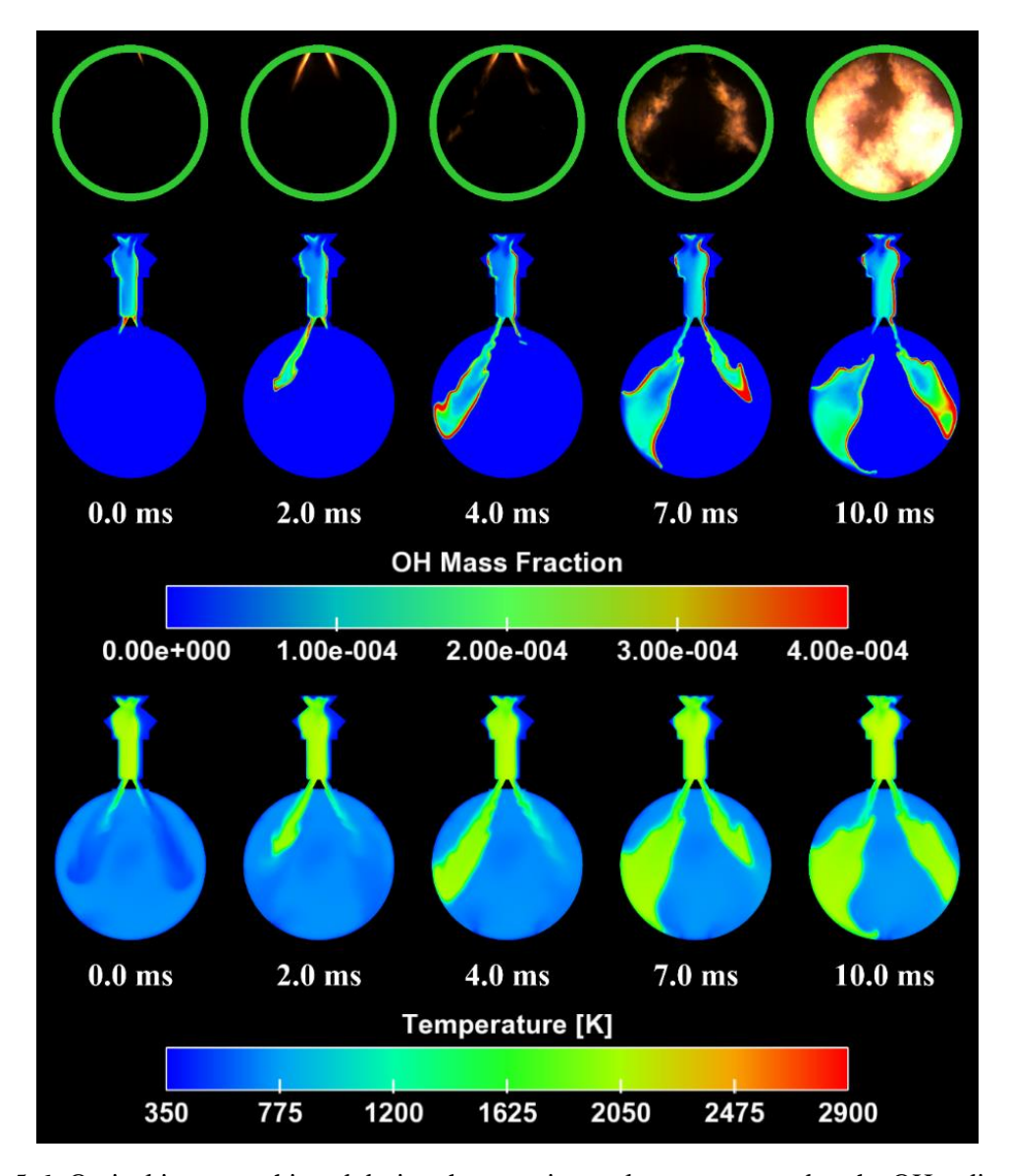


Figure 5-6- Optical images achieved during the experimental tests compared to the OH radical mass fraction contours of the simulation for λ =1.0 and 40% N_2 dilution with 4% auxiliary air/fuel injection in the prechamber.

Figure 5-3 to Figure 5-6 show that due to the high percentage of N_2 dilution, the prechamber combustion and flame development is delayed, as a result, the main chamber combustion is also delayed. 50% mass fraction burn durations for the no dilution case takes place in 1.5 ms while this time duration is almost three times longer with 20% dilution and eight times longer with 35% N_2 dilution. In addition, the symmetry of the flame propagation decreases with increased N_2 dilution,

and for the case of 35 % dilution, only one jet is visible and not strong enough to ignite the main chamber mixture quickly.

Experiments show that the N_2 dilution limit is ~35% since only 30% of the experiments with 40% N_2 dilution were successful. In the same manner, numerical simulation of the case with 40% dilution shows no combustion due to the insufficient turbulence intensity in the prechamber to help the flame propagation at the time of the spark event. However, injection of a small amount of fuel and air in the prechamber results in having two strong jets in the main chamber and noticeably increases the chance of successful combustion and enhances ignition. Figure 5-6 shows these improvements. It should be noted that simulation results show a much longer combustion duration compared to the experiments. As it is shown in the experimental images of Figure 5-6, after 13.5 ms, the experimental main chamber mixture combusted completely while the modeling results show that only half of the main chamber mixture is combusted by this time. This discrepancy may be due to the reduced methane mechanisms that is used for the modeling.

An interesting result of the CFD simulation is the observation of the cold jets of unburned mixture exiting from the orifices prior to the hot combusting jets. The spark event results in a pressure rise in the prechamber and unsettles the balance of pressure between the two chambers. Consequently, a portion of the prechamber mixture is forced into the main chamber through the orifices and increases the main chamber turbulent intensity. The initial cold jets, although not luminous enough to be seen in the experimental images, have a vital role in the increase of turbulent intensity and in seeding the main chamber mixture with small amounts of easily ignitable near-stoichiometric mixture, facilitating main chamber combustion.

It should be noted that the experimental images of Figure 5-3 to Figure 5-6 are an indication of OH* where only excited OH radicals emit visible light at high temperature which are visible through chemiluminescence imaging. However, the numerical images are an indication of mass fraction of all OH radicals which exist in the computational domain. Another more widely employed technique of measurements for flame studies is Laser Induced Fluorescence (LIF) imaging which has higher spatial and temporal resolution and provides more detailed information of the flame front. A brief comparison between LIF and chemiluminescence images is provided in [129]. Although not all OH radicals get excited during the experiment, comparing the experimental images and numerical mass fraction results is a relatively fair qualitative comparison of OH radical location.

The numerical results also show a backflow of unburned mixture at the later stages of combustion from the main chamber back into the prechamber. The main chamber pressure rise forces the mixture to pass through the orifices and enter the prechamber. This phenomena is also not visible in the experiments.

Figure 5-7 demonstrates the turbulent kinetic energy contours obtained from the numerical simulations. Results show that the turbulent kinetic energy decreases as the N₂ dilution increases. Reduction of turbulent intensity in the main chamber reduces the mixing rate and causes a lower combustion rate. Further decreases in turbulent intensity in the prechamber reduces the chance of spark kernel propagation, and consequently, the initial flame that is develop around the spark diminishes and does not develop into a strong flame leading to low energy jets that penetrate weakly into the main chamber. The last row of images in Figure 5-7 shows the turbulent kinetic energy improvement by adding a small amount of auxiliary air and fuel into the prechamber. It should be noted that injection quantity and timing are both important parameters in ensuring a

successful main chamber combustion event. Lastly, in all cases it can be seen that the turbulent kinetic energy decreases as the combustion rate increases and fades away during the final stages of combustion.

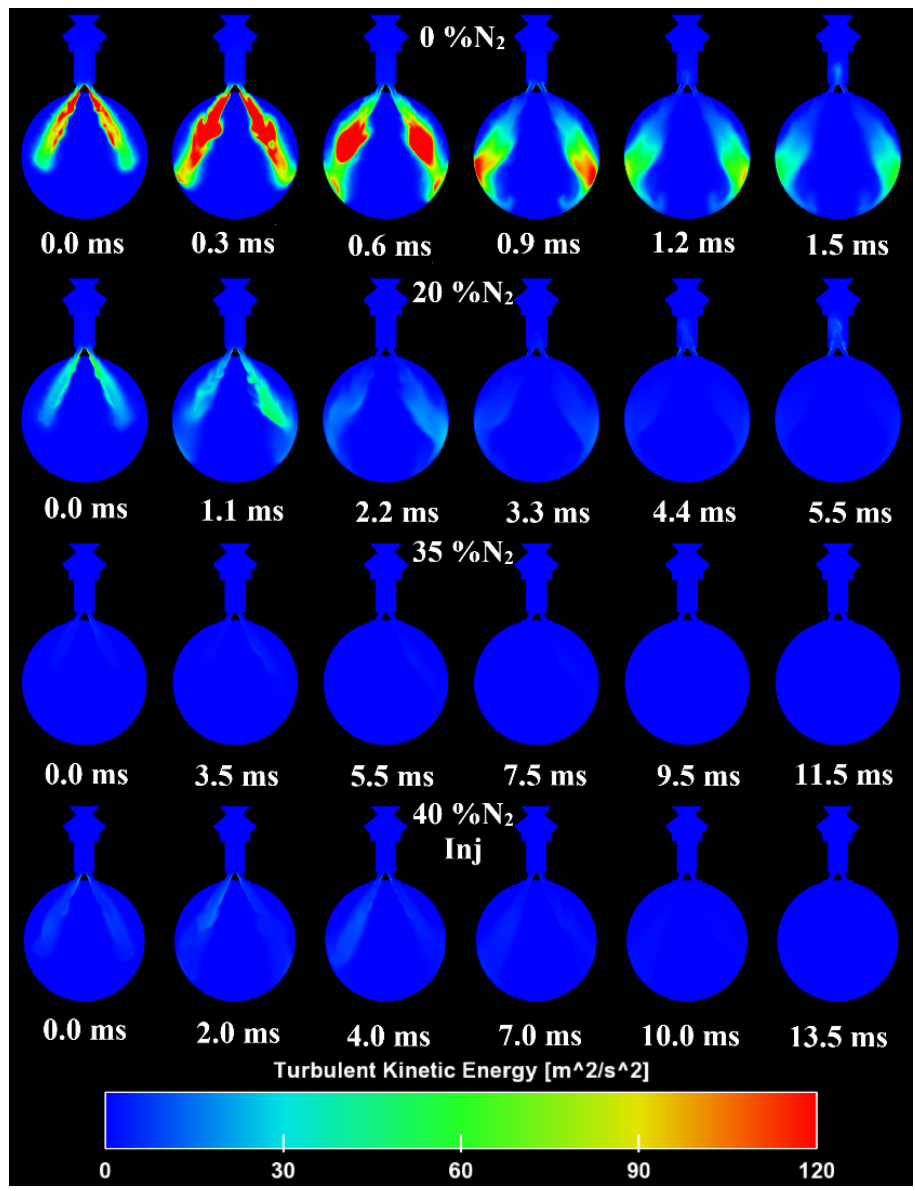


Figure 5-7- Turbulent kinetic energy contours of the simulations for λ =1.0, a comparison between various diluted mixtures.

5-2 Chapter Summary

A set of numerical simulations of the combustion process of an auxiliary fueled TJI system with N_2 dilution was carried out with the Converge commercial CFD code using RANS k- ε turbulence model. The results were compared with optical images captured by a high speed camera during experimental RCM tests. Pressure traces of the numerical simulations are in good agreement with

the experiments. The discrepancies between the numerical and experimental pressure traces are due to a number of reasons. A major contributor is the existence of crevice volumes in the experiments which trap unburned fuel which does not have the opportunity to combust. See Appendix D. A second contributor is the kinetic mechanism and the reduction method. The full mechanism has been shown to lose accuracy at higher pressures and it is expected that by reducing the mechanism further accuracy may have been lost. Lastly, the automated grid refinement settings may also contribute to the variation between the numerical and experimental pressure traces. In addition, the combustion rate in the numerical simulations is slightly different than the experiments. The differences in the reaction rates are thought to be attributable to the use of a reduced mechanism and the fact that the reduced mechanism is not optimal for operation at high pressures. This difference was most pronounced for the case with dilution and auxiliary injection.

The contours of the OH radical mass fractions and the turbulent kinetic energies that are provided in the present study reveal the effect that increased dilution has on decelerating the flame propagation and combustion process. Results also confirmed the idea of combustion enhancement of diluted mixtures by the prechamber auxiliary injection event.

Numerical results also give insight into the combustion process inside the prechamber and provide qualitative data such as the turbulent kinetic energy which is either impossible or difficult to measure during the experiments. In addition, features such as the initial cool prechamber jet as well as the backflow of unburned mixture from the main chamber into the prechamber at the later stages of combustion, which cannot be observed experimentally, are revealed. This phenomenon demonstrates the pressure imbalance through the orifices that leads to the unsteady jet velocity through the orifice and into the main chamber. Jet velocity and its effect on the main chamber

turbulent flow field and consequently flame propagation is of special interest and is discussed further in Chapter 6 and Chapter 7.

Chapter 6 Study of the Physics of a Premixed, Variable Inlet Density and Flow Rate, Confined Turbulent Jet

The behavior of transient, compressible and combusting pre-mixed methane-air jets was experimentally studied with high speed imaging in the MSU rapid compression machine. The jets were generated with the turbulent jet ignition system. The absence of physical analyses of the characteristics of premixed turbulent jets was the motivation for the work presented in this chapter. Experiments were completed for turbulent jet ignition system orifice diameters of 2.0, 2.5 and 3.0 mm each at lean-to-stoichiometric equivalence ratios of ϕ =0.67, 0.8 and 1.0. The hot jet velocity at the orifice exit was calculated using mathematical correlations. The Mach number and Reynolds number were also computed. The high speed imaging shows the influence of orifice diameter on the flame propagation and the shape and structure of vortices resulting from the turbulent jet. Results reveal a direct relationship between orifice exit area reduction and a decrease in hot jet penetration speed. There was also a reduction in hot jet penetration speed with an increase in the equivalence ratio. For the orifice diameters and equivalence ratios tested here, results showed that the jet evolved downstream of the orifice exit in partial agreement with existing correlations. Moreover, the jet was turbulent with calculated Reynolds numbers of around 20,000 or greater.

The purpose of this study is to investigate the behavior of transient compressible gas jets in a TJI system and to perform a structural analysis of the jet using existing correlations from the literature, provided in Chapter 6. As an important component of this investigation, the normalized hot jet penetration length is measured and compared to literature values. The nozzle exit velocity is estimated by using several correlations. The hot jet penetration speed is measured from the processed images captured by a high speed camera during the RCM experiments.

The TJI system used for this work consists of a spark plug located in a small prechamber that is connected to the main chamber via a nozzle having a single orifice. The different-diameter nozzles are easily interchangeable to examine different inlet configurations. The prechamber volume is approximately 5% of the clearance volume of the RCM and the compression ratio of the RCM for these sets of experiments was 8.5. Figure 6-1 is an end-on (bore view) close-up of the Dual-Mode turbulent jet igniter, see Chapter 3.

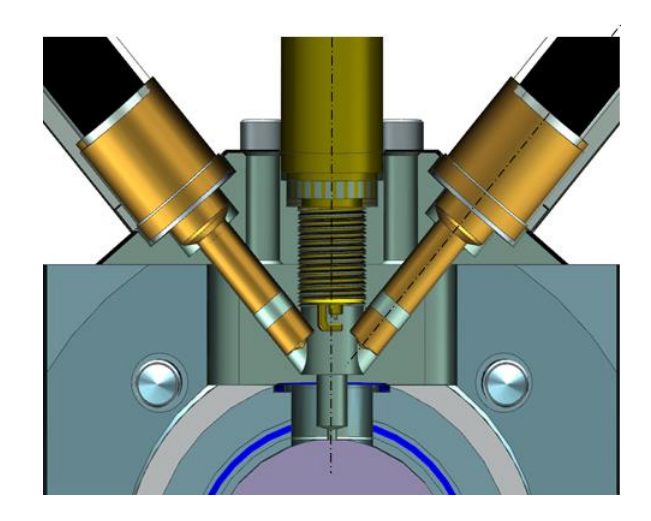


Figure 6-1- Close-up view of TJI with nozzles installed.

Since the flow rate and hot jet Reynolds number depend on the orifice diameter, three single orifice nozzles were tested and their jet characteristics compared. The orifice diameters were 2.0, 2.5 and 3.0 *mm*. The experiments were run at stoichiometric (ϕ =1) and lean conditions (ϕ =0.8 and 0.67).

Combustion visualization of the TJI process was performed with a Photron SA4 High Speed color camera coupled with a Nikon f/2.8 objective lens. The resolution and frame rate were 512×512 pixels and 20,000 frames per second, respectively. The camera lens aperture was completely open for all experimental tests to capture the initial illumination of the turbulent jet. The images were processed with ImageJ software available through the National Institutes of Health [130]. Their

contrast and brightness were enhanced in order to facilitate the measurement of the hot jet penetration length, referred here as the jet tip.

6-1 Theory

In order to understand the TJI process, it is necessary to analyze the hot jet that generates the flame and changes the flow structures in the main chamber, which subsequently influences the burn duration and flame propagation. The hot jet velocity at the nozzle exit is not experimentally measurable with the current set-up. However, using high speed imaging and image enhancement techniques, the jet tip location is measurable as the jet travels toward the lower main chamber wall. The hot jet penetration speed on the centerline is calculated based on the jet travel distance divided by the time interval of travel.

The hot jet velocity at the nozzle exit was estimated from the penetration speed as a function of jet penetration length and by using available mathematical correlations. In the following section, three mathematical correlations [74, 86, 131] are described briefly. Their corresponding estimated nozzle exit velocities are shown in the results section.

6-1-1 Correlation I: Laminar Jet Analysis [131] and Inverse Ratio Correlation

A straightforward laminar jet analysis provides a non-dimensional axial velocity distribution as a function of Reynolds number at the nozzle exit. Further details of the correlation can be found in [131]. The result is

$$\frac{v(x,r)}{v_e} = 0.375 \left(\frac{\rho_e v_e r_e}{\mu}\right) \left(\frac{x}{r_e}\right)^{-1} \left[1 + \frac{\xi^2}{4}\right]^{-2}.$$

Similar to the jet description shown in Figure 2-9, a polar coordinate system is used in which the x-axis aligns with the flow direction. In Eq. 6-1, v(x) is the jet velocity of a flow particle at a

specific point in the main chamber with axial and radial distances (x, r) from the nozzle exit. The quantities ρ_e , v_e and r_e are the jet density, velocity and radius at the nozzle exit, respectively, and the dimensionless quantity ξ is defined as

$$\xi = (\frac{3\rho_e I_e}{16\pi})^{1/2} \frac{1}{\mu} \frac{r}{x},$$
6-2

where J_e is the jet exit momentum defined as follows:

$$J_e = \rho_e v_e^2 \pi r_e^2. ag{6-3}$$

Since r=0 on the centerline, $\xi=0$ and the velocity there reduces to

$$\frac{v_{x0}}{v_e} = 0.375 \left(\frac{\rho_e v_e r_e}{\mu}\right) \left(\frac{x}{r_e}\right)^{-1}.$$

Here v_{x0} is the centerline jet velocity at every stream-wise x location. It is important to note that the preceding laminar jet analysis is based on the hypothesis of a steady non-reacting laminar jet that issues into an infinite reservoir of quiescent fluid (oxidizer) [131]. In TJI, however, the transient turbulent jet issues into a wall-bounded finite chamber. Consequently, the laminar jet analysis is likely not a precise correlation for the hot jet exit velocity. In fact, the exit velocity estimated by the laminar jet correlation is an order of magnitude smaller than the experimentally measured hot jet tip penetration speed. However, the laminar jet analysis suggests a functional form of a correlation in which the nozzle exit velocity is inversely proportional to the hot jet penetration length. It is convenient to apply a descriptive name for this correlation, which is referred to henceforth as the "inverse ratio" correlation,

$$v_{\chi 0} = \frac{c}{\chi}.$$

Here, C is a constant coefficient that can, in principle, be deduced from the experimental data.

6-1-2 Correlation II: Similarity Analysis, [86]

The second correlation that will be used here is based on the steady state solution for the velocity profile within a turbulent gas jet. This correlation uses a similarity analysis of the two dimensional axisymmetric Navier-Stokes equations [86], to find

$$v(x,r) = \min\left[v_e, \frac{3v_e^2 d_{eq}^2}{\left[32\vartheta_t x(1 + \frac{3v_e^2 d_{eq}^2 r^2}{256\vartheta_s^2 r^2})^2\right]}\right].$$
 6-6

As in Eq. 6-6, v_e is the injection velocity at the nozzle exit. Abraham [132] defined a characteristic length called the "effective" or "equivalent" diameter of the gas jet, $d_{eq} = d_{noz} \sqrt{\frac{\rho_e}{\rho_{amb}}}$, in which d_{noz} is the nozzle diameter and ρ_e and ρ_{amb} represent the jet and ambient fluid densities, respectively. Also, ϑ_t is the turbulent viscosity, defined as $\vartheta_t = C_t \pi^{0.5} v_e d_{eq}/2$. Here C_t is a constant coefficient equal to 0.0161 as proposed by Schlichting [133].

Abani and Reitz [86] stated that the velocity decay rate at the centerline is generalized as

$$v_{x0} = \left(\frac{dx}{dt}\right)_0 = \frac{3v_e d_{eq}}{Kx} \quad (x \ge \frac{3d_{eq}}{K} = x_0)$$

Here, K is the entrainment constant, $K=16\pi^{0.5}C_t$. Abani and Reitz [86] calculated the jet penetration length as a function of time, by integrating Eq. 6-7 and assuming a constant injection velocity. The resulting equation is

$$x(t) = \left(\frac{6}{\kappa}\right)^{1/2} (v_e d_{eq})^{1/2} t^{1/2} \quad (for \ x \ge x_0).$$
 6-8

It should be noted that although the hot jet tip penetration speed is a function of 1/x in both Eq. 6-4 and Eq. 6-7, simplifying both of these equations in terms of v_e , redefines them as follows:

$$v_e = \frac{1}{r_e} \left[\frac{v(x).\mu}{0.375\rho_e} \cdot x \right]^{1/2},$$
6-9

$$v_e = \frac{v(x).K}{3d_{eq}}.x$$

where x is measured from the virtual origin of the jet. Eq. 6-9, in the laminar flow analysis, gives $v_e \propto c_1 x^{1/2}$ whereas the turbulent jet similarity analysis gives $v_e \propto (c_2 \times x)$, or, in other words, $v_e \propto (c_3 \times t^{\frac{1}{2}})$. In what follows it will be demonstrated that the predictions of these two correlations may differ by an order of magnitude.

6-1-3 Correlation III: Non-Vaporizing Spray Penetration Correlation, [74]

The third correlation here is the non-vaporizing spray penetration correlation of Naber and Siebers [74]. Their analysis is a modification of the spray penetration analyses of Wakuri et al. [134] and Hays [135] in which an inverse relationship (penetration distance versus time) is introduced. To establish the correlation, the integral control surface technique is used for the injected and ambient fluids with different densities. Major assumptions of the correlation are the uniform functional form of the jet velocity profile in the domain, constant injection velocity, no slip velocity between the fuel and entrained air, and quasi-steady flow with a uniform growth rate (i.e. constant dispersion angle). The dimensionless penetration time, $\tilde{t} = t/t^+$, as a function of dimensionless penetration distance, $\tilde{s} = x/x^+$, is obtained as;

$$\tilde{t} = \frac{\tilde{s}}{2} + \frac{\tilde{s}}{4} \times \sqrt{1 + 16\tilde{s}^2} + \frac{1}{16} \ln[4 \times \tilde{s} + \sqrt{1 + 16\tilde{s}^2}]$$
 6-11

where $t^+ = \frac{d_{eq}\sqrt{\tilde{\rho}}}{a\times\tan(\frac{\theta}{2})v_e}$ and $x^+ = \frac{d_{eq}\sqrt{\tilde{\rho}}}{a\times\tan(\frac{\theta}{2})}$ are the time and length scales used in the nondimensional correlation of Eq. 6-11. The density ratio is defined as $\tilde{\rho} = \frac{\rho_e}{\rho_{amb}}$, where ρ_e and ρ_{amb} are the jet and the ambient gas densities, respectively. The effective jet diameter is defined as $d_{eq} = \sqrt{c_a} \times d_{noz}$ where c_a is the area contraction coefficient. The fuel velocity at the orifice exit is a function of jet pressure, ambient pressure, jet density, and velocity coefficient, (which is the ratio of discharge coefficient, c_d , and contraction coefficient, c_a , ($c_v = \frac{c_d}{c_a}$)). However since the jet pressure

is unknown in the present study, v_e is a variable that must be estimated (in Naber and Siebers [74], the spray's velocity and pressure were both known). The cone angle, θ , of the outer boundary of the jet is termed the dispersion angle since it measures spray dispersion. The constant a accounts for the difference between the real jet dispersion angle and the angle used in the model. Based on the best fit correlation provided by Naber and Siebers [74], a=0.66. More details regarding the derivation of the correlation are available in [74].

In order to apply the penetration correlation in the current study, the penetration length was measured from the orifice exit and the elapsed time was measured from the first appearance of the hot jet. The half dispersion angle is 10 degrees and the area contraction coefficient is 0.8.

6-2 Results

The prechamber size and orifice diameter were examined in several studies [16-18]. It was determined that if the orifice diameter was too small, (d<1mm), the jet was not capable of igniting lean mixtures in the main chamber. In addition, smaller orifices, although having greater hot jet penetration, had higher heat losses [1]. The commonly used orifice diameters for prechamber ignition systems in general, and TJI systems in particular, are in the range of 1-4 mm [1, 136]. In the present study, experiments were performed for orifice diameters of 2.0, 2.5 and 3.0 mm for equivalence ratios of ϕ =0.67, ϕ =0.8 and ϕ =1.0 for a test matrix of 9 possible cases. A nozzle of 1 mm diameter was also examined, however, the exiting hot jet, even with image enhancement, was not sufficiently luminous to measure its penetration length in the region close to the orifice exit. As a result, the exit velocity estimation was not experimentally viable. Murase and Hanada [16] showed that a faster pressure rise is attainable with the smaller orifice diameter (~2.5 mm compared to 4 mm), which greatly enhances the combustion process. In order to produce a substantial

pressure rise in the prechamber, a smaller orifice is used and thus the use of a large orifice (d>3 mm) is avoided here.

Ten runs at each test point were performed to ensure repeatability. The initial pressure in all cases was 1.04 bar which resulted in a compressed pressure of ~ 15 bar and a peak combustion pressure of ~47 bar (with a higher peak pressure for the stoichiometric condition). Figure 6-2 shows an example of the pressure trace and spark trigger signal from an RCM test (note: spark occurs on the falling edge of the square wave signal).

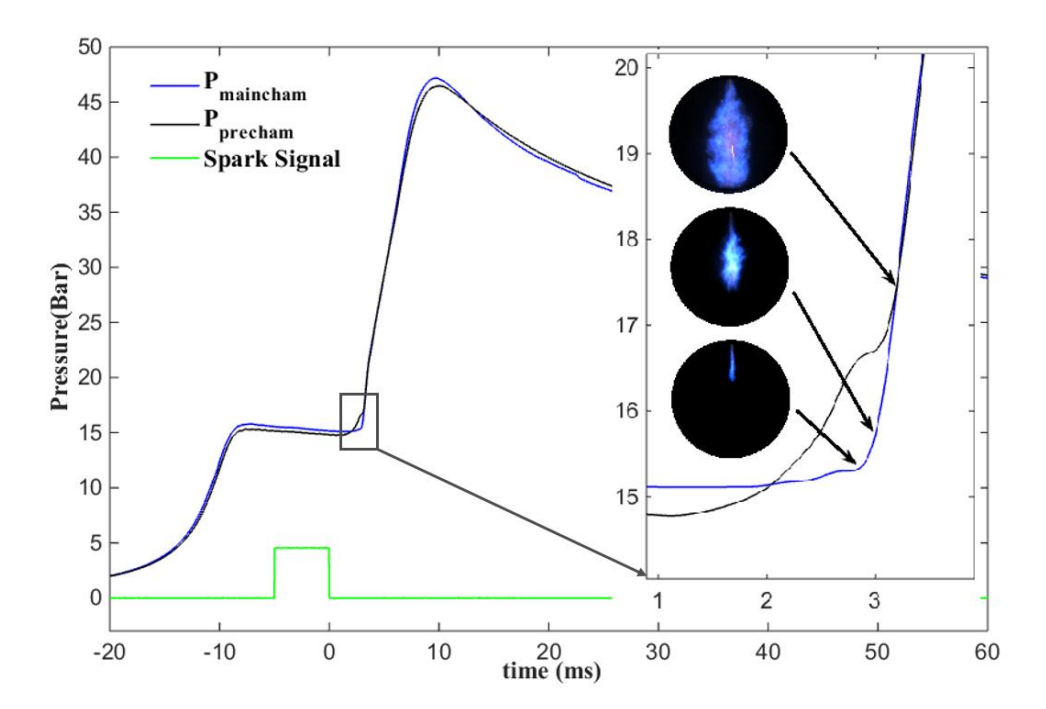


Figure 6-2- Recorded pressure traces in both pre and main chambers together with the spark trigger signal for the 3.0 mm orifice at ϕ =0.8. The inlay shows images of the locations of the jet. The images correspond to the time sequence of Table 7-1. (t=0.1 ms, t=0.25)

An annotated view of the pressure, which correlates to the experimental images of the issuing hot jet appears in Figure 6-2. This plot shows that the hot jet dynamics occur when the pressure in both chambers is close to the TDC pressure (15-20 bar). Numerical studies of the TJI system [23, 128] have shown that a relatively cold jet of unburned prechamber mixture issues into the main chamber

prior to the hot jet of combustion products. This colder non-reacting jet cannot be seen in the chemiluminescence imaging. The cold jet has a strong effect and both increases the turbulent intensity and the mixing rate in the main chamber. Figure 6-2 shows that the initial 15% of the pressure rise is due to the issuance of the hot combusting jet. The influence of the TJI concept on the burn rate compared to direct SI combustion was investigated by Gentz et al. [19]. Detailed images of the issuing jets are provided in the next section.

The temperature at TDC is calculated by assuming polytropic compression. Compressed temperatures at ϕ =1.0, 0.8 and 0.67 as a function of equivalent ratio values are 755, 757and 758 K, respectively. In order to estimate the nozzle exit density and viscosity, the major assumption made here is that the jet consists of the hot products of methane/air combustion, which is a gross simplification of the actual complexity of the real injection process. The jet density and viscosity were calculated using this assumption, which results in a comparable order of inaccuracy in the values of these quantities. The viscosity of the mixture is calculated as the summation of the partial viscosities of all species, $\sum x_i \mu_i$, (x_i =mass fraction of species, i) while μ_i is the viscosity of every species at the adiabatic flame temperature and is calculated using the formula

$$\ln(\mu_i) = A \ln(T) + \frac{B}{T} + \frac{C}{T^2} + D.$$
 6-12

The coefficients *A*, *B*, *C* and *D* are provided by McBride et al. [137]. The jet density is calculated using the ideal gas equation of state at the adiabatic flame temperature.

In order to estimate the uncertainty of the desired/intermediate variables based on the contribution of the uncertainty of each parameter, a sensitivity analysis was performed. The sensitivity analysis has two parts, the uncertainty of the temperature and ambient density at TDC and the uncertainty of each correlation of the exit velocity.

In order to conduct the uncertainty analysis, each variable is considered to be composed of a mean and an error, namely:

$$\alpha = \bar{\alpha} + \delta \alpha. \tag{6-13}$$

Substituting these expressions for the initial temperature, initial pressure, and the compressed pressure in the polytropic compression process equation, and knowing the related errors, $(\frac{\delta T_{BDC}}{T_{BDC}} < 1.5\%)$, $(\frac{\delta P_{BDC}}{P_{BDC}} < 0.7\%)$ and $(\frac{\delta P_{TDC}}{P_{TDC}} < 7\%)$, the compressed temperature error is estimated as 3.5%. Equivalently, using the ideal gas equation of state, the uncertainty of the main chamber mixture density at TDC, $(\frac{\delta \rho_a}{\rho_a})$ is found to be less than 6.5 % for all conditions studied here.

For the second part of the analysis, a considerable error $(\frac{\delta T_{adiabatic}}{T_{adiabatic}} = 10\%)$ is assumed for the jet temperature since the experimental measurement of the jet temperature is unfeasible. This adiabatic flame temperature error leads to ~10% error in the jet density, (varying due to the air/fuel ratio). Substituting for all variables of Eq. 6-7 in the form of Eq. 6-13, the uncertainty calculation of the nozzle exit velocity based on the similarity analysis results in the exit velocity errors, $(\frac{\delta v_e}{\overline{v_e}})$, of 11.4%, 7% and 12.5% for 2 mm, 2.5 mm and 3 mm nozzles, respectively. The uncertainty calculation for the non-vaporizing spray correlation produces estimated exit velocity errors $(\frac{\delta v_e}{\overline{v_e}})$ of less than 4% for all nozzle diameters. Details of the uncertainty analysis are provided in Appendix A.

6-2-1 Jet Penetration Illustration

Experimental images of the penetrating hot jet and combustion initiation in the main chamber are shown in Table 6-1 and Table 6-2. In Table 6-1, variations of the orifice diameter are compared at

 ϕ =0.8, whereas Table 6-2 shows the variation in equivalence ratio for the 2.5 *mm* orifice. To make the early flame development clearly visible for comparison, the image brightness was enhanced.

Table 6-1 shows that the turbulent jet exiting the 3.0 *mm* orifice is the fastest. The span-wise growth of the larger orifice jet is also quicker than the growth of the jets from the smaller orifices. The higher mass flow rate that passes through the 3.0 *mm* orifice enables the development of a more powerful ignition source in the main chamber. By contrast to the 3.0 *mm* orifice, the 2.0 *mm* orifice jet has the slowest speed, probably caused by flow resistance, which restricts the flow and therefore diminishes the flow rate.

In Table 6-2 it can be seen that the stoichiometric jet flame is brighter than the lean jets due to the difference in oxygen concentration. Decreasing the equivalence ratio results in lower soot production. The images in Table 6-2 show that the lean jet is faster than the stoichiometric jet. By the time the stoichiometric jet reaches the center of the main chamber, the leanest jet (ϕ =0.67) has reached the opposite chamber wall. The images show that the jet does not experience selfsimilarity as it impinges on the wall after leaving the orifice exit. The jet tip shape illustrates that the combustion propagation is strong in both the radial and the axial direction at the beginning and that it strongly spreads radially after the jet impinges on the wall. The images exhibit three processes that are made possible by the TJI: distributed combustion; improved flame propagation, and cavity radical dissemination. An additional fundamental feature of the turbulent hot jet that can be seen from Table 6-1 and Table 6-2 is the large scale structure of the turbulent jet, which plays a crucial role in combustion enhancement. Images of Table 6-1 and Table 6-2 illustrate the existence of a laminar flame structure surrounding the reacting core of the flame in the near field region, (x/d < 6). In addition, similar to [138], vorticity generation and destruction is present in the intermediate region (6 < x/d < 25) where density gradients, produced by heat release, are the main

reason for shear layer reduction and potential core expansion. In the intermediate region, a shear layer is formed between the hot jet core and the surrounding mixture: large vortices are located at the edge of this layer.

Table 6-1- Experimental images of hot jet penetration into the main chamber for various orifice diameters (d=2.0, 2.5, 3.0 mm) at a constant equivalence ratio condition (ϕ =0.8).

t (ms)	φ=0.8 d=2.0 mm	φ=0.8 d=2.5 mm	φ=0.8 d=3.0 mm
0.1			
0.15			
0.2			
0.25			
0.3			
0.35			
0.4			
0.45			

Table 6-2- Experimental images of hot jet penetration into the main chamber for various equivalence ratios (ϕ =1.0, 0.8, 0.67) for an orifice diameter of 2.5 mm.

t	$d=2.5 \ mm$	d=2.5 mm	d=2.5 mm
(ms)	ф=1.0	φ=0.8	φ=0.67
0.1			
0.1			
0.2			
0.3			
0.4			
0.5			
0.6			
0.7			
1.2			

6-2-2 Penetration Speed Measurements

Figure 6-3 shows a plot of the changes in the direction x (abscissa) of the hot jet tip penetration speed (ordinate) for the three different orifice diameters with the same equivalence ratio, ϕ =0.8. The hot jet penetration length is normalized by the main chamber diameter, D. The error bars were

calculated based on ten experimental runs completed for each test point. The initial variation is highest due to the variability in the flame kernel formation in the prechamber. The variability reduces as the hot jet propagates towards the far combustion chamber wall. As can also be seen in Table 6-1, the 3.0 mm orifice presents a lower flow restriction, enabling a higher mass flow rate into the main chamber at a higher jet tip penetration speed. In addition, for d=3.0 mm orifice, the rate of penetration speed change stays constant until the jet impinges on the far main chamber wall. By contrast, the 2.5 and 2.0 mm orifice jet velocities have a steeper slope in the region of x/D < 0.3(where D is the main chamber bore) and then remain approximately constant between 0.3 < x/D < 1.0. The steeper slope of the penetration speed decrease for x/D < 0.3 is due to the viscosity effect that induces higher shear forces in the gas close to the orifice exit. This observation is in agreement with a previous turbulent jet diffusion flame study [138]. In this study Pitsch [138] showed that there is a laminar region close to the nozzle exit which results in strong diffusion effects and that molecular diffusion is the main physical process affecting mixing in the vicinity of the orifice exit. As the hot jet reaches the center of the main chamber, its penetration speed increases slightly due to heat released by the flame. Diffusion of heat and mass far downstream of the orifice exit contributes to the constant hot jet penetration speed in the region 0.5 < x/D < 1.0.

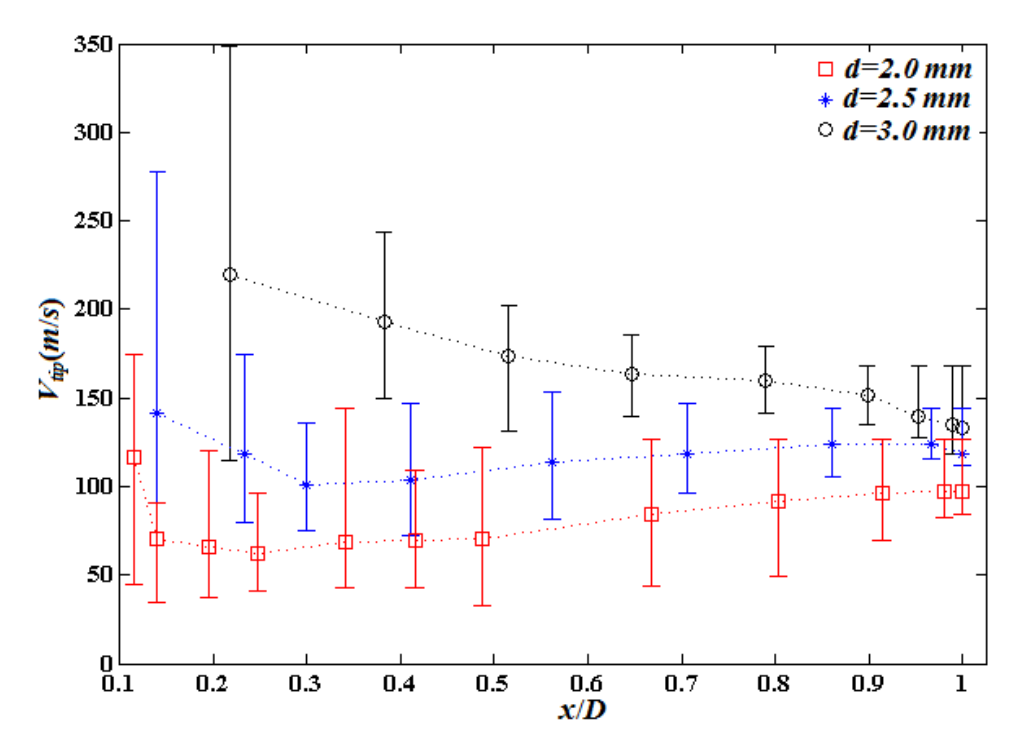


Figure 6-3- Jet tip penetration speed versus normalized jet penetration length at ϕ =0.8.

Figure 6-4 shows the jet penetration speed and its penetration length as functions of time. For consistency, the data for ϕ =0.8 for the three nozzle orifices is shown. Results show that the hot jets of the d=3.0 mm and d=2.5 mm orifices reach the main chamber wall the fastest. In addition, the hot jet penetration speed decreases rapidly with the increase of x/D in the region x/D<0.5. This is the hot jet development region, where the rate of entrainment is low and the radial extension is limited, but the axial propagation of the hot jet is notable. On the other hand, in the region x/D>0.5, defined as the confining region, constant diffusivity effects lead to a constant mixing rate [138], that results in a gradual change in the hot jet tip penetration speeds. In this region, the high temperature reacting jet forces the surrounding mixture to react, which expands the flame surface area. In addition, large scale vortices of the turbulent hot jet that are associated with higher turbulent intensity induce additional entrainment of the main chamber unburnt mixture into the jet. The momentum entrainment rate is lower than the mass entrainment rate, which results in a semi-constant tip penetration speed for the jet in the region 0.5 < x/D < 1.0.

Figure 6-4 demonstrates a very obvious difference between the penetration from the smallest orifice compared to the two wider orifices. As previously discussed, a smaller nozzle cross sectional area applies greater contraction effects on the jet flow, leading to a slower hot jet. The required time to reach the chamber wall for the smaller orifice jet is 1.5 *ms* longer than the two larger orifices.

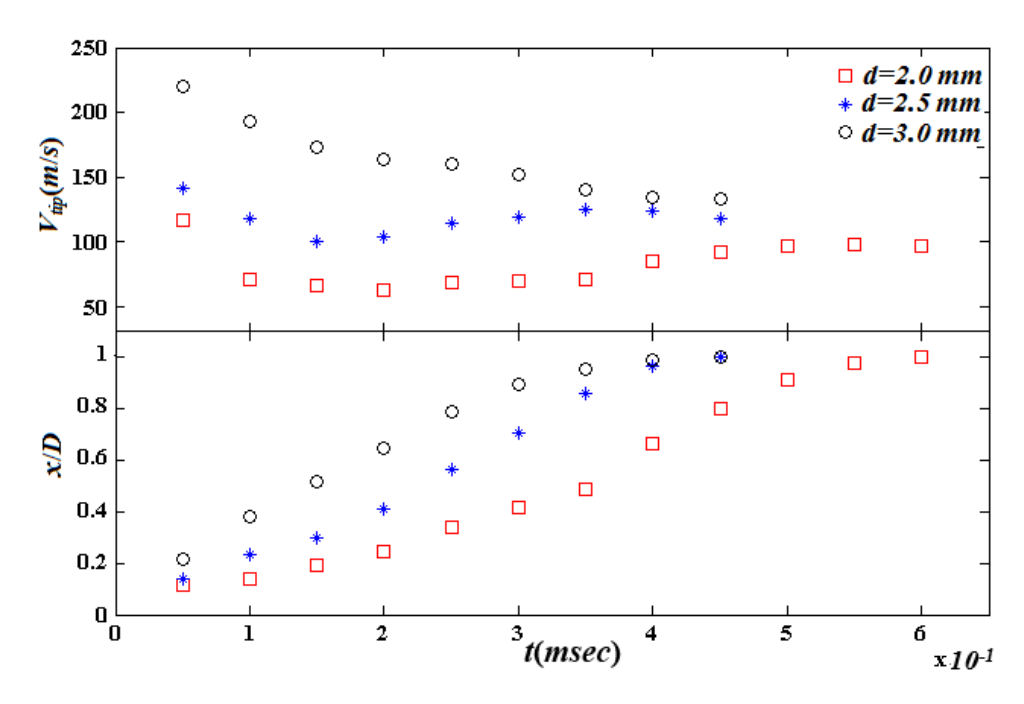


Figure 6-4- Jet tip penetration speed and normalized jet penetration length versus time at ϕ =0.8, here, D is the main chamber bore.

In order to demonstrate the dependence of the hot jet penetration on time mathematically, Eq. 6-11 provides a linear relationship between the jet penetration length and the square root of time for a steady state injection velocity. In a similar manner, Naber and Siebers [74] introduced a short and a long time limit in Eq. 6-11. With the short time limit as \tilde{t} approaches zero near the injector (i. e., \tilde{x} approaches zero), the jet penetration shows a linear dependence on time, $\lim_{\tilde{t}\to 0} |\tilde{s}=\tilde{t}$, and with the long time limit where \tilde{t} approaches infinity, (i. e., \tilde{x} approaches infinity), the penetration length becomes a function of the square root of time, $\lim_{\tilde{t}\to \infty} |\tilde{s}=\tilde{t}^{1/2}$. Naber and Siebers [74] also

defined a transition region where the spray changes from one dominated by the injected fluid to one dominated by entrained air. The results of the present study also show a linear dependency of penetration length on time in the development region $x/D \le 0.5$ and a square root dependence in the region of $0.5 \le x/D$, as the hot jet approaches the chamber wall, see Figure 6-5.

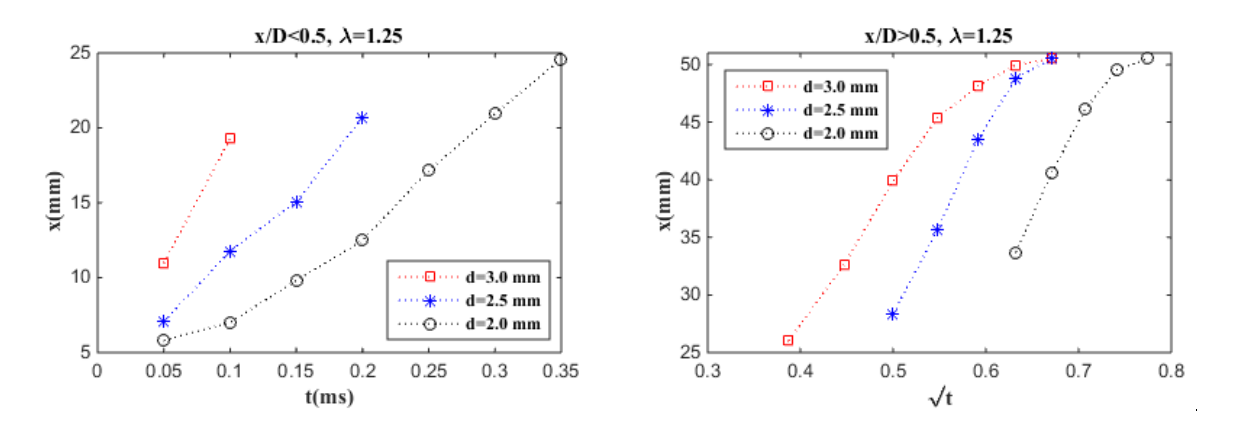


Figure 6-5- Dependence of jet penetration length on time, (a) short ($\tilde{s} = \tilde{t}$), and (b) long ($\tilde{s} = \tilde{t}^{1/2}$), limits, for ϕ =0.8. Note that correlation (a) remains linear throughout but correlation (b) breaks down as time increases and the hot jet approaches the opposite wall.

Figure 6-5 shows that the initial trends of the jets in the present study are in good agreement with the suggested literature correlations [74, 85]. The transition region from linear to square root dependence does not occur at a specific time for all cases; it does, however, occur at the center of the main chamber.

Figure 6-6 depicts the hot jet tip penetration speeds of all mixture conditions (ϕ =1.0, 0.8, 0.67) exiting each of the three orifices. In general, lean hot jets have higher speeds than stoichiometric jets. This observation is explained by differences in jet density. Although the main chamber density increases with the increase in the air/fuel ratio, the differences between main chamber densities at various air/fuel ratio conditions is not notable. However at the orifice exit (not the main chamber), a decrease from ϕ =1.0 to 0.8 results in about 17% increase in the jet density. The additional decrease from ϕ =0.8 to 0.67 results in extra 10% jet density increase. Higher density jets have

higher penetration speeds. The jet density changes across the equivalence ratio conditions are due to changes in the burned gas temperature, while the differences in burned gas pressures are relatively minor.

A distinct characteristic of the larger orifice injector is the more moderate slopes of the penetration speed plots for all equivalence ratios, from the nozzle exit to the far wall. The 2.0 mm orifice is notable for its steep initial penetration speed slope which becomes nearly zero in the region x/D>0.3. Results of the 2.5 mm orifice lie between the 2.0 mm and the 3.0 mm orifice velocities. Figure 6-6 also shows that for the 3.0 mm orifice, there is more variation in the hot jet tip penetration speed for different mixture compositions as the jet travels toward the main chamber end wall. This penetration speed variation decreases with the decrease in orifice diameter. The 2.0 mm orifice shows the least variation in penetration speed with respect to the equivalence ratio.

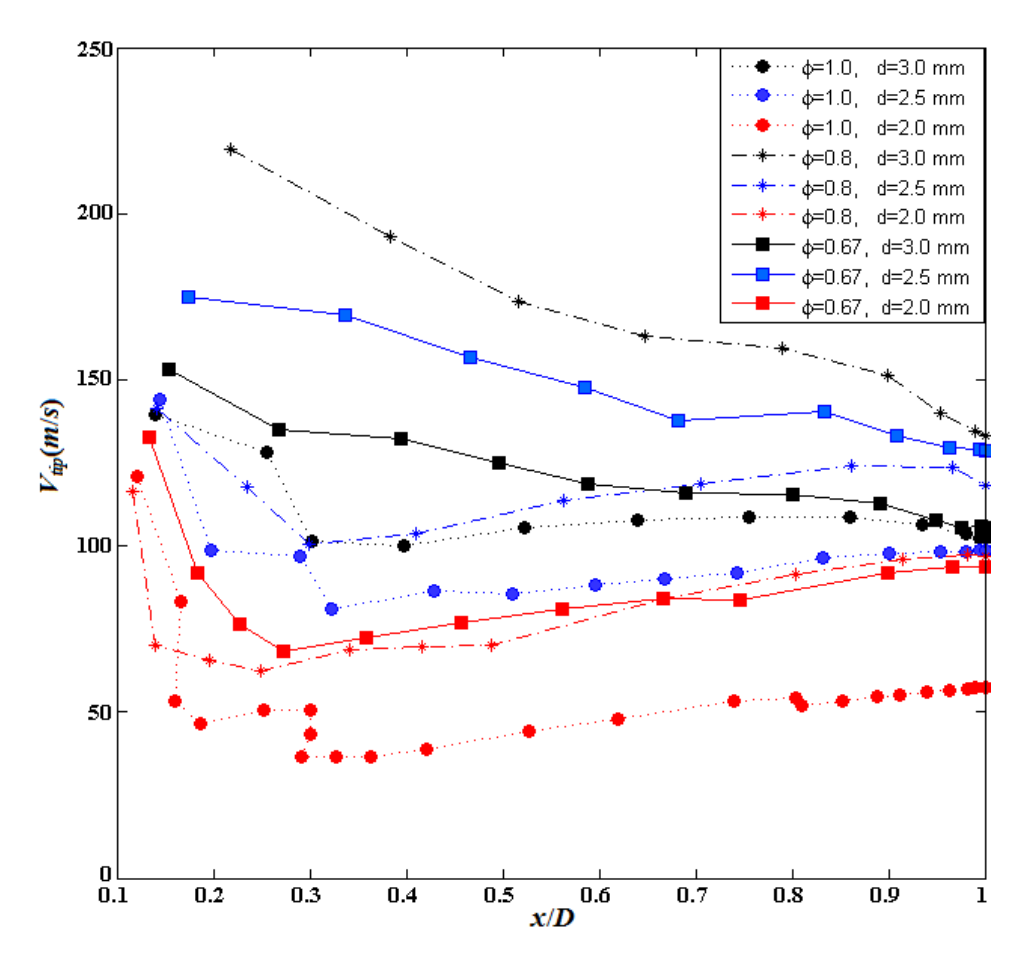


Figure 6-6- Jet tip penetration speed versus normalized jet penetration length for all nine cases. Here, D is the main cylinder bore.

Figure 6-7 shows the experimental penetration speed data in the near and intermediate regions. The turbulent jets studied here satisfy the inequality x/d < 25 (note: d is the orifice diameter). In this range of x/d, the flow is not self-similar according to the jet flow regimes identified by Fellouah et al. [76]. In the region x/d < 25, both the viscosity and momentum of the mixture determine its flow behavior. The structure and size of the vortices depend on the turbulent intensity of the jet and the combustion rate in the main chamber. Two phenomena can be put forth for the combustion rate in the main chamber. Firstly, the amount of turbulence that forms in the main chamber due to the piston motion. Secondly, the turbulent intensity of the initial cold jet of the unburnt mixture, followed by the hot jet of the combustion products of the prechamber mixture that issues into the

main chamber. The turbulent intensity can be influenced by the volume of the prechamber, the piston shape (especially in an engine inlet condition), the size and number of orifices, the spark trigger event, and the amount of released energy, as well as the equivalence ratio. The measurement of the turbulent intensity and all its determining factors is not within the scope of the current study. In addition as stated before in the near field region (i. e., vicinity of the orifice exit), diffusion of heat and mass dictates the structure of the flow field, whereas diffusion effects remain constant in the intermediate field [138]. Here, entrainment determines the speed and shape of the hot jet and also the structure of turbulent vortices.

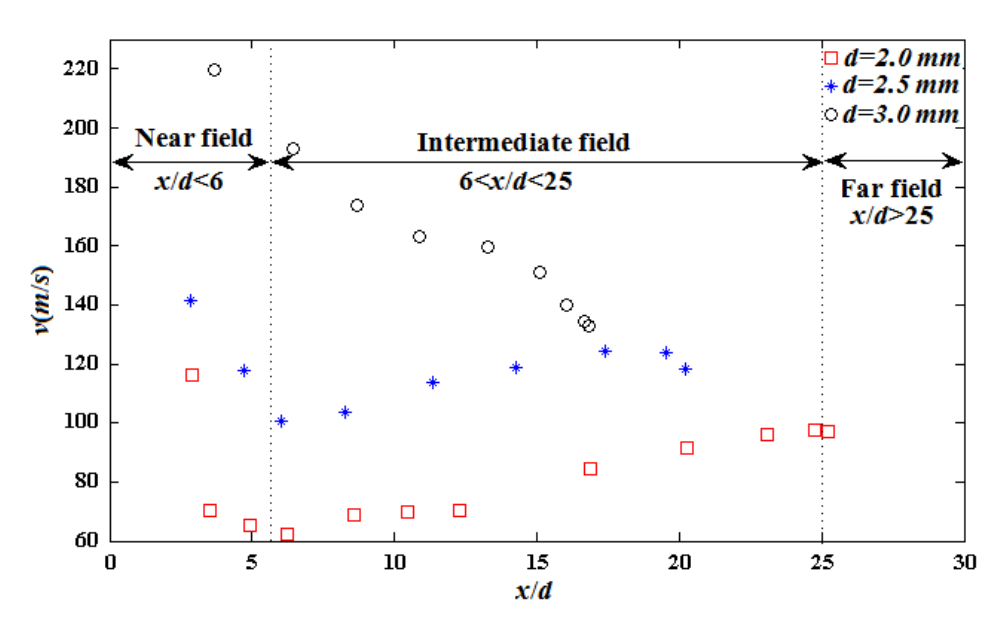


Figure 6-7- Jet tip penetration speed versus x/d (d is the nozzle diameter) for three nozzle diameters at ϕ =0.8

6-2-3 Orifice Exit Velocity Estimation

The measurement of orifice jet exit velocity is not viable in the RCM due to the experimental difficulties corresponding to unsteady combustion in a very small high pressure vessel. Thus, a major goal of the current study was to *estimate* the orifice exit velocity using existing literature correlations. Figure 6-8 illustrates the differences between the inverse, the similarity [86], and the

penetration [74] correlations in the prediction of hot jet velocity at the nozzle exit. Due to viscosity effects and entrainment, the hot jet penetration speed decreases as it travels downstream of the nozzle exit. Consequently, the exit velocity is expected to be higher than the jet tip penetration speeds measured in the experiments. The similarity analysis, however, under predicts the exit velocity. The similarity analysis uses the jet and ambient densities in the calculation of the equivalent diameter, $d_{noz}\sqrt{\frac{\rho_e}{\rho_{amb}}}$, and in the jet exit velocity prediction. A substandard estimate of the jet density is a possible reason for the under prediction of the velocity by the similarity model. The jet may be a combination of combustion products and unburnt gases from the prechamber. Since the composition of the hot jet exiting the orifice was not measured, the presumption of complete combustion in the prechamber and a jet of combustion products that leaves the orifice is a reasonable assumption. It has been observed experimentally, and in numerical simulations [23, 24], that the hot burning gases exit the orifice after an initial jet of cold, unburnt mixture. This initial cold jet changes the main chamber temperature in the vicinity of the orifice exit and also

The inverse ratio correlation predicts a higher velocity at the orifice exit since it borrows the model's constant coefficients from the experimental results. However, the predicted exit velocity for d=3.0 mm seems high. Because of the use of constant coefficients in this correlation, its uncertainty is higher than the two other correlations.

increases the turbulence intensity of the ambient gas, resulting in higher entrainment and radial

spread of the hot jet. This strongly influences the hot jet penetration speed.

The penetration correlation [74] has a discrepancy in the prediction of the d=2.0 mm orifice exit velocity. As shown in Figure 6-8, the predicted exit velocity based on the penetration correlation does not agree with the other correlations and with the first experimental data point (i. e., the

measured penetration speed based on the experimental image in which the initial hot jet is observed). Uncertainties in density ratio, $\frac{\rho_e}{\rho_{amb}}$, area contraction coefficient, c_a , and the dispersion angle are the main reasons for the inaccurate estimation by the penetration correlation.

The Mach number at the nozzle exit is calculated using the exit velocity computed by the inverse ratio analysis. The Mach numbers calculated for all the cases in the present study are less than 0.3. It is possible and useful to calculate the flow Reynolds number as well. The calculated streamwise Reynolds number, Re_x for all experiments lies between 1.4×10^4 and 8×10^4 , where the characteristic length, x, is the distance between the nozzle exit and the hot jet virtual source [73]. For these cases, the jets are turbulent, because x/d is less than 25 and the Reynolds numbers are on the order of 10^4 .

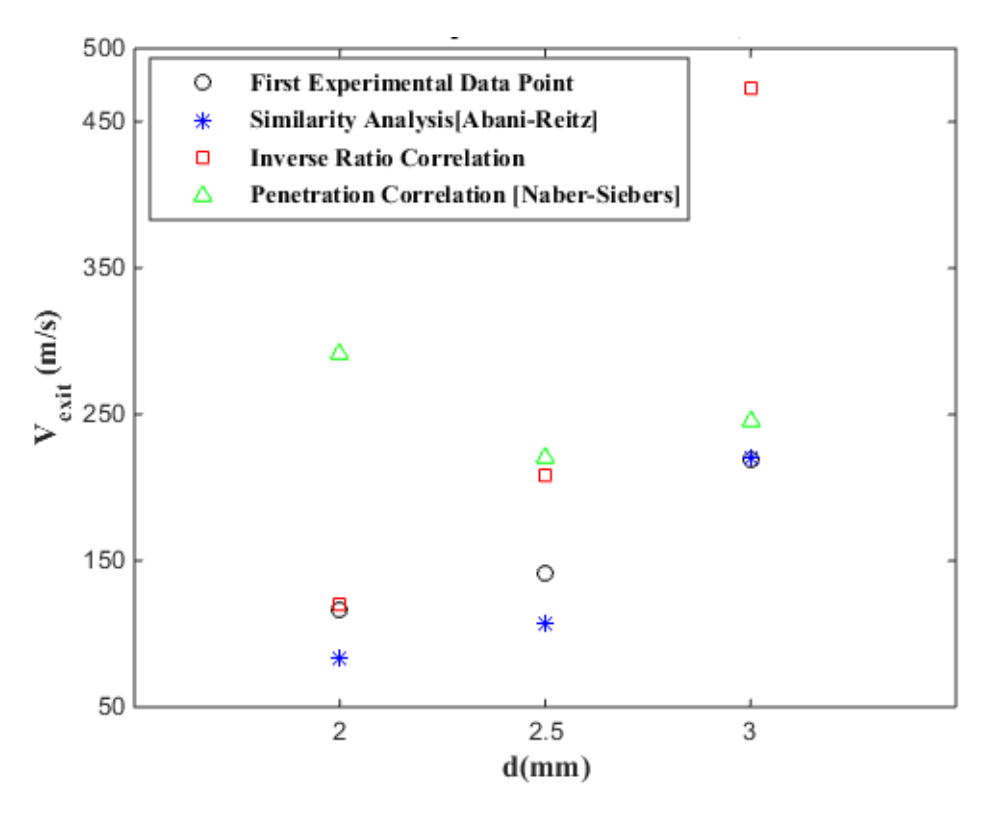


Figure 6-8- Jet exit velocity based on various correlations for three nozzle diameters at ϕ =0.8. None of the three correlations is consistently accurate over the entire range of the data.

6-3 Chapter Summary

A series of tests was carried out to determine the influences of orifice diameter, d, and mixture composition, ϕ , on the jet inlet and tip speed in a turbulent jet ignition system and the rate of flame spread in the main combustion chamber. Experiments performed in a RCM and experimental images of the combustion process have been presented in order to illustrate the progress of hot jet development and combustion initiation in the main chamber as well as the features of the flow structures within the turbulent jet. The results reveal two direct relationships for the orifice sizes and equivalence ratios tested here: (1) reducing the orifice exit area below a threshold produces a decrease in the hot jet penetration speed; (2) a decrease in the mixture equivalence ratio increases the hot jet penetration speed with the exception of the 3.0 mm orifice diameter case. In general, the penetration speed of the burnt gas products exiting the orifice via the jet is higher for leaner mixtures relative to stoichiometric mixtures, which was explained in terms of density increases for the leaner mixtures. The higher density results in faster penetration speed. The changes in the hot jet densities are mainly due to the effect of leaner mixtures on the burned gas temperatures while the pressure differences are relatively minor. Due to the higher exit velocities enabled by the larger orifice diameters, the hot jets that exit the 3.0 and 2.5 mm orifices impinge on the far chamber wall in a shorter period of time. This generates faster lateral spread and higher burn rates in the combustion chamber.

Results show that as the hot jet evolves downstream of the orifice exit, it remains in the near and intermediate field x/d regimes, and does not evolve into the far field stage $x/d \ge 25$. For the range of Reynolds numbers calculated, $\sim 20,000$ and higher, the round jets are all turbulent. Having a turbulent jet in the main chamber increases the mixing rate and also yields a shorter burn duration

and thus lower heat losses during the combustion process. The turbulent jet vorticity also improves combustion by increasing the flame surface area.

Measured results reveal that the factors governing the hot jet characteristics and the main chamber flow field are not similar in the near and the intermediate fields. In addition, there is a distinct transient location, $x/d\approx 10$, where the hot jet penetration speed dependence on time changes from a linear to a square root function. There is also a range of values, $15 \le x/d \le 23$ where the latter correlation breaks down as the jet impinges on the wall. The correlations for the larger nozzle break down earlier likely because the jets are wider and therefore reach the vicinity of the wall sooner than suggested by the centerline x/D value.

Due to the non-viability of velocity measurements during combustion in a high pressure (\sim 50 bar) RCM, existing correlations have been utilized to estimate the orifice exit velocity. Data has been presented for the hot jet velocity at the nozzle exit, predicted by the similarity, inverse ratio and penetration correlations. The under prediction of the similarity analysis compared to the inverse ratio analysis may be due to the assumptions made for the jet density, among other factors that remain to be investigated. Although the inverse ratio analysis predictions are acceptable, they are highly dependent on empirical correlation constants determined from the experimental data, whereas the similarity analysis has no discernable connection to the experiments. The over prediction of the penetration correlation for d=2 mm orifice could be attributed to the uncertainty in the contraction coefficient. However, the uncertainty in the density ratio and dispersion angle are considerable too.

Although the correlations used in the current chapter have not precisely estimated the orifice exit velocity, which is highly variable, they have provided acceptable results to calculate the Reynolds and Mach number of the hot jet, and they show, unequivocally, that the TJI jet and flow is

turbulent. In addition, results show that with the conditions considered and the orifice sizes used the nozzle will most likely not be choked and, hence, no shock or expansion waves are expected.

Finally, the results suggest that as useful as previous literature correlations may be, the fact that the TJI jets impinge on an opposite wall while also demonstrating strong lateral entrainment and spread during injection requires new and improved analyses and correlations. Other major differences between previous studies are the transient injection velocity and the variation in the injection gas density and temperature. None of these variables is accounted for in the previous correlations nor in any of the PPJB studies.

Chapter 7 Theoretical Study of Turbulent Jet Flow Field in a Methane Fueled Turbulent Jet Ignition System

To improve our understanding of the physics and flow chemistry interaction of the reacting jet in the TJI system, more fundamental studies are required. In this chapter, Computational Fluid Dynamics (CFD) modeling of a methane fueled TJI system is used to provide more information of the flow field, particularly the density gradients, turbulence intensity, and temperature fields in both the prechamber and main chamber that are not experimentally measurable in our system. In this thesis, simulation results are compared with high speed chemiluminescence images of combustion in the RCM main chamber. This chapter follows Chapter 6 [139] with emphasis on RCM computational prediction of the orifice exit velocity and detailed comparison with available literature correlations as well as a discussion of a newer, improved correlation model.

7-1 Theory

7-1-1 Generalized TJI Injection Model Derived From First Principles

In Chapter 6, of this thesis, which was published [139], an analysis of the hot jet structure and main chamber characteristics led to an improved understanding of the TJI process. The jet tip location in the main chamber and hot jet penetration speed at the centerline were calculated based on the jet travel distance divided by the time interval of travel. Furthermore, since measuring the jet density and flow velocity were not feasible in our experiments, theoretical correlations were applied to the hot reacting jet penetration speed measurements obtained from the chemiluminescence images. This allowed the jet velocity at the orifice exit to be estimated. A laminar jet [131], a similarity analysis [86] and a non-vaporizing spray penetration correlation [74] were used to approximate the transient orifice exit velocity.

In this thesis, a simplified model based on first principles is introduced to estimate the TJI exit velocity, in which few assumptions are necessary. Since the model is based on the conservation of mass in the control volume of the prechamber, for simplicity it is called the Control Volume (CV) analysis.

Beginning with the equation for conservation of mass written in integral form as follows:

$$\frac{\partial}{\partial t} \iiint \rho dv = - \iint \rho \vec{v} \cdot \hat{n} da, \tag{7-1}$$

we consider that the density in the pre-chamber is uniform with average value ρ_{pre} whereas the density at the exit plane of the nozzle where the pre-chamber gases enter the main chamber has the value ρ_{in} . Equation (1) reduces after minor manipulation to:

$$v_{in} = -\frac{v_{pre} + v_{nozzle}}{\rho_{in}A_{in}} \cdot \frac{\partial \rho_{pre}}{\partial t}.$$
 7-2

Here, V_{pre} is the volume of the pre-chamber, $V_{nozzle} = \pi r^2 h_{nozzle}$ is the volume of the nozzle section that joins the pre-chamber with the main chamber, and $A_{in} = \pi r^2$ is the nozzle section cross sectional area, so that $V_{nozzle} = A_{in}h_{nozzle}$ where h_{nozzle} is the nozzle height. In order to evaluate the main chamber injection velocity from Eq. 7-2 it is necessary to specify the values of $\rho_{in}(t)$ and $\partial \rho_{pre}/\partial t$ separately from the numerical solution. Hence, a monitor point was located in the nozzle orifice exit cross sectional area in order to record the cell averaged values of density. Similarly, a monitor point was located in the prechamber geometry including all the computational cells of the prechamber, to record the prechamber density as a function of time.

7-2 Results

7-2-1 Pressure Traces

Experiments were performed for orifice diameters of 2.0, 2.5 and 3.0 mm and air-fuel ratios 1.0, 1.25 and 1.5. For the CFD simulations, a 3-D grid with a law of the wall constant temperature wall condition was used. The reactive mixture was initially at rest. The first set of simulation characteristics and settings was based on experiments for λ =1.25 and different orifice sizes. The second set of simulations was based on the first set (in terms of spark timing and TDC pressure), with the only quantity undergoing change being the global equivalence ratio.

The initial pressure and temperature for both the experiments and simulations were 1.04 bar and 80°C, respectively. The experimental configuration and geometry, in terms of the sizes of the main and prechamber as well as the CR were to the same as those described in Chapter 6. Figure 7-1 shows a CFD simulated RCM pressure trace for the λ =1.25 mixture compressed to ~15 bar and 757 *K*. Both curves in Figure 7-1 match well during the compression part and the initial stage of

combustion. It is evident that the model can adequately predict the early heat release processes. It does not calculate well the later heat release stage, the burn rate or the peak pressure.

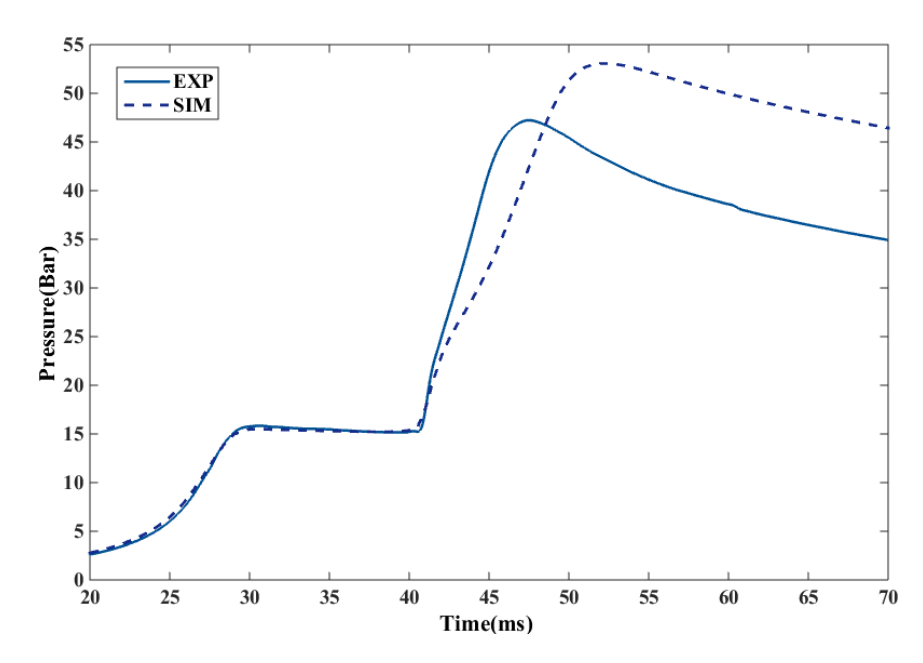


Figure 7-1- A comparison between the simulation and experimental pressure traces for a nozzle diameter=3.0 mm at λ =1.25.

Figure 7-2 shows the influence of variable nozzle diameter on the cylinder pressure for experiments and simulations. A reduced mechanism generates the model results. Since the mixture condition is the same, and only the orifice diameter changes, no substantial change is seen in the pressure traces. As mentioned earlier, the simulation burn rates and peak pressures differ from the experimental results.

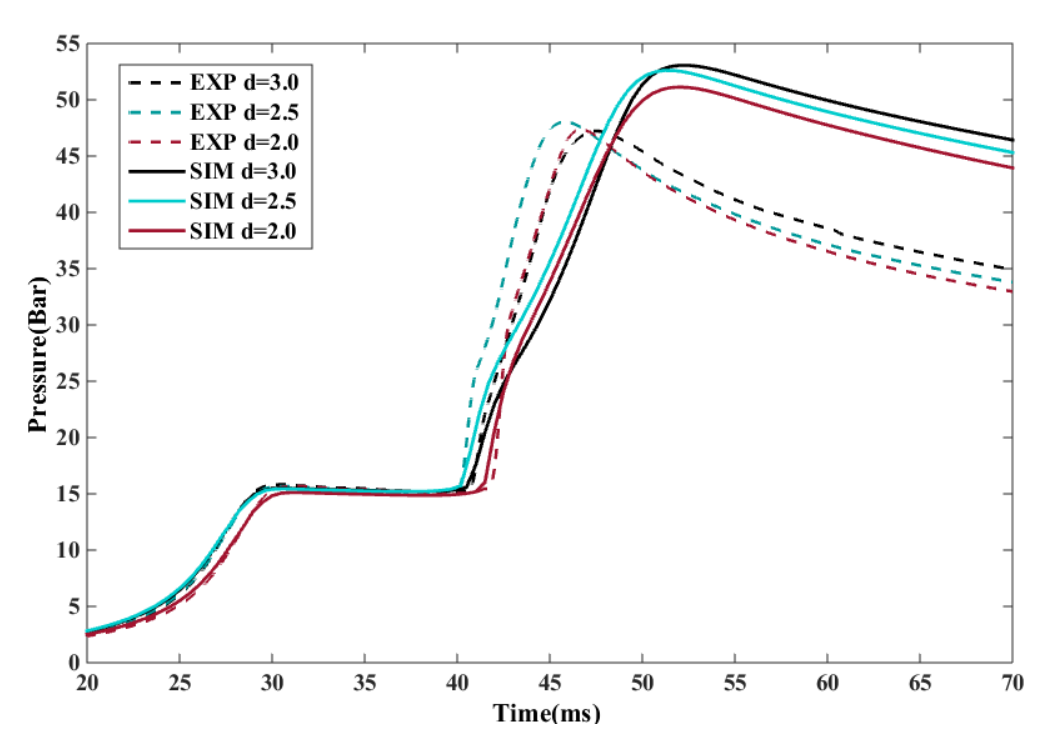


Figure 7-2- A comparison between all simulation and experimental pressure results for λ = 1.25.

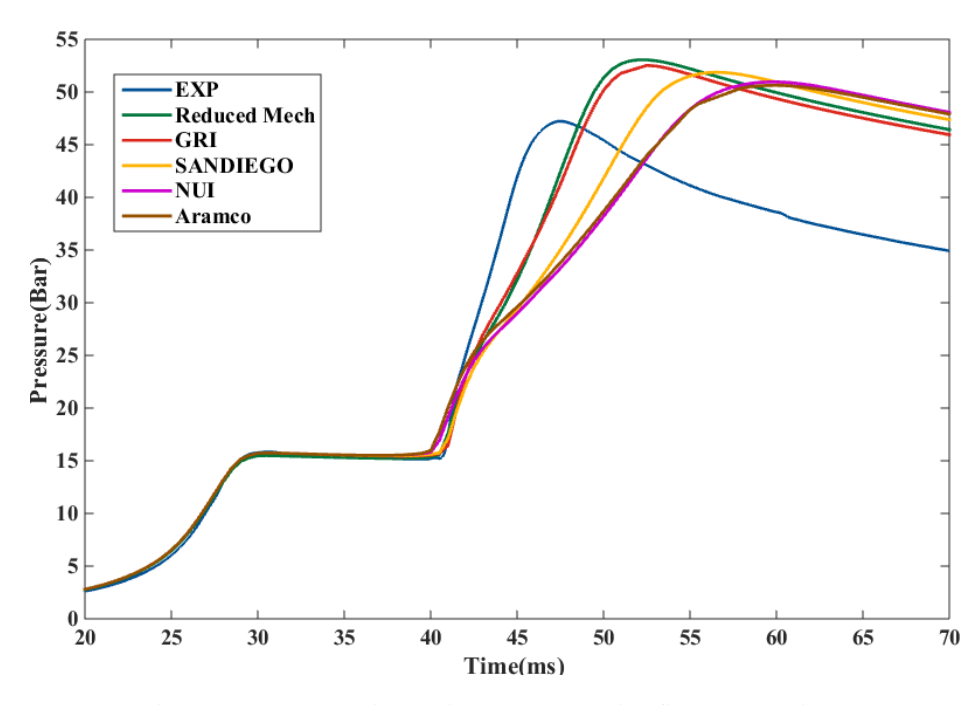


Figure 7-3- A comparison between the simulation pressure with five mechanisms and the experiment. Here the nozzle diameter=3.0 mm and λ = 1.25.

To demonstrate the effects of the chemical kinetic mechanism, modeling results for a lean mixture $(\lambda = 1.25)$ are presented in Figure 7-3 using four full mechanisms and a reduced mechanism along

with the two following modeling constraints: 1) the entire compression process up to TDC is identical for all cases using the initial experimental mixture condition; 2) the spark timing for each case differs due to the differences in ignition delay time predicted by each mechanism. The start of combustion (onset of pressure rise) matches the experiments for all cases.

Figure 7-3 shows that none of the mechanisms precisely predicts the experimental burn rate, with all models yielding higher peak pressures (approximately 10-18%). The differences in the intermediate reactions and active species appear to be the main reason for the differences between the results. Furthermore, the mechanism with the lowest peak pressure error (Aramco) has the longest burn duration (defined as the 0 to 100% pressure rise), while the reduced mechanism and GRI mechanism with the highest error in peak pressure have the shortest burn duration. Interestingly, the GRI mechanism and the reduced mechanism pressure traces match closely and behave similarly for burn duration, maximum combustion pressure and heat release. Considering the computational cost of the full mechanism, the use of a reduced mechanism appears beneficial. Figure 7-4 shows how the pressure trace changes as the initial fuel mass fraction in the domain varies. Figure 7-4 illustrates that the ignition delay time increases as the mixture becomes leaner (the spark timing is the same for all cases). The modeling and experimental trace (λ =1.25) only match during the initial pressure rise and thereafter the simulation underpredicts the burn rate. The stoichiometric simulation result shows a much better correlation with the lean experiment (λ =1.25) and has a slower burn rate than its own $\lambda=1$ experiment (see Figure 7-2). The modeling results show that the burn rate slows down and the peak pressure decreases as the charge becomes leaner. This is expected.

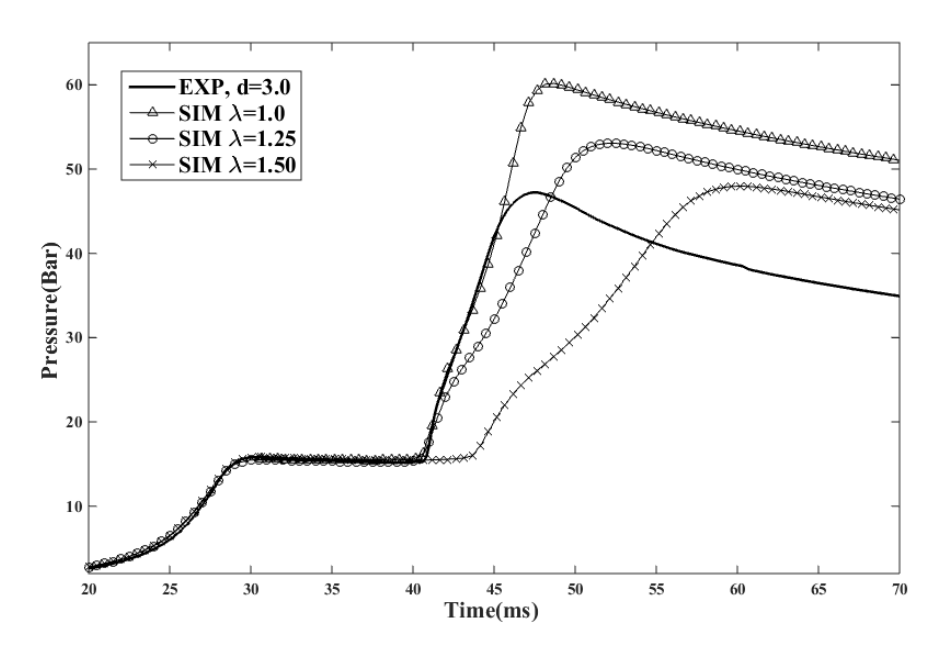


Figure 7-4- A comparison between the simulations at various lambda values (λ =1.0, 1.25 and 1.5) and experimental pressures for λ =1.25 and d=3.0 mm.

7-2-2 Hot Jet and Flow Velocity

In this thesis, the average orifice exit flow velocity as well as the velocity in the main chamber aligned with the jet (see Figure 7-5) are determined numerically. To find the numerically calculated flow variables (e.g. velocity), one monitor point is prescribed in the nozzle throat and seven others in the main chamber aligned with the jet. Monitor points in the main chamber are spheres of 2.0 *mm* diameter. The monitor point in the nozzle throat has a diameter equal to that of the nozzle. The reported flow variables are averages of the computational cell data enclosed in that sphere.

A time-series of the flow velocity distribution at the monitor points during the jet impinging period for the 2.5 *mm* orifice is illustrated in Figure 7-5 and a comparison between the different orifice configurations is illustrated in Figure 7-6. In these figures, the horizontal axis is the simulation time, which is limited to the period were the jet enters the main chamber and the velocity in the domain has the highest magnitude. The velocity magnitude is negative as it is directed in the negative *y* or vertical direction, where the y-axis is aligned with the nozzle axis with the positive

direction is toward the prechamber. (a negative sign indicates flow from prechamber to main chamber). Seven curves are shown in Figure 7-6 with each sub plot of nozzle diameter, corresponding to the velocity at each monitor point, based on the distance from the orifice exit (i.e. 1 is closest and 7 is furthest). Furthermore, the average velocity at the throat is shown here. For the case shown in Figure 7-6, the spark is at 39 ms and the first jet is visible at 42.69 ms when d=3 mm. The velocity profile shows that the maximum velocity in the domain occurs at 43 ms in the throat and elsewhere indicating that the initial hot visible jet does not have maximum velocity and that at each point 1-7 the flow becomes faster as a greater volume of the air-fuel mixture burns in the prechamber. Of course, the flow subsequently slows down for t>43 ms.

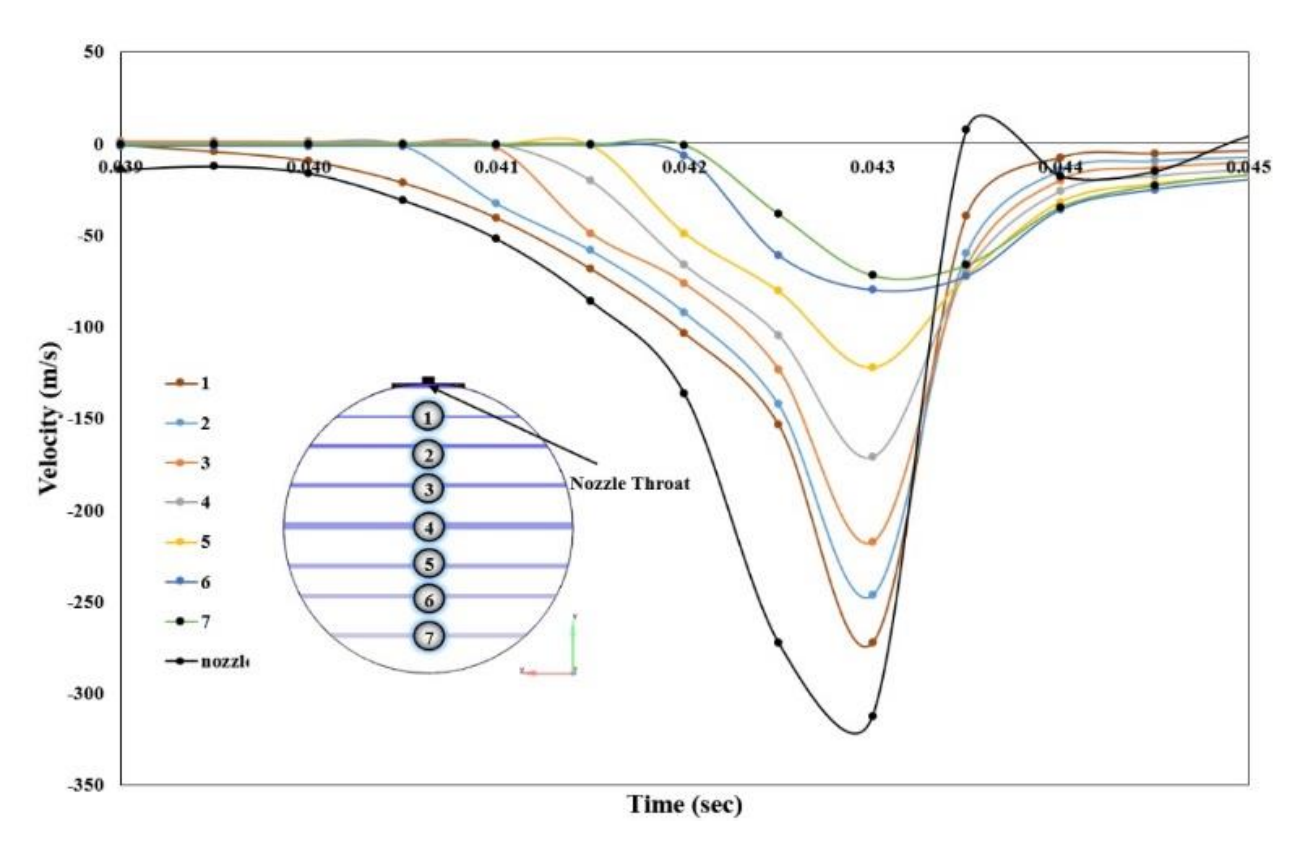


Figure 7-5- RANS simulation of time-dependent velocity profile at each monitor point over the span of the jet impingement period, d=2.5 mm, $\lambda=1.25$.

The comparison between various orifice diameters in Figure 7-6 indicates that the flow through the smaller orifice has the highest velocity near the vicinity of the orifice exit (i.e. in the main chamber), however, the peak velocity magnitude, closer to the end wall, is lower than for the two larger orifices. In fact, the flow velocity magnitude in the lower section of the main chamber (from the center to the chamber wall) decreases as the orifice diameter decreases. Comparing these results with the flame speed results reported in [139], a distinction should be made between the hot jet speed and the flow speed measured through simulations. In fact, the velocity magnitude of the flow which is the velocity of unburned mixture and could not be visualized in the experiment is higher than the reacting jet velocity. To distinguish the hot reacting jet velocity and compare the numerical results, with the experiments in [139], line of sight measurements were performed, as described in section 7-2-3.

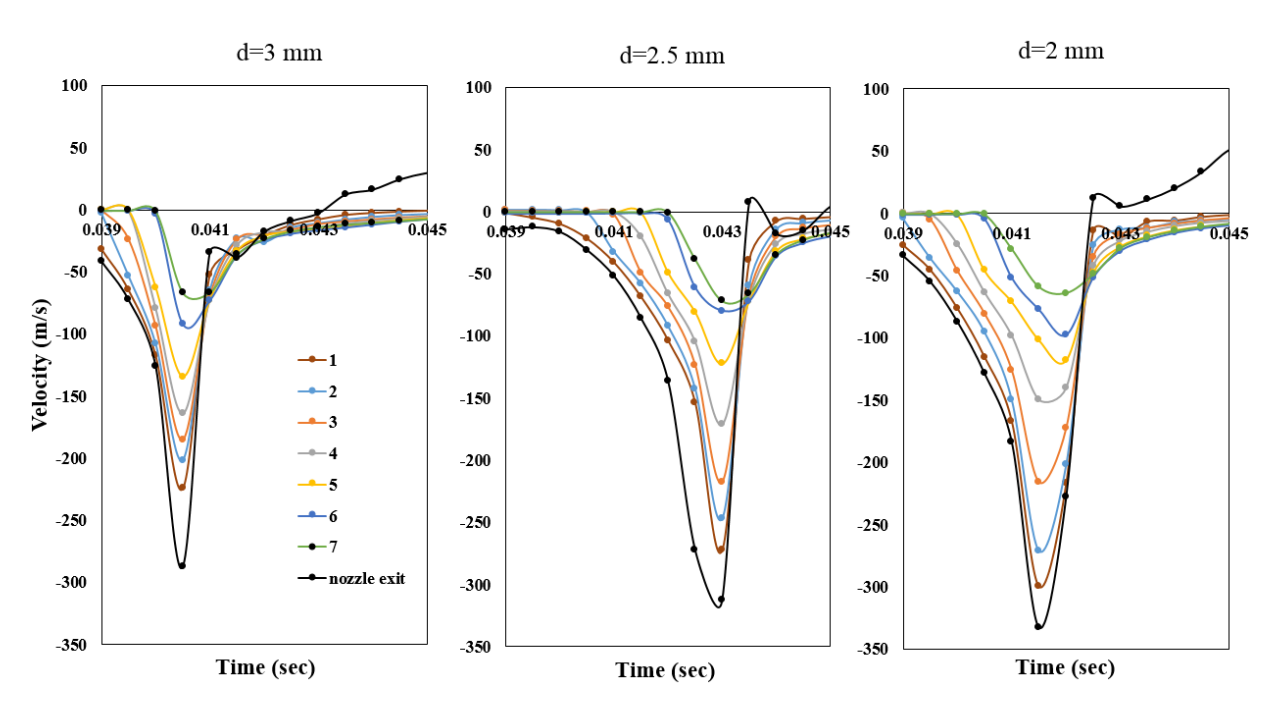


Figure 7-6- Time-dependent velocity profile at monitor points over the span of the jet impingement period, for all nozzle configurations, $\lambda=1.25$.

The orifice exit velocity at the nozzle throat was calculated by taking the average cell data enclosed in a sphere monitor point with diameter d, where d is the nozzle diameter, and located at the orifice exit cross section. The location of this monitor point is shown in Figure 7-7.

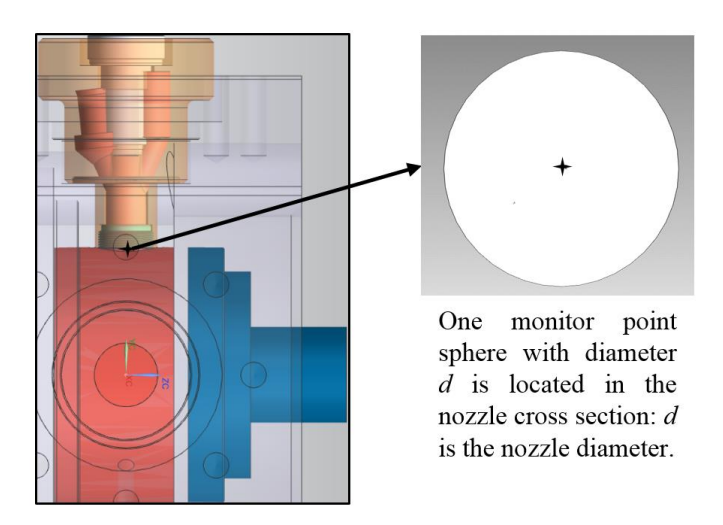


Figure 7-7- Schematic of the spherical monitor point in the domain.

A time series of the y-direction velocity at the orifice exit and the mass flow rate are shown in Figure 7-8. The simulation results show that the maximum velocity decreases as the nozzle exit area increases. The maximum velocities are $353 \, m/s$, $313 \, m/s$ and $287 \, m/s$ for $d=2.0 \, mm$, $2.5 \, mm$ and $3.0 \, mm$, respectively. It should be mentioned that the spark timing is not unique for all cases where the simulations were matched with their corresponding experiments. The recorded time differences between the spark event and the onset of the jet discharge are 3.44, 3.69 and 3.9 milliseconds for 3, 2.5 and 2 mm orifices, respectively. The difference between mass flow rates in various nozzle configurations supports the idea that with a larger orifice cross sectional area, a lower flow restriction is applied, enabling a higher mass flow rate into the main chamber as discussed in [139]. The smaller orifice has a lower mass flow rate despite its higher velocity.

The onset of the hot jet discharge is shown with red diamonds. Figure 7-8 shows that the onset does not coincide with the peak flow velocity, meaning that the flow velocity accelerates as a

larger volume of mixture reacts, leading to an increased pressure buildup in the prechamber. Comparison of the location of the onset of the hot jet discharge in the velocity and mass flow rate plots shows that when the velocity in the throat is highest the highest mass flow rate is not necessarily the highest because the rate of change of density is not uniform. The positive velocities in Figure 7-8 indicate that there is a flow from the main chamber into the prechamber during the pre-combustion and the post hot jet discharge stages.

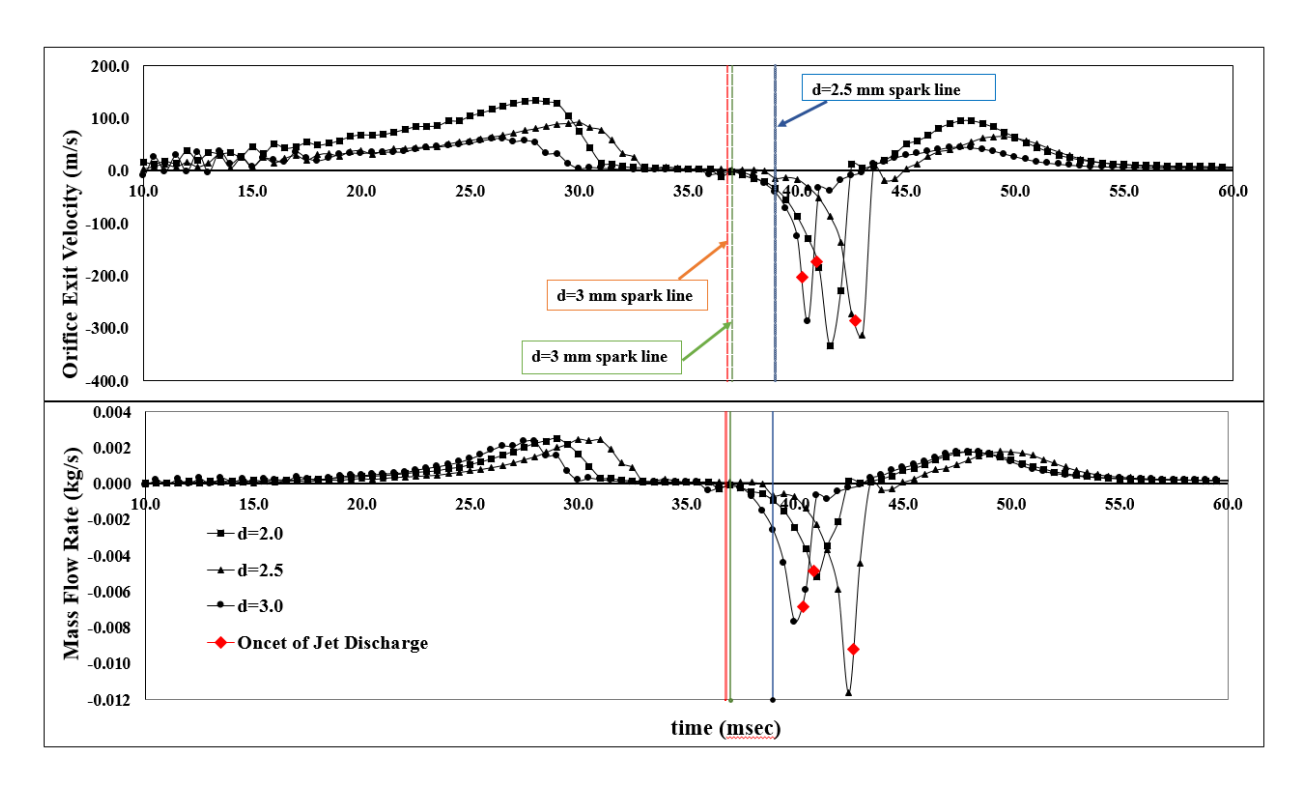


Figure 7-8- Velocity and mass flow rate variation at the nozzle throat for orifice diameters of d=2.0, 2.5 and 3.0, λ = 1.25.

7-2-3 Line-of-Sight Penetration Measurements

In [139], the line-of-sight penetration speed of the reacting jet was measured from images recorded during combustion experiments. In this thesis, the numerical temperature contours are used to measure the line-of-sight penetration jet speed. Results shown in Figure 7-9 are compared with Figure 6 from [139]. Although the initial penetration speed from the simulation is not equal to the

experiment, the overall predictions are qualitatively similar. In both methods, the jets from the larger orifices reach the chamber wall faster than those from the smallest orifice jet. Furthermore, the smallest orifice jet has the lowest penetration speed except initially. To clarify the difference between the modeling and experimental results, the numerical line of sight velocity is normalized by its corresponding experimental values and is shown in the top right corner of Figure 7-9. Results show that the initial speed estimated by the modeling matches with the experimental measurements for the large orifice while for the smaller orifices it is higher at the vicinity of the orifice exit and merges to the experimental measurements as the jets reach the chamber wall. This could be explained by inaccuracies of the turbulence model and chemical mechanisms used for the simulation, by errors in the experimental measurements, and by erroneous extrapolation of the experimental data using modeling approximations [139]. The inaccuracies of turbulence models are well known and extensively documented [88]. In addition, it is found that the RANS models do not provide accurate results where the flow is highly turbulent (for example, in the vicinity of the orifice exit) and all the turbulent length scales must be resolved. Near the chamber wall, however, the turbulent intensity is low and time averaged velocity values are reasonable. Results suggest the adaptation of LES models in the orifice exit region in order to increase the accuracy of the numerical simulations.

Concerning chemistry, none of the chemical mechanisms used accurately predicted the ignition delay time, the maximum pressure and the burn rates in the RCM experiments. Hence, predicting the details of the expulsion process with fidelity is not likely.

Finally, in order to compare an experimental measurement of exit velocity with the numerical simulations, an extrapolation from the measurement point downstream of the exit was used: this extrapolation is fraught with error, as described in [139].

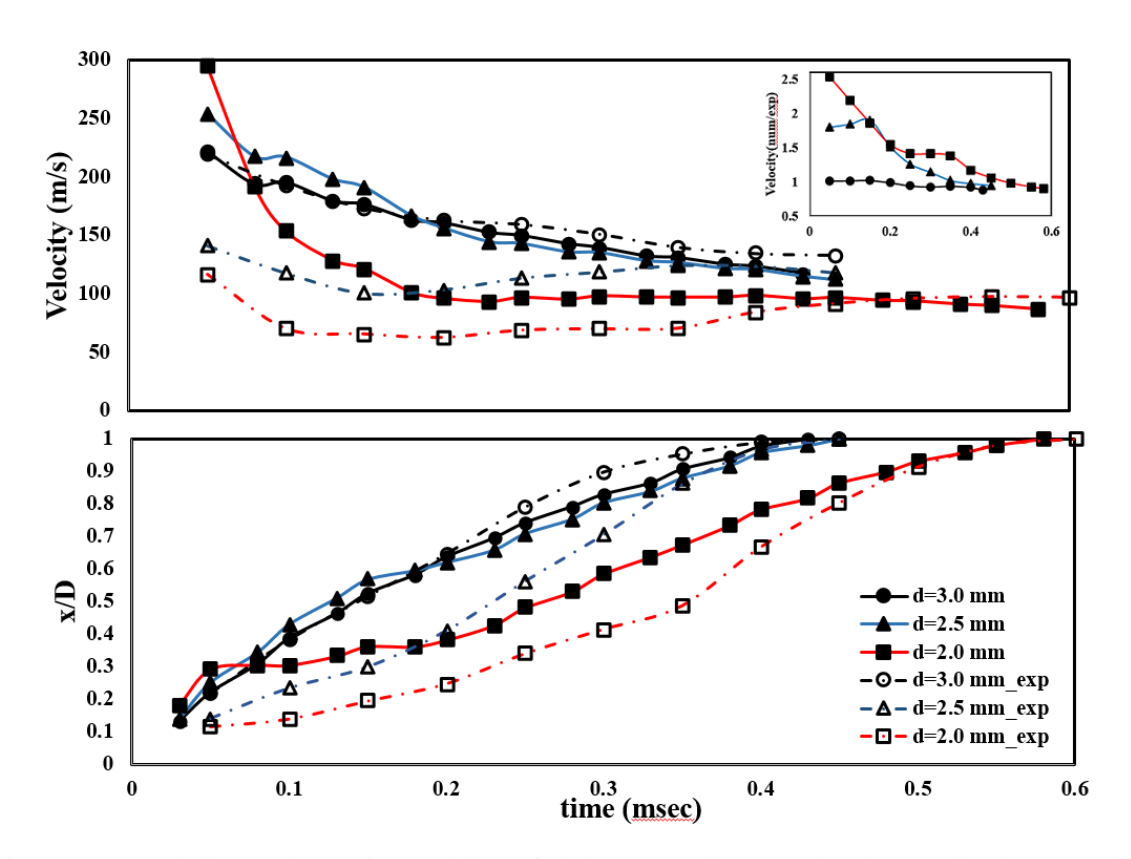


Figure 7-9- Modeling and experimental line-of-sight penetration speed and normalized penetration location of the reacting jet versus time.

In order to form a quantitative interpretation of the overall ignition and combustion, a burn duration analysis is proposed. However, this analysis did not enable the timing of the actual physics to be precisely resolved [140]. As a result, the analysis of inflection points and change of curvature of the RCM pressure curves becomes relevant. Gentz et al. [140] performed a thorough analysis of the inflection points and curvature changes which required evaluating the first, second and third derivatives of pressure. Physical events such as the end of compression, the end of combustion and fast changes in the pressure curve (an indicator of jet ignition and autoignition) were achieved. The start of jet ignition (from spark discharge to jet penetration in the main chamber) and the time interval of specific combustion events such as jet ignition (characterized by wall impingement and flame propagation) and autoignition (for the special case of isooctane-charged experiments) were clearly identified. In this thesis, the higher jet velocity seen in the modeling results (Figure 7-9)

corresponds to the rapid pressure rise (beginning of jet ignition-first stage), as shown in Figure 7-1 to Figure 7-4. The quick decay of velocity is related to the slower pressure rise (second stage of combustion) that occurs during the jet ignition interval (or the plume [59]). As expected, a similar trend were seen in the experimental traces.

7-2-4 Orifice Exit Velocity Estimation

One of the major goals of Chapter 6 was to estimate the jet exit velocity using correlations from the literature [139]. The process of a jet exiting the orifice is highly transient, hence it is more reasonable to describe the velocity profile over the span of jet discharge. Here, a simple, practical correlation is introduced (i.e. Control Volume analysis) and the exit velocity results along with the numerically calculated exit velocities are compared. As stated previously, viscosity effects and entrainment in the main chamber produce a decrease in the hot jet velocity, hence the exit velocity is expected to be higher in the nozzle throat compared with the main chamber. The estimated modeling results show that the hot jet exiting the 2.0 *mm* jet is the fastest. Modeling results follow the Control Volume correlation shown in Figure 7-11.

The jet exiting the nozzle is a mixture of burned and unburned mixture. However, only the reacting jet is visible through the experimental combustion visualization. Nevertheless, the unburned mixture velocity contributes to the average velocity of the flow exiting the orifice. Overall, the estimated hot jet exit velocity is in the range of $100-300 \, m/s$ giving a Reynolds number of 2.8×10^4 to 6×10^4 which is in the range of turbulent flows [75, 78]. In order to acquire a better understanding, the simulation time and the jet velocity are both normalized based on the interval of the jet discharge and maximum exit velocity, respectively. The time interval was normalized with the time interval t_{final} - $t_{initial}$ where t_{final} is the time at which backflow begins and $t_{initial}$ is the time at which the jet fist exits the pre-chamber nozzle into the main chamber. The time normalized

in this way varies between zero and unity. The jet velocity is normalized with the maximum exit velocity so that $\bar{v}_{max} = 1$. The normalized velocity results are compared in Figure 7-1. It is noted that the normalized functional agreement is good even though the exact numbers are not in agreement. The reasons for this are presently unclear.

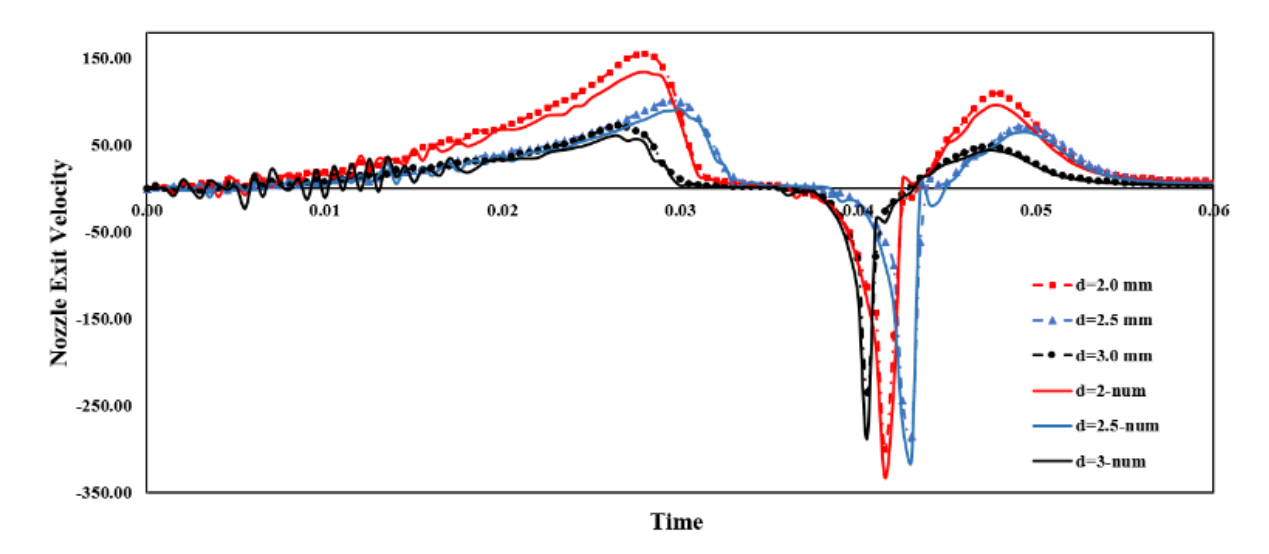


Figure 7-10- Jet exit velocity based on Control Volume correlation compared to the modeling results for three nozzle diameters at λ =1.25.

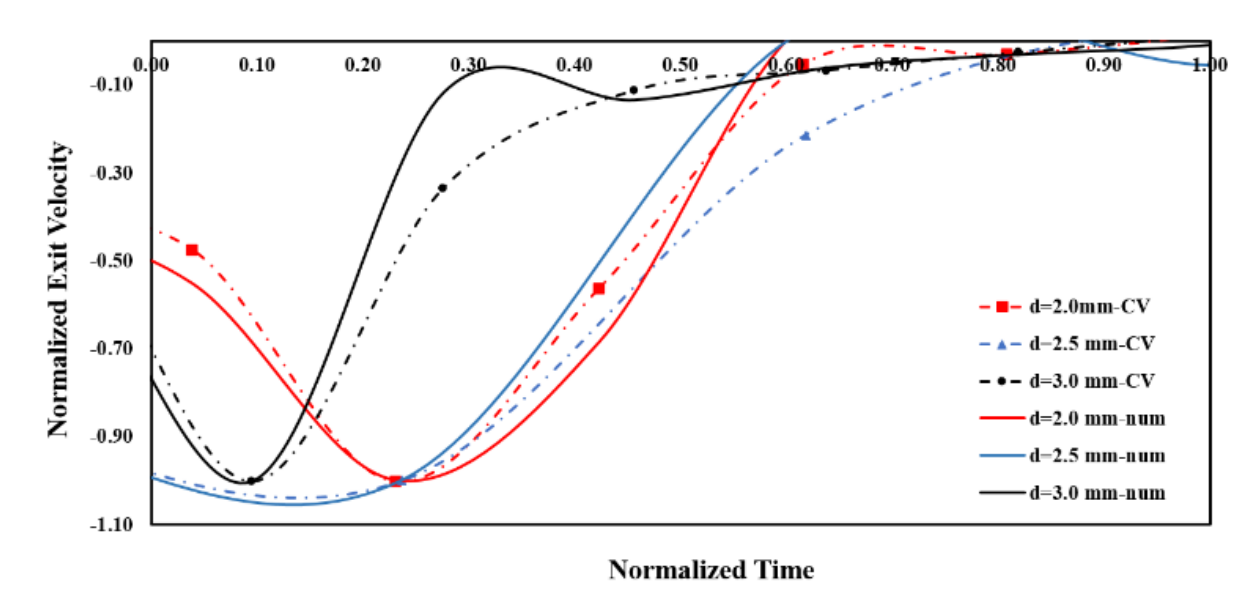


Figure 7-11- Normalized exit velocity versus normalized time. A comparison between Control Volume analysis and modeling which shows that the normalized experiment and simulation trends are similar.

7-2-5 Pressure Normalization

Since the combustion burn rate predicted by the numerical model is slower than the experiments, comparison of modeling contours with experimental images at similar times in accordance with the start of combustion is misleading. A more appropriate method is to make the comparison at the same burn duration (BD= time between the start of combustion and start of heat release). The onset of combustion is defined as the maximum rate of pressure rise following compression. The peak pressure is defined at the point of the maximum rate of pressure drop at the end stage of combustion. These two points are calculated by locating the maximum of the second derivative of the pressure data $(\frac{d^2P}{dt^2}]_{max}$), and the location where the first derivative of the pressure data equals to zero $(\frac{dP}{dt}]_0$), respectively. For clarity, annotations detailing these points are presented in Figure 7-12.

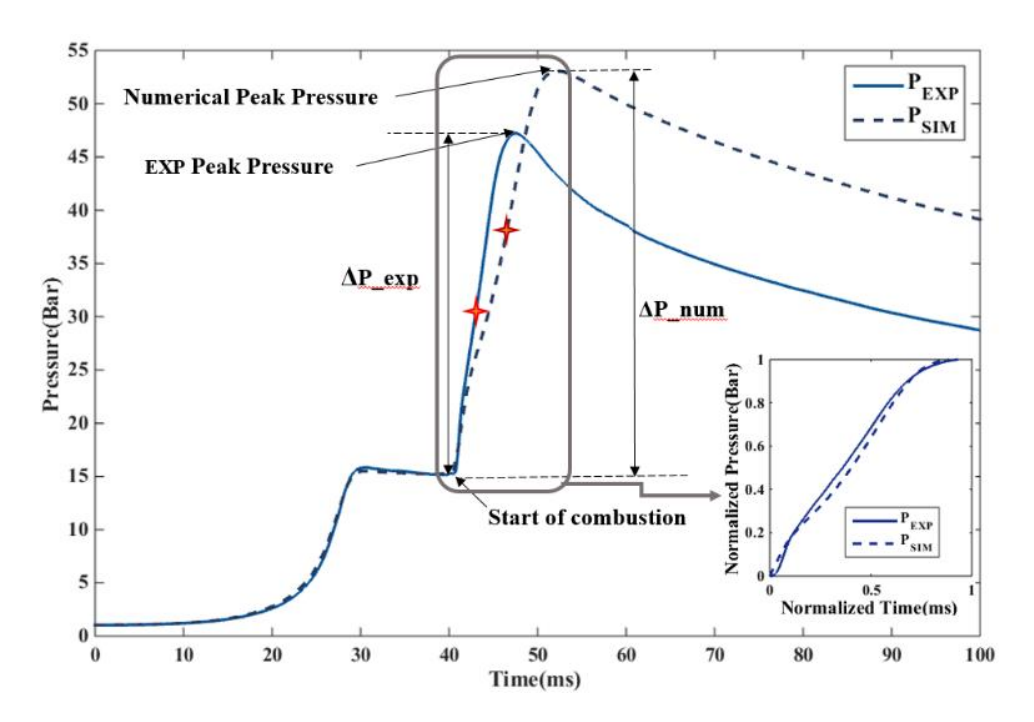


Figure 7-12- Location of the start of combustion and peak pressure for experimental and numerical pressure traces.

Since the simulation compression stroke matches the experiment, and no ignition or injection events occur during compression, only the combustion portion is normalized. The pressure curves are scaled such that 0 corresponds to the pressure at the start of combustion (0% of combustion) and 1 corresponds to the maximum pressure achieved (100% combustion). The normalized pressure trace for the lean case (λ =1.25), and nozzle diameter of 3.0 *mm* is shown together with the experimental trace in the right bottom corner of Figure 7-12.

Comparisons between temperature contours from the modeling and the experimental images are shown in Figure 7-13 to Figure 7-15. From the temperature field evolution during combustion, it is noted that the bigger orifice reacting jet proceeds faster in the initial stage of combustion. However, it slows down as the jet reaches the center of the reaction chamber. Although the modeling burn rate does not completely match the experiment, the trend of flame development is reproduced by the RANS approach using the normalized combustion time. Furthermore, the simulation contour plots show that flame propagation in the prechamber is not symmetric because of the spark plug orientation. Flame development in the prechamber leads to a pressure increase and a disruption of the pressure balance between the two chambers. Pressure imbalances force the unburned prechamber gases to enter the main chamber creating a cold jet of unburned mixture. The cold jet exerts a large influence on turbulent mixing in the main chamber.

In addition, the large-scale vortices of the turbulent flow at the margin of the flame kernel grow rapidly after the jet hits the chamber wall, increasing the mixing rate and combustion rate. Needless to say, not all the vortices of the turbulent flow are captured by the modeling since the RANS model uses ensemble averaging of the flow field terms and is not capable of resolving higher level flow details.

The compressed gas temperature calculated by the simulations is approximately 750 *K* and the maximum temperature that the model predicts is about 2600 K. A detailed uncertainty analysis for the combustion temperature is provided in [141] and [139]. It should be noted that since the piston in the current thesis is flat, it does not suppress the roll-up vortices that are generated during compression. Flow field inhomogeneity at TDC exacerbates turbulent intensity effects on jet development and combustion enhancement. Further details regarding the differences between creviced and flat pistons and their effects on the flow field of the reaction chamber can be found in [126].

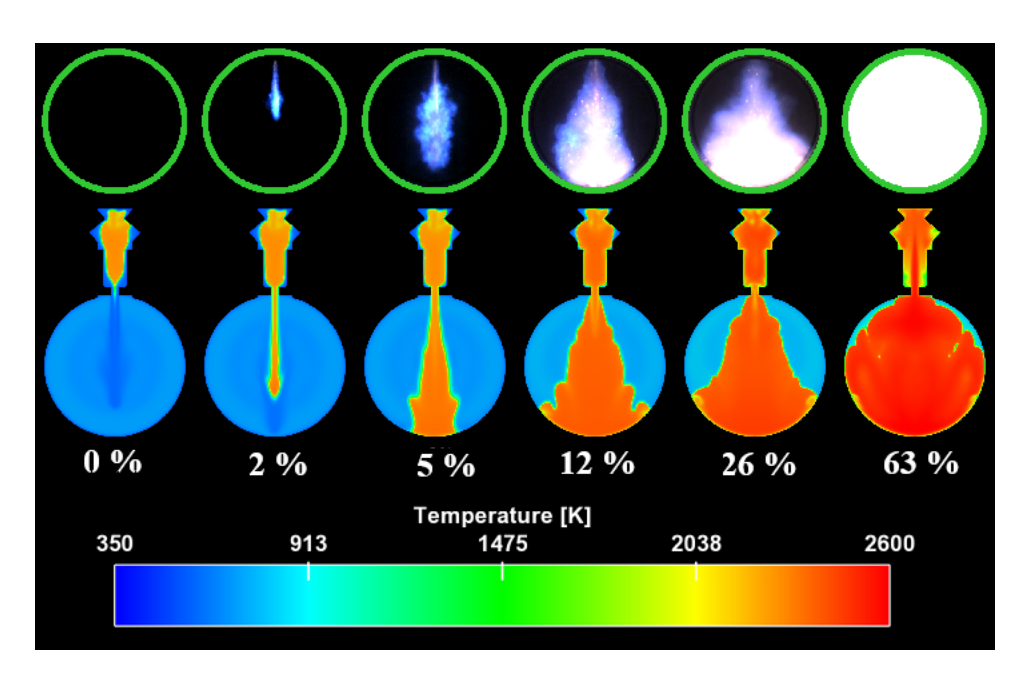


Figure 7-13- Comparison between the simulation's temperature contours and the experimental chemiluminescence images at similar burn duration times. Nozzle diameter=3.0 mm, λ = 1.25.

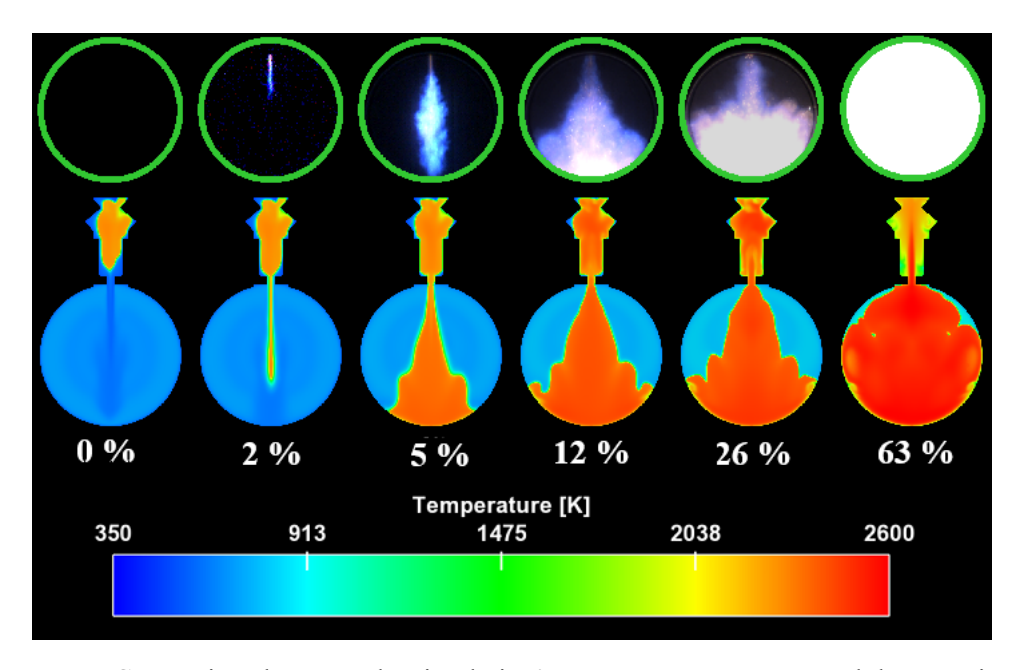


Figure 7-14- Comparison between the simulation's temperature contours and the experimental chemiluminescence images at similar burn duration times. Nozzle diameter=2.5 mm, λ = 1.25.

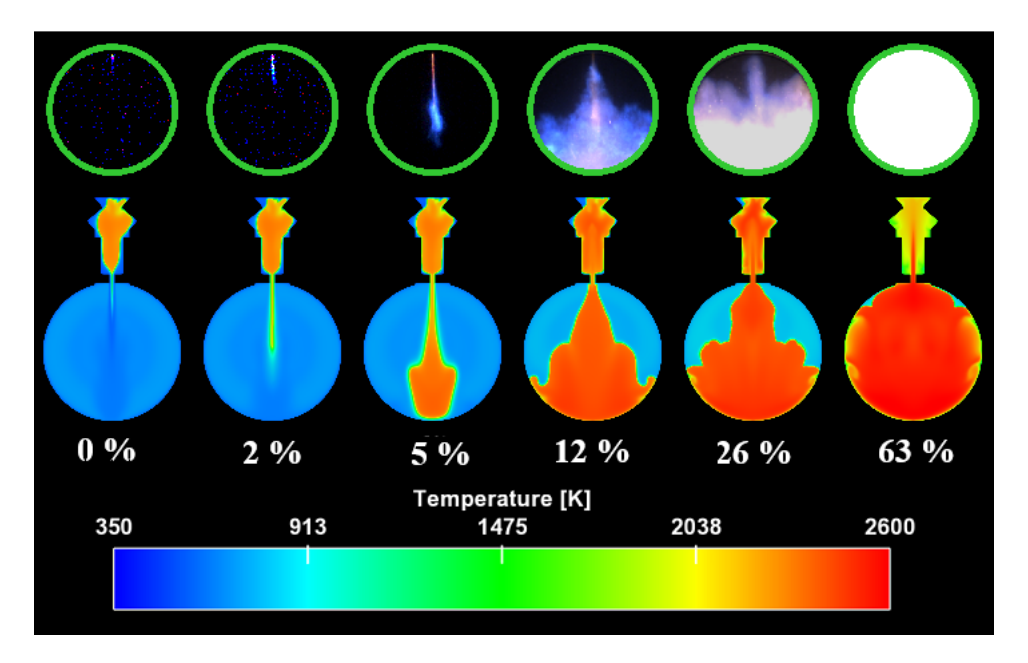


Figure 7-15- Comparison between the simulation's temperature contours and the experimental chemiluminescence images at similar burn duration times. Nozzle diameter=2.0 mm, $\lambda = 1.25$.

7-3 Chapter Summary

A series of numerical simulations were carried out to study the discharge of a hot reacting jet using the Converge code. Results were compared with the experimental measurements and the theoretical correlations discussed in [139]. A correlation based on first physical principles was introduced. CFD modeling of a methane fueled TJI system was used to provide further information on the flow field consisting of velocity, density gradient, and turbulent intensity inside the main chamber and prechamber. Simulation results were compared with the combustion visualization images captured during the combustion tests in the RCM for three orifice geometries (nozzle diameters 3.0, 2.5 and 2.0 mm) and mixture conditions in the range of stoichiometric to lean conditions (λ =1, 1.25 and 1.5).

The pressure traces of four comprehensive mechanisms and a reduced mechanism were compared with the experimental pressure data. Results showed that none of the mechanisms are in complete agreement, however they are in reasonably good agreement with the experiment in terms of burn rate, peak pressure and ignition delay prediction. Consequently, the reduced mechanism was used for the simulations. Results showed that as the mixture became leaner, the ignition delay time increased while the burn rate and maximum peak combustion pressure decreased. A time series of the velocity in the main chamber (at specific monitor points) and the nozzle throat were recorded during the run time. Results showed that the flow velocity in the nozzle throat and in the vicinity of orifice exit was highest for the smaller orifice diameter, however, near the chamber wall the large orifice jet was fastest. In addition, results showed that the maximum flow velocities occurred after the onset of the jet discharge leading to the conclusion that the flow inside the main chamber does not necessarily have its highest velocity at the moment when the hot jet becomes visible. As a result, a distinction should be made between the flow velocity and hot jet penetration speed. The

maximum flow velocity occurred when the mass has burned in the prechamber and the pressure has built up, while some of the burned gas has already exited the nozzle with a lower velocity compared to the subsequent jet flow.

Comparing the mass flow rate of the 3 orifices, the flow had its highest mass flow rate at the onset of the hot jet discharge. The 2.5 mm orifice had the highest mass flow rate. The nozzle exit velocity estimated by various correlations and simulation was in the range of 100 to 300 m/s for all cases resulting in a Reynolds number of $3-6\times10^4$ ($Re=\rho vd/\mu$ where d is the nozzle diameter).

Concerning the nozzle exit velocities as functions of time, the correlations of Figure 7-12 showed that when the velocities and the injection time interval are normalized, or non-dimensionalized as discussed in 7-2-4, the control volume model and the full numerical model agreed. The normalized functional dependences were very nearly the same. Figure 7-12 indicates that the actual jet injection process is complex and highly transient.

To compare the temperature contours with the experimental images, the numerical pressure traces are scaled to match the start of combustion and the peak pressure with the corresponding values from the experiment to produce an accurate time basis for comparison. Modeling contours showed that the maximum temperature in the domain varies based on the mixture condition and it was as high as 2600 K for the stoichiometric case. Furthermore, modeling contours showed that the unburned mixture cold jet discharges prior to the hot reacting jet, increasing the turbulent intensity in the main chamber and forming a path for the hot jet that includes active radicals. As a result, the turbulent jet decreases the reaction time in the main chamber and facilitates lean burn combustion.

Chapter 8 RANS Modeling of a Homogeneously Charged Turbulent Jet Ignition System

A thorough numerical investigation of the transient turbulent jet and ignition processes of a premixed methane-air mixture of a turbulent jet ignition (TJI) system is performed using Converge computational software to achieve a better understanding of the flow physics. A comparison is made between the numerical contours and the optical images obtained from combustion visualization experiments in an optically accessible RCM. In addition, the numerical pressure traces are compared with the experiments. The RANS RNG k-ε model is chosen to solve for the flow field.

8-1 Results

The purposes of this chapter is to numerically investigate the effect of variations in orifice diameter. Three simulations are performed at a lean condition (λ =1.25). The geometry is the same for all cases except for nozzle diameter, which varies between 3.0, 2.5 and 2.0 mm.

A comparison of numerical pressure traces from CFD RANS modeling and corresponding experimental data is shown in Chapter 7 and is repeated in Figure 8-1. The CFD simulations closely follow the experiments in the compression part, however, some discrepancies are noted after the ignition time is approached. CFD simulations typically do not predict accurate combustion burn rates and peak pressures. This is believed to be mainly due to non-adjustability of the chemical kinematics at high pressures. Another main reason for this discrepancy is the crevice volumes that are removed from the simulations in order to minimize unnecessary computational costs. Crevice volumes are located around the injectors (in the actual physical experimental setup two injectors are located in the prechamber but not used for these simulations) and in the connection between the prechamber and main chamber. Although these volumes are small, they contribute to the numerical pressure inaccuracy. However, it is believed that the crevice volume effects are not as important as the mechanism inaccuracy at high pressures. Further details on the effect of the crevice volume is provided in Appendix D.

Half-way through the combustion period, the simulation pressure traces begin to deviate from the experimental traces. The close-up view of the compression and combustion stages are shown in Figure 8-2.

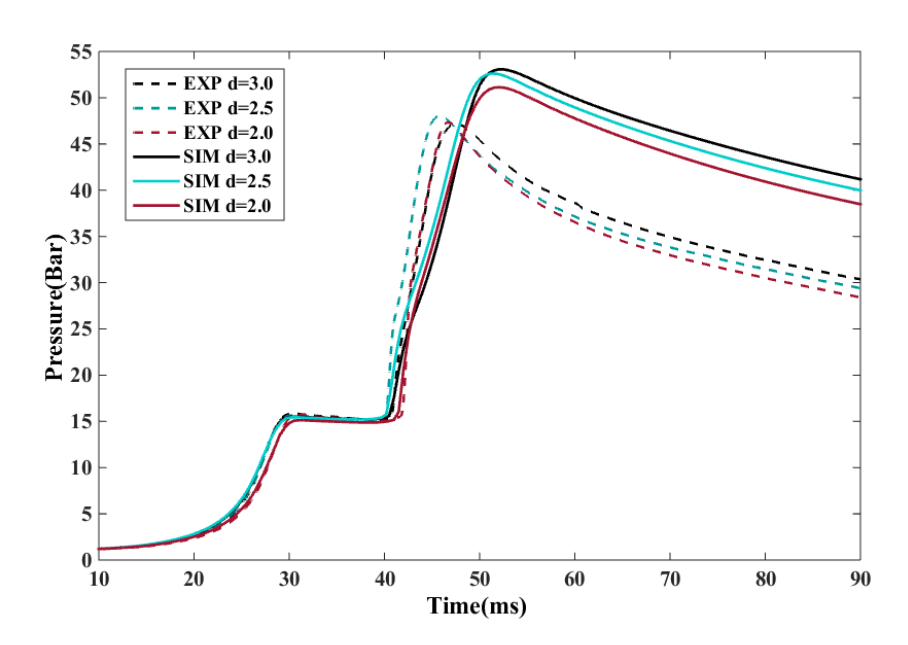


Figure 8-1- A comparison between all the RANS simulation and experiment's pressure results, λ =1.25. Note that the deviation of the simulations and experiments becomes large in the active combustion stage, where the pressure rises to its peak value.

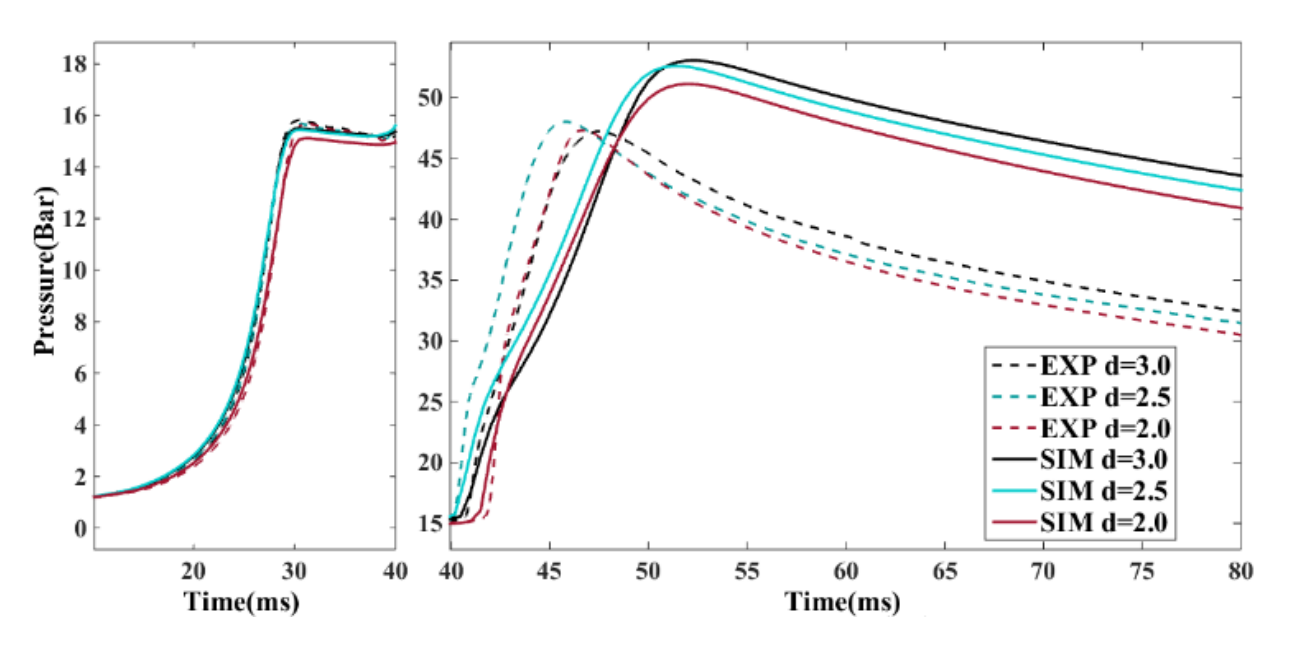


Figure 8-2- A comparison between all the RANS simulation and experiment's pressure results, λ =1.25 in compression (left) and combustion (right) stages.

The pressure rise inside the prechamber and the pressure imbalance between the two chambers leads to the discharge of a hot jet of reacting mixture and active radicals from the prechamber into the main chamber. Figure 8-3 shows a comparison between the numerically computed pressure of

both main and pre chambers and the experimental measurements and a close-up view of the pressure at the onset of jet discharge. Figure 8-3 illustrates that the pressures of both chambers are almost identical except during the onset of the jet discharge.

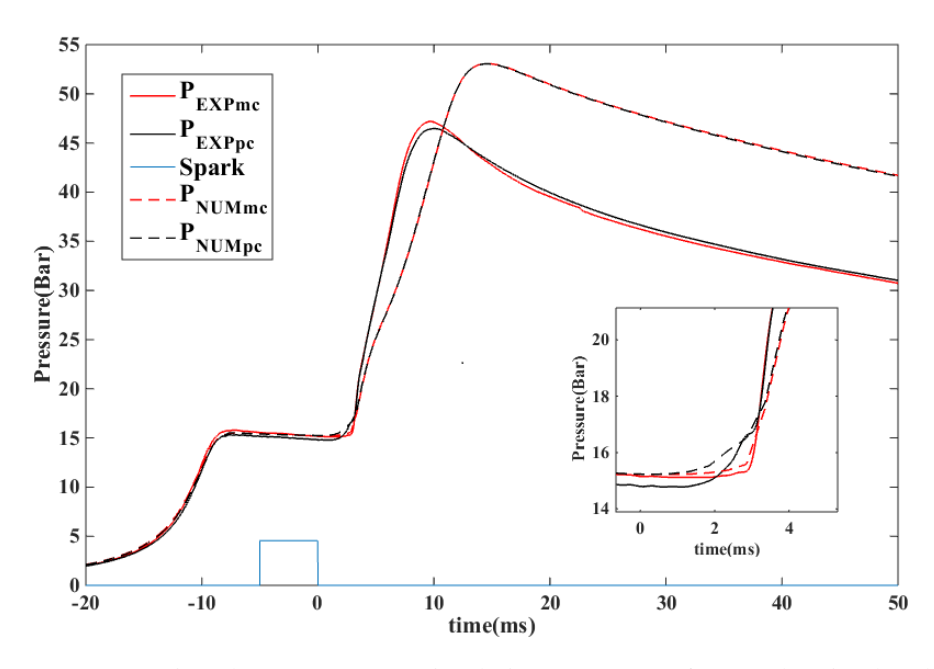


Figure 8-3- A comparison between RANS simulation pressures of pre and main chambers and experimental measurements, nozzle diameter=3.0 mm and λ =1.25.

A comparison between the numerical pressure trace of LES modeling and experimental measurements is shown in Figure 8-4. The LES model with a Smagorinsky sub grid scale shows a better burn rate compared to the RANS models (see Figure 8-1). However, the peak pressure estimation has an 8% error (the simulation pressure is ~ 4 bar higher than the experiments).

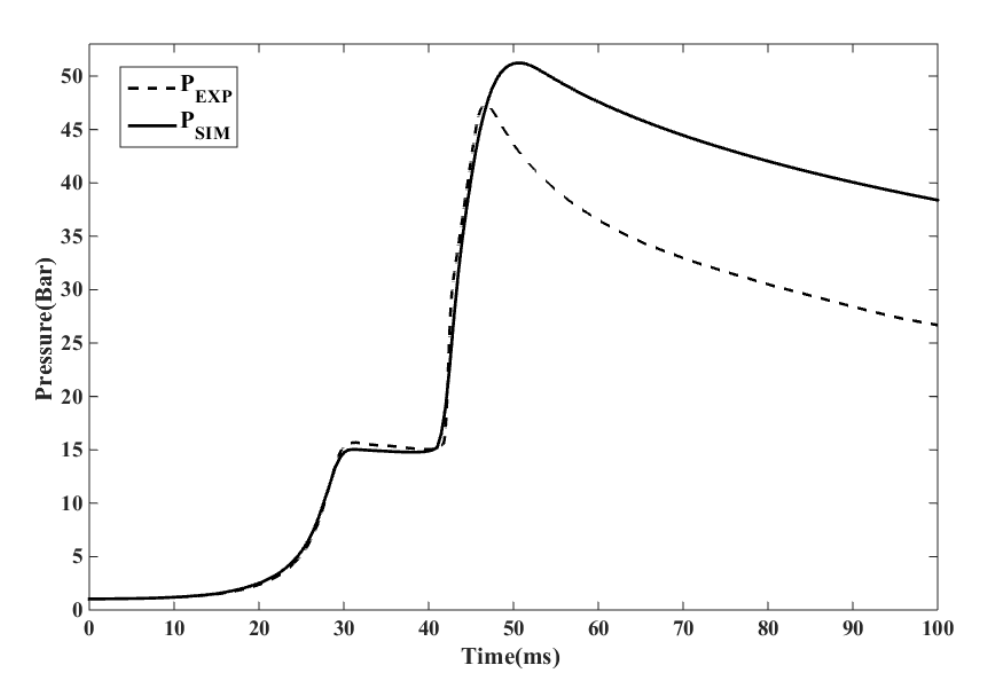


Figure 8-4- A comparison between main chamber LES simulation pressure and experimental measurements, nozzle diameter=2.0 mm and λ =1.25.

The 0-10% burn duration of the pressure rise due to combustion is an indicator of flame initiation and the 10-90% burn duration of pressure rise characterizes the flame propagation speed. The difference between an RCM and engine burn durations are described in [22]. The mean 0-10% and 10-90% burn durations are illustrated in Figure 8-5. Here, the start of combustion is defined where the pressure deviates from linearity (analyzing the first and second derivations of pressure data from the RCM). In general, the 3 mm orifice jet, although almost identical to the 2 mm orifice jet, has a shorter 0-10% burn duration compared to the two other geometry configurations. However, with the smaller orifice, the flame initiation is about 0.5 milliseconds longer. These results are in contradiction with [22] in which propane-air mixtures were investigated. The difference in the fuel type (methane-air mixtures are investigated in this thesis) is thought to be the cause of this effect.

The 10-90% burn duration results (Figure 8-5-right) are in good agreement with [22]. The overall 10-90% burn durations are less than 10 msec and the smaller orifice has the shortest burn duration while the 3 mm orifice jet is slower than the other configurations. Results imply that for near

stoichiometric conditions (i.e. λ =1.25) the orifice size has a very small influence on burn duration and combustion performance. As a result, in order to have faster combustion (0-90%) with poor ignition quality mixtures (i.e. lean mixtures), a smaller orifice is more effective. Gentz et al. [22] explained that this phenomenon is due to the higher turbulence rate provided by the turbulent jet and consequently the allowance of more active radicals to expedite the combustion process. Adding both the 0-10% and 10-90% burn durations, it is clear that the smaller orifice has a shorter overall burn duration for all mixture conditions. As the orifice diameter increases, the overall burn duration increases.

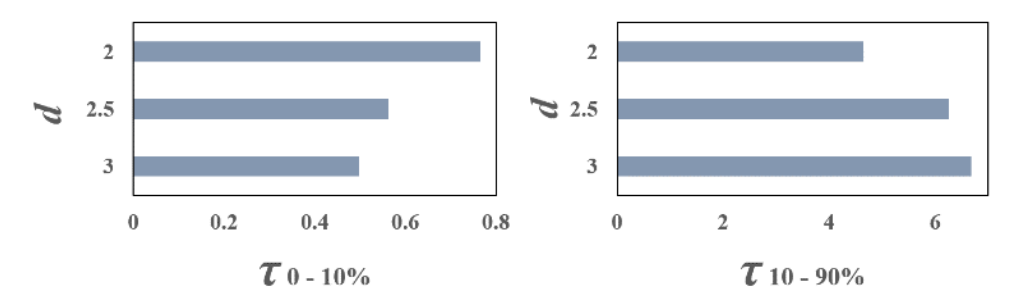


Figure 8-5- Experimental 0-10% and 10-90% burn durations, λ =1.25.

Since the 0-100% combustion period is longer than the experimental results and the pressure rises predicted by modeling are higher than the experimental peak pressures, to compare the numerical contours of variables such as temperature or turbulent kinetic energy, it is appropriate to normalize the pressures. Consequently, comparisons can be made at similar burn duration points with respect to the start of combustion. Normalized pressures are presented in Figure 8-6. For more details see section 7-2-5.

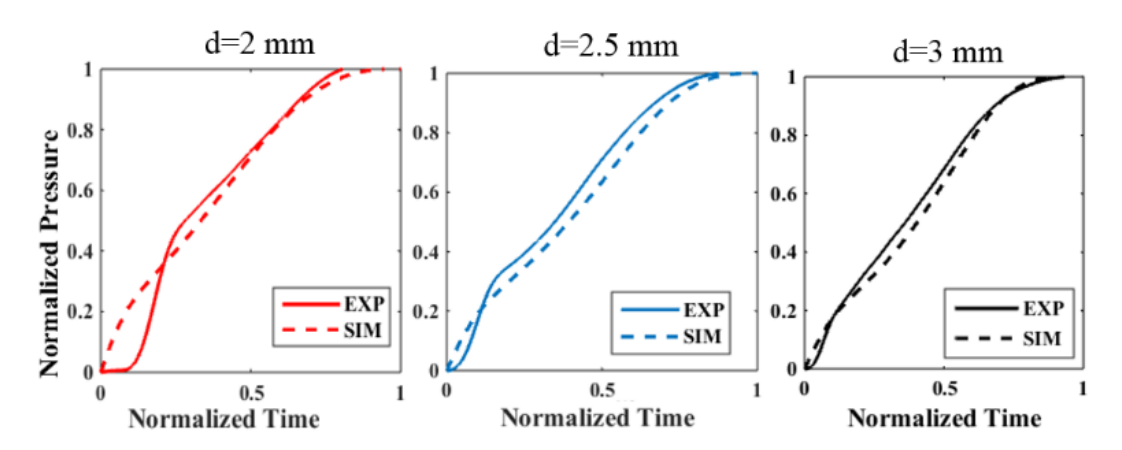


Figure 8-6- Normalized combustion period pressure plots, indicating similarity of the normalized profiles.

Once the pressure data is normalized, numerical contours can be compared with experimental images for similar stages of combustion [0%, 2%, 5%, etc.]. Figure 8-7 to Figure 8-9 show and compare the temperature fields with corresponding chemiluminescence images (these figures are shown in Chapter 7 and are repeated here with more detailed explanation). For the 3.0 mm orifice, the jet is wider and faster compared to the other nozzle configurations. A faster and more vigorous initial jet of 3.0 mm orifice can be explained by the wider opening of the orifice compared to the two other geometries. A wider orifice introduces fewer restriction against the flow, hence, more mass flow through the nozzle which forms a more powerful jet. In contrast, the flow restriction of smaller orifices is higher. On the other hand, as the jets reach the end wall, the burn rate and flame propagation speed in smaller orifice configurations is higher than that of the bigger orifice. This phenomenon can be explained by the amount of turbulent kinetic energy (TKE) in the domain. Images of TKE contours are presented later. In addition, further investigation of jet penetration speed and velocity prediction at the nozzle throat were discussed in Chapter 6 and Chapter 7 [139]. The following figures further shows the existence of a comparatively cold jet of unburned products that enters the main chamber prior to the hot jet of combustion products. The images illustrate that

jet ignition leads to a more distributed combustion, while also improving the flame propagation

rate. In addition, larger scale structures of the turbulent jet can be seen at the flame margin of the images. The RANS CFD simulations are unable to capture all of the vortices due to the time averaging nature of RANS. The LES results, however, capture some of these structures.

Figure 8-9 shows the ability of LES models in large and small scales of turbulent flow during the jet penetration and flame propagation periods. Because of computational costs, simulation results of LES modeling for only one nozzle geometry were prepared and provided in this chapter, the complete LES results are provided in Chapter 9.

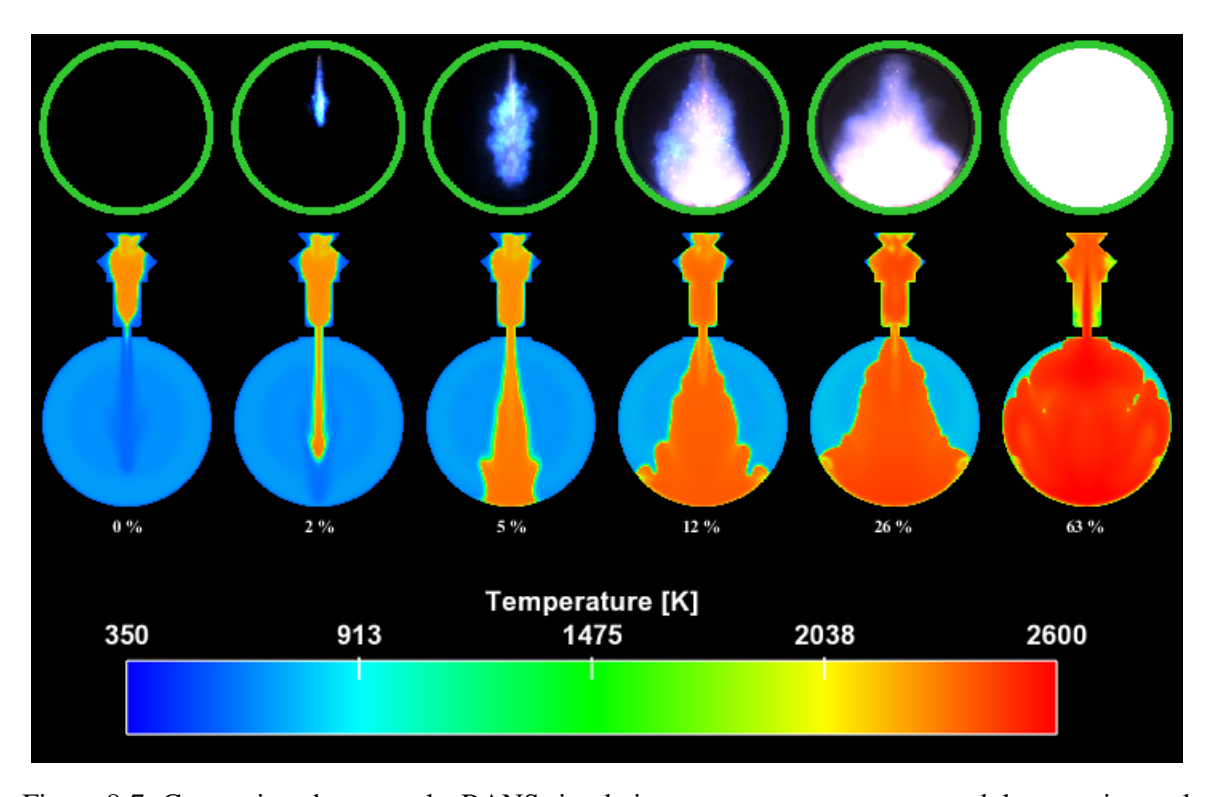


Figure 8-7- Comparison between the RANS simulations temperature contours and the experimental chemiluminescence images at similar burn duration times. d=3.0 mm, λ =1.25.

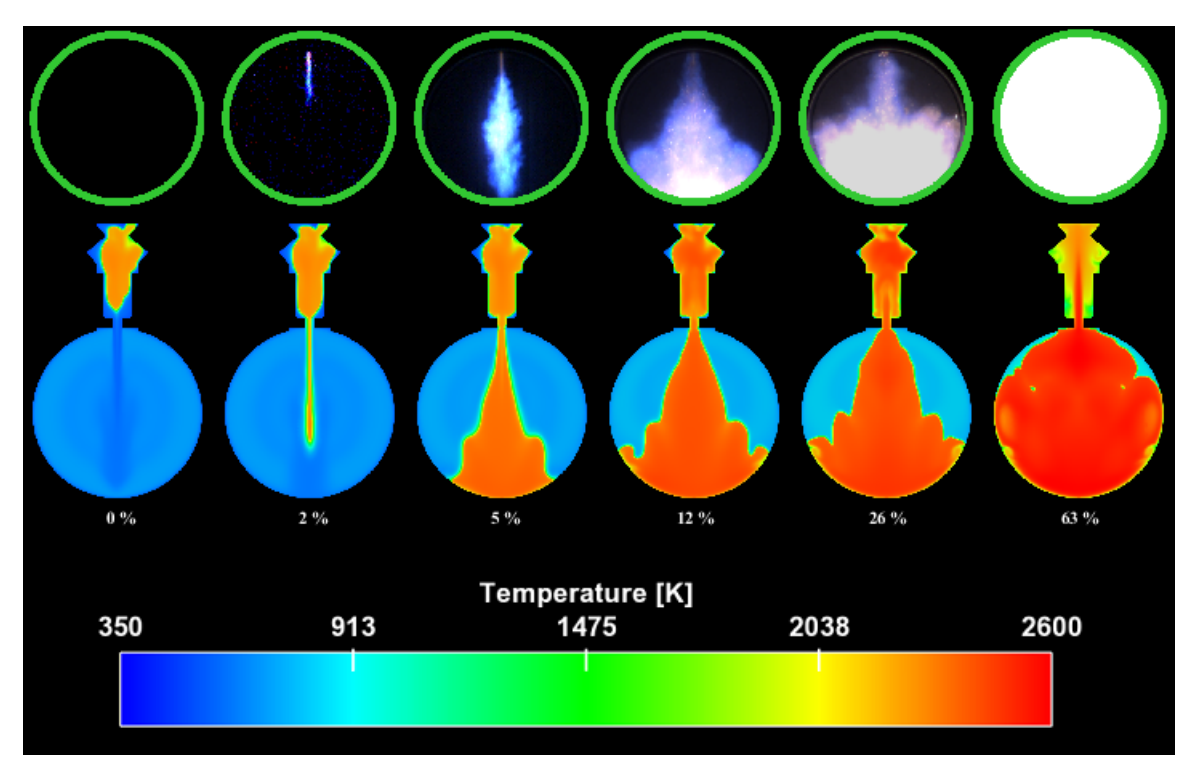


Figure 8-8- Comparison between the RANS simulations temperature contours and the experimental chemiluminescence images at similar burn duration times. d=2.5 mm, $\lambda=1.25$.

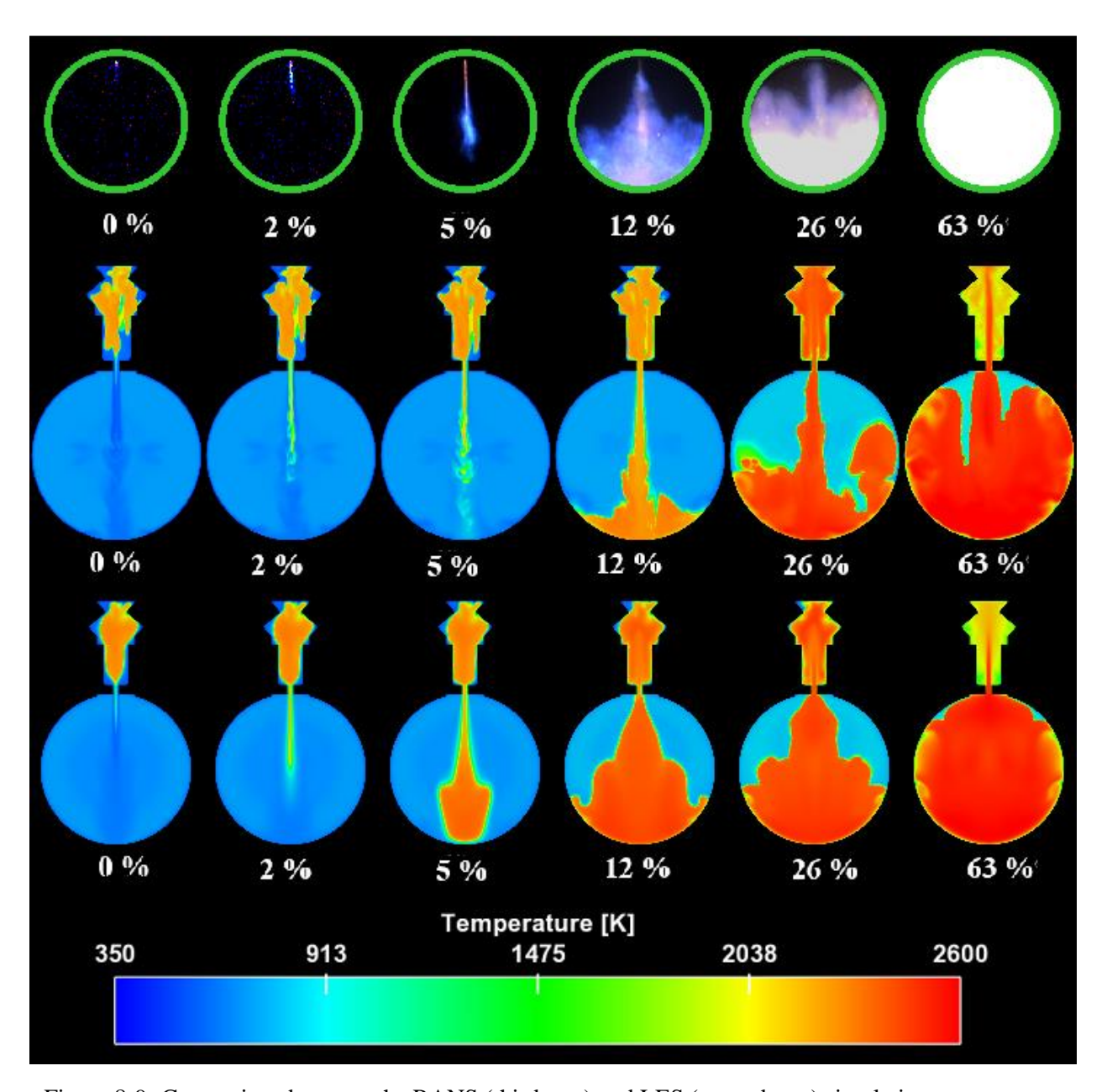


Figure 8-9- Comparison between the RANS (third row) and LES (second row) simulations temperature contours and the experimental chemiluminescence images (first row) at similar burn duration times. d=2.0 mm, λ =1.25.

Figure 8-10 shows the turbulent kinetic energy in the domain from the beginning of hot reacting jet discharge to over 50% of burn duration. Similarly, the turbulent dissipation rate contours from the RANS simulations are shown in Figure 8-11. It is seen that the discharge of the cold jet increases the turbulent kinetic energy in the main chamber and that TKE increases even more by

the discharge of hot reacting jet. Meanwhile, the turbulent dissipation rate in the main chamber increases with the jet discharge. The dissipation rate is a maximum in the combustion stage. Due to the combustion progress and flame propagation, the turbulent kinetic energy decreases and it starts to fade away when about 12% of the charge is burned. When burning process reaches to 25%, TKE in the main chamber is almost zero, however, the reverse flow (from the main chamber to the prechamber), increases the TKE of the prechamber. Reverse flow resulting from pressure rise in the main chamber forces the main charge to flow back into the prechamber.

Comparing the contours of the various orifice areas, the 3.0 mm jet penetrates faster, ignites more fuel in the main chamber at a shorter period of time and consequently, turbulent kinetic energy and mixing vanish in the main chamber. This phenomenon reduces the penetration speed of the jet in the later stages of combustion (i.e. when the jet reaches the chamber wall). Furthermore, the reverse flow results in higher turbulent kinetic energy in the prechamber for the 2.0 mm orifice. It does not have a large impact on the overall burn rate.

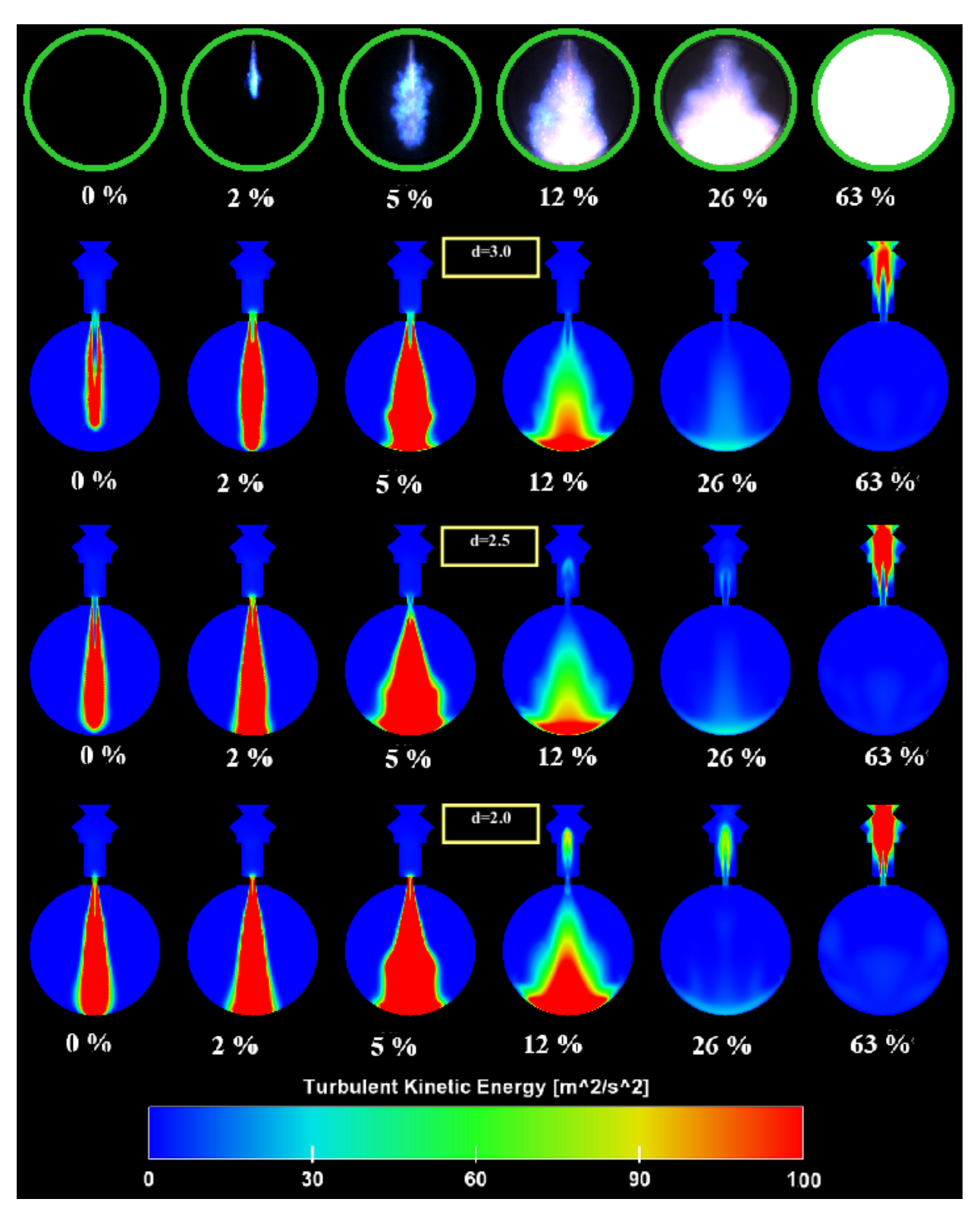


Figure 8-10- Comparison between the simulation's turbulent kinetic energy contours at similar burn duration times, λ =1.25.

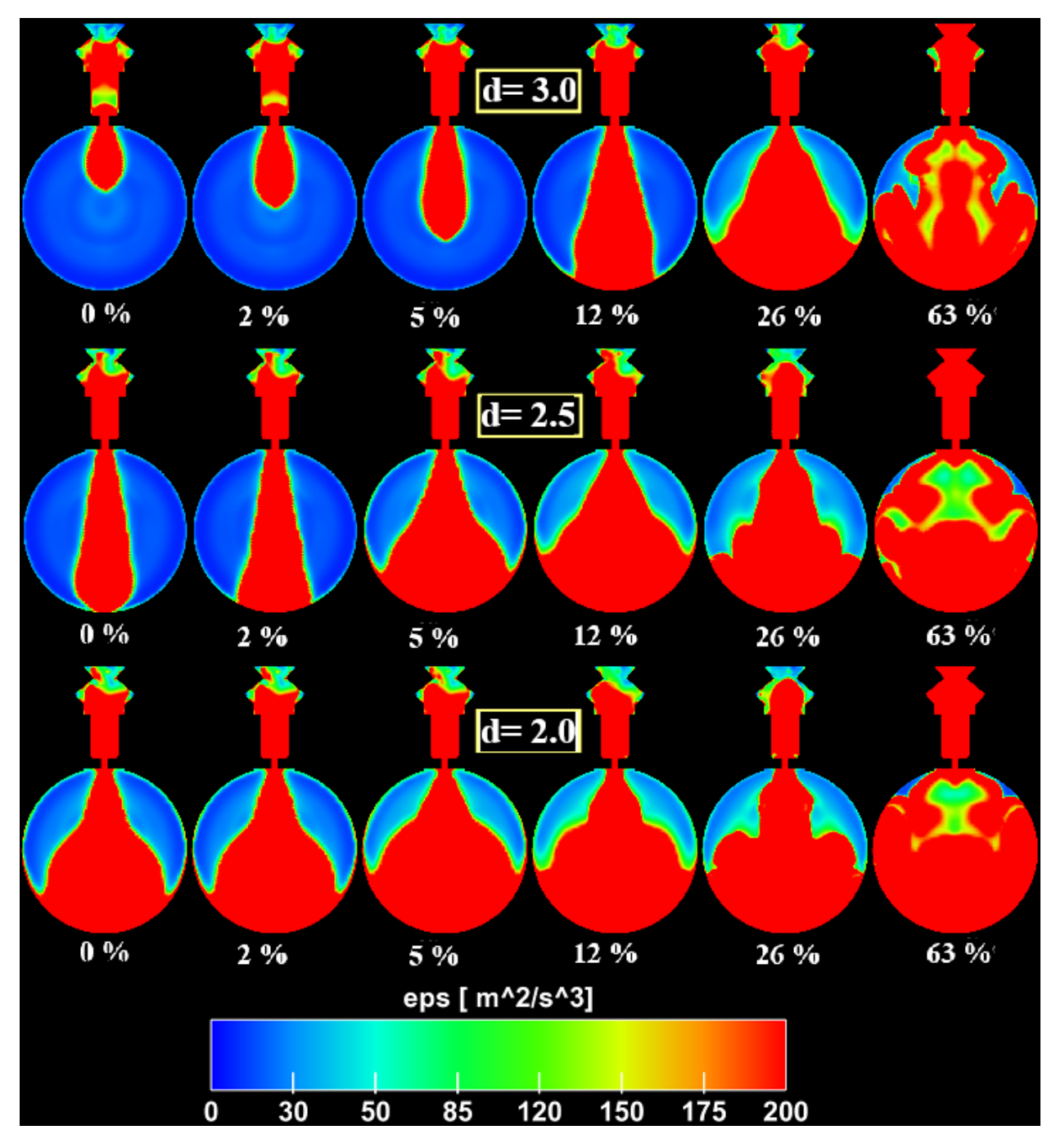


Figure 8-11- Comparison between the simulation's turbulent dissipation rate contours at similar burn duration times, λ =1.25.

8-2 Chapter Summary

Three-dimensional transient CFD simulations were performed to address the effect of orifice diameter on the flow field, burn duration and combustion of methane fueled TJI in the MSU rapid compression machine. The initial penetration speed and flame propagation of the wider opening nozzle were higher than smaller orifices. The smaller orifices led to a faster combustion in the later stages of ignition (when the jet hits the main chamber wall). Overall combustion rates were always faster for the smaller orifices. These results were evaluated by CFD modeling as well. CFD pressure curves showed close compatibility with experiments in the compression stage, however, the burn rate, burn duration and maximum pressures predicted numerically were not in exact agreement with experiments. Two main reasons for this are the unsuitableness of the chemical mechanism used for high pressure combustion (over 40 bar) and the removal of crevice volumes that led to a generally smaller CFD volume. The latter alleviated computational costs.

The numerical and experimental pressures were normalized. Modeling contours and chemiluminescence images were then compared at normalized combustion levels. Temperature contours at normalized burn duration illustrated good agreement with images. The maximum temperatures observed in the domain was approximately 2500 K. Two interesting conclusions made by CFD results were the discharge of cold jet prior to the reacting jet of combustion products, at the initial stages of combustion, and the reverse flow from the main chamber to prechamber in the later stages of combustion. Computational results were greatly revealing because many flow field variables such as the velocity, density and temperature distributions are fundamental physical variables that define the turbulent jet, and the main chamber flow field, and in the current experiments can be determined from the computational investigations.

The chapter suggests that the use of a wider opening nozzle is more desirable because it improves jet penetration. On the other hand, a smaller orifice magnifies turbulent intensity in the main chamber and consequently is more efficient during the later stages of combustion. Simulations confirmed the creation of a high turbulent kinetic energy region in the main chamber as a result of cold jet discharge, facilitating the increase of mixing and improve combustion, as well as the creation of a non-uniform density and turbulent intensity distribution. This thesis also suggests using LES turbulent models in place of RANS simulations when the requisite computational resources are available. LES models provide more details of the pressure, temperature and velocity fields showing smaller scales of the turbulent flow. LES models also provide a more accurate burn rate prediction compared with the experimental measurements. Finally, the use of a reduced mechanism was highly recommended for future studies of TJI combustion in rapid compression machines.

Chapter 9 LES Modeling of a Homogeneously Charged Turbulent Jet Ignition System

Chapter 8 was devoted to the computational study of the transient jet ignition of a homogenous methane air mixture in a TJI system using a RANS turbulence model. In this chapter, a Large Eddy Simulation (LES) turbulent model is used for the transient jet ignition study. The influence of orifice size and mixture stoichiometry is studied through simulations performed with the Converge CFD code. A reduced chemical kinetic mechanism with 122 reactions and 23 species is used for combustion modeling along with a zero-equation Smagorinsky sub-model for turbulence modeling. The computed pressure traces are compared with experimental data measured through the Rapid Compression Machine (RCM) tests. Pressure traces are scaled and CFD temperature contours for various nozzle orifices and air-fuel ratios are compared in order to achieve deeper insight into the TJI combustion process in the RCM combustion cylinder, the numerical iso-surface temperature contours (800, 1200, 2000, and, 2400 K) were obtained which enabled 3-D views of the flame propagation, the jet discharge, ignition and extinction events, and the heat release process. The heat release process and regeneration of mid-range temperature iso-surfaces (1200 K) were not visible through the experimental images available in the MSU RCM.

9-1 Results

The simulations were performed for three nozzle dimeters (d=2.0, 2.5 and 3.0 mm) at air-fuel ratios of λ =1.0, 1.25 and 1.5. Initially, the calculated pressure from the numerical simulations are compared to the experimental measurements for various lambda conditions, followed by a discussion of the thermodynamic variable contours. Figure 9-1 and Figure 9-2 illustrate a comparison between pressure traces measured during the experiments and the corresponding LES simulations for the stoichiometric and the lean case of λ =1.25, respectively.

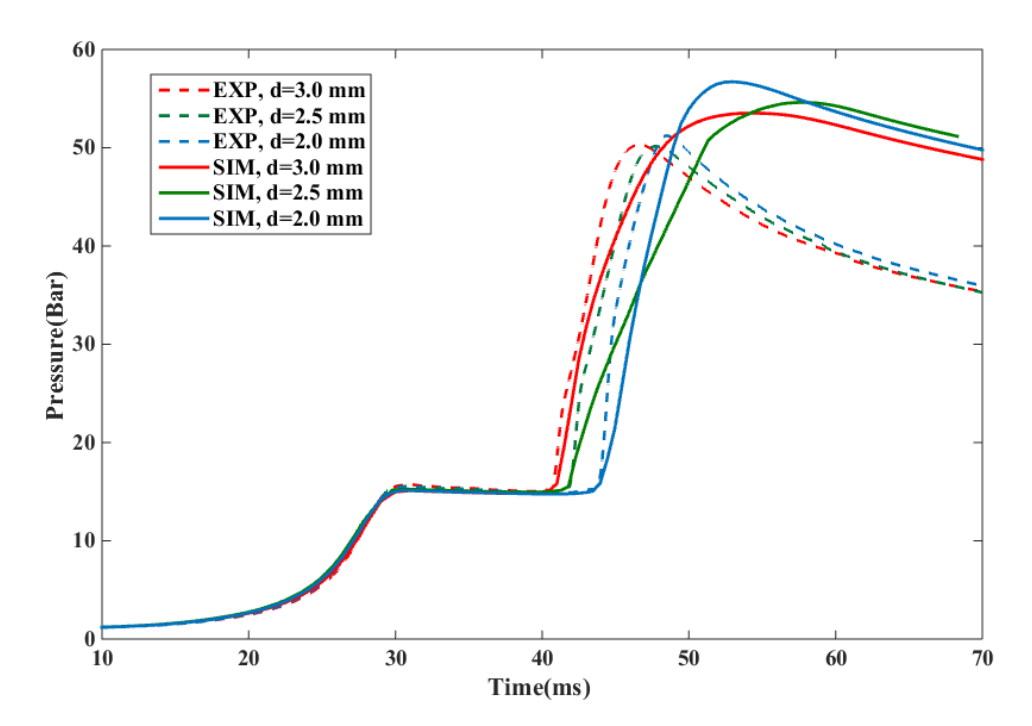


Figure 9-1- Pressure trace comparison between experimental measurements and numerical simulations, $\lambda=1.0$.

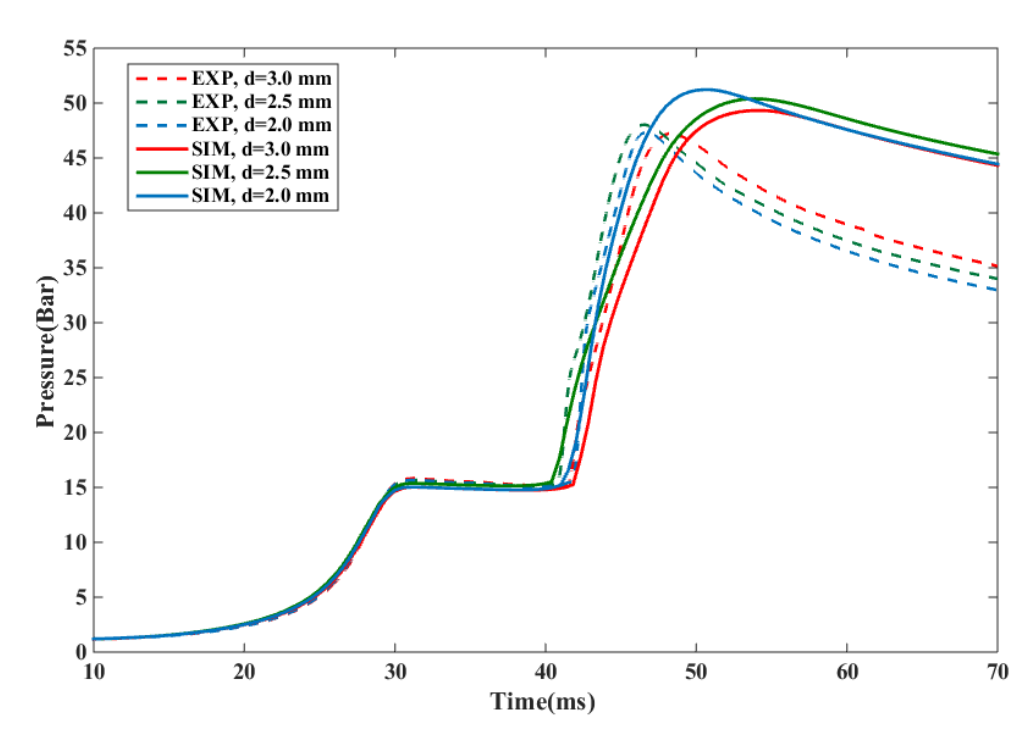


Figure 9-2- Pressure trace comparison between experimental measurements and numerical simulations, $\lambda=1.25$.

During the compression stroke, the pressure reaches to 16 bar. At the end of the compression stroke, when the piston is stationary, the spark energy is discharged in the prechamber. Until the start of combustion, the numerical simulations follow the experimental results closely. For the combustion stage, however, there is some discrepancy between the numerical results and the experimental measurements of burn rate, burn duration and peak pressure. One reason for this discrepancy is attributed to the fact that the crevice volumes present in the experiments were neglected in the modeling to reduce computational time. In the experiments unburned mixture that is trapped in the crevice volumes of the combustion chamber and the TJI assembly, remains unburned, which results in lower experimental peak pressure. An estimate of the unburned mass that is trapped in the crevice volume and its effect on the pressure rise is provided in Appendix D. In addition, the chemical kinetic mechanism also contributes to the discrepancies particularly at higher combustion pressures, where the mechanism is not well validated (> 31.4 atm [142]).

Lastly, a part of the discrepancy is attributed to the numerical methods. In the current thesis, the use of the LES turbulence model resulted in an improvement in calculated burn rate and peak pressure that better matched with experiments.

In terms of the orifice size comparison, a major difference can be seen in the jet discharge and the start of combustion in the main chamber. Further details can be found in Chapter 6 and Chapter 7 [19, 139]. In addition, results show a decrease in peak pressure by increasing air-fuel ratio and change of burn rate. In general, as the mixture becomes leaner, the peak pressure decreases and the mixture burns at a slower rate. Once the pressure reaches a maximum, it decreases due to the heat losses to the chamber wall. In the simulations, a constant temperature boundary condition is used to match with the constant temperature of the experimental chamber walls (80 °C).

In order to better understand and to compare the simulation and experimental results, three methods were used to present the modeling results. First, a planar surface located in the y-z plane passing through the centerline of the orifice was employed as the reference cross sectional view. Second, three planes were placed in the domain, one passing through the centerline of the orifice and the other two located in front of and behind the central plane, equidistant between the nozzle and the edges of the chamber. An isometric view of the three planes is shown in Figure 9-3. In order to visualize gradients in the presented variables (such as temperature, OH mass fraction, etc) or the flame area, the transparency of each plane was set to 50%. Lastly, a 3-D isometric view was used to show iso-surface contours, as can be seen in Figure 9-4 to Figure 9-7.

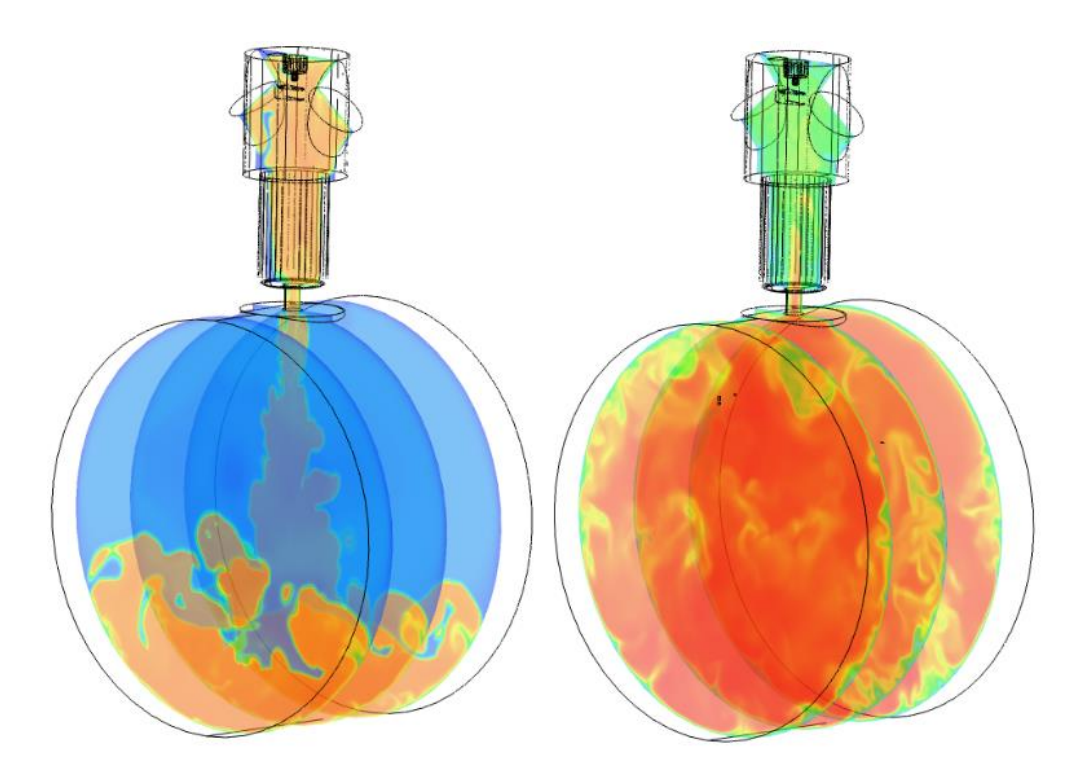


Figure 9-3- Isometric view of three clip planes showing their placement relative to each other.

Experimental chemiluminescence images are compared to the transient evolution of the LES temperature profile in the central *y-z* plane that passes through the orifice (2nd row), multi-plane temperature contours (3rd row), and mid-range temperature iso-surfaces (1200 K) (4th row) at synchronous burn rates, as shown in Figure 9-4 to Figure 9-6. The LES approach, although computationally expensive, is more precise in the calculation of large and small scales of turbulent flow for the jet penetration and flame propagation periods. The images show how the jet discharge leads to a fast and strong flame propagation whereas the LES contours capture large scale structures of the turbulent jet at the flame front and during the discharge of the colder non-reacting jet prior to the hot reacting jet. The non-reacting (cold) jet is shown with the dark blue color in the temperature contours. This is not visible during the experiments as it is non-reacting and produces no visual markers. In addition, since the measurement of temperature inside the reacting chamber was not feasible in these experiments, the maximum temperature of the domain is estimated

through the simulations. The stoichiometric and lean mixture conditions (λ =1.25, 1.5), reach approximately 2600, 2300, and, 2000 K, respectively.

Results show that a more stable and wider jet is seen with the larger orifice due to fewer restrictions to the flow. On the other hand, the smaller orifice jet faces more restriction, which results in a jet with reduced width in the vicinity of the nozzle. This jet has a higher velocity and penetrates faster, leading to a higher turbulent intensity in the main chamber, which contributes to an improvement during the later stages of combustion. This sequence of events was described at length in Chapter 8.

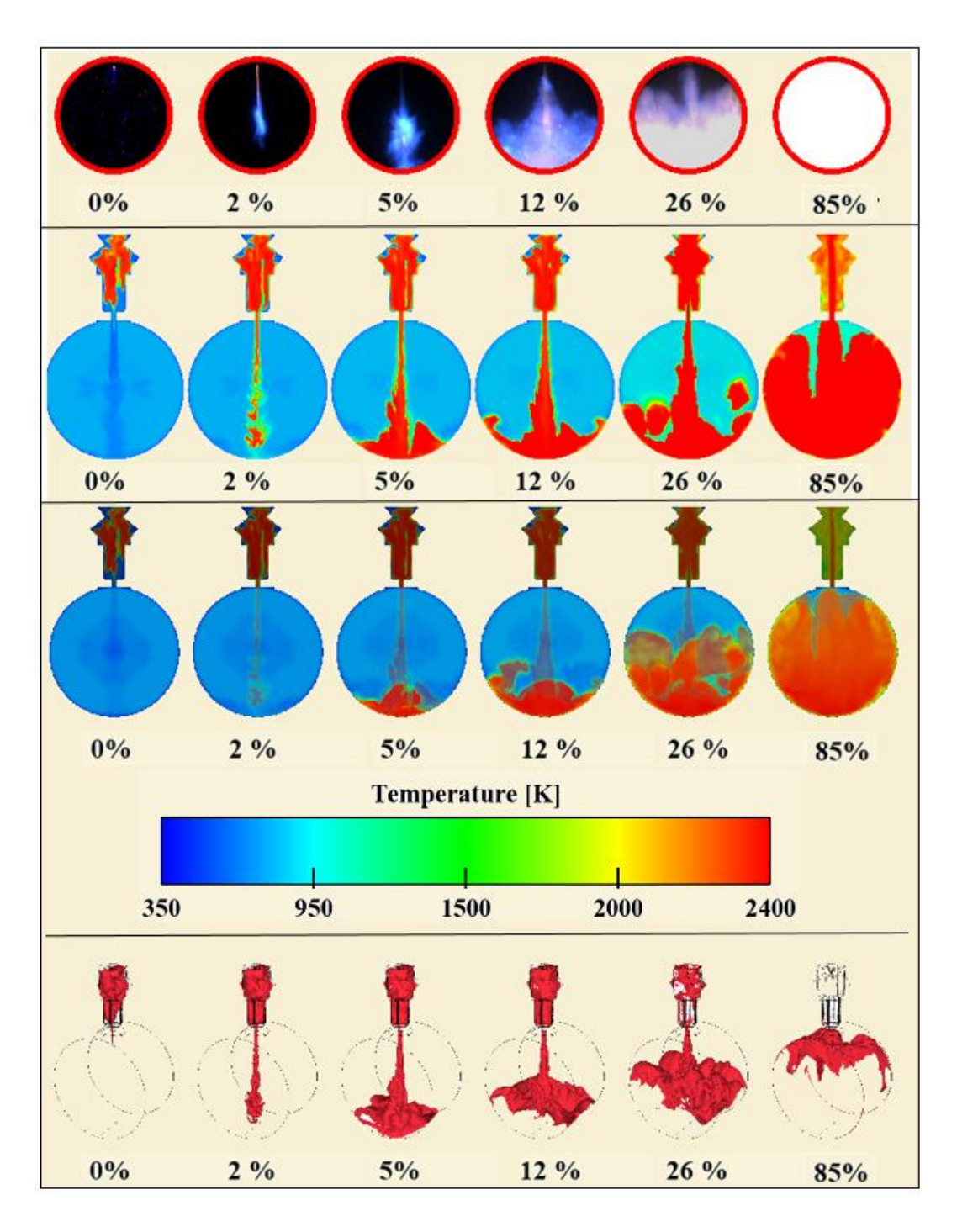


Figure 9-4- Chemiluminescence images of combustion (1st row) and LES temperature and mid-range isosurface contours (2nd, 3rd and 4th rows, respectively), d=2.0 mm, at λ =1.25.

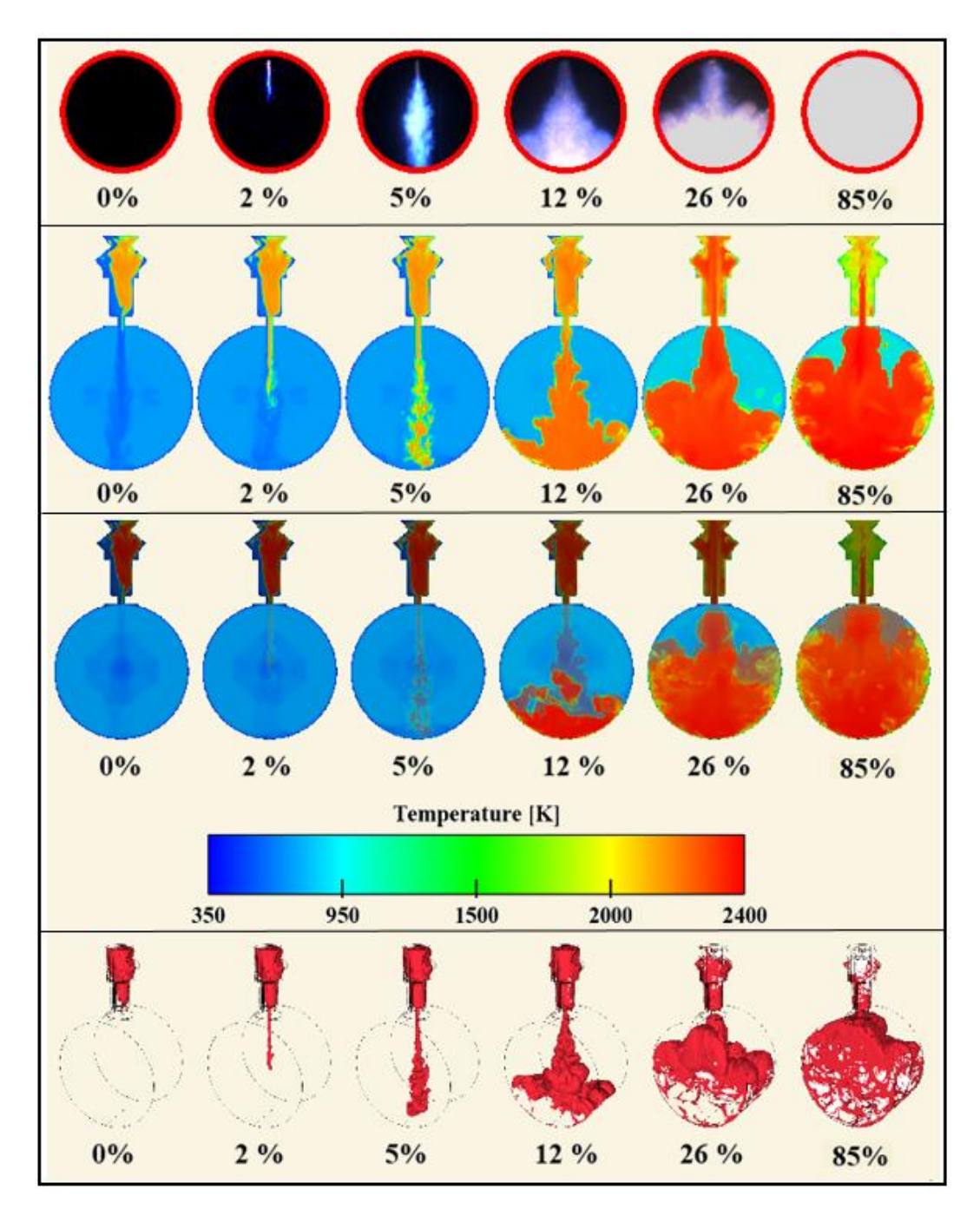


Figure 9-5- Chemiluminescence images of combustion (1st row) and LES temperature and mid-range isosurface contours (2nd, 3rd and 4th rows, respectively), d=2.5 mm, at λ =1.25.

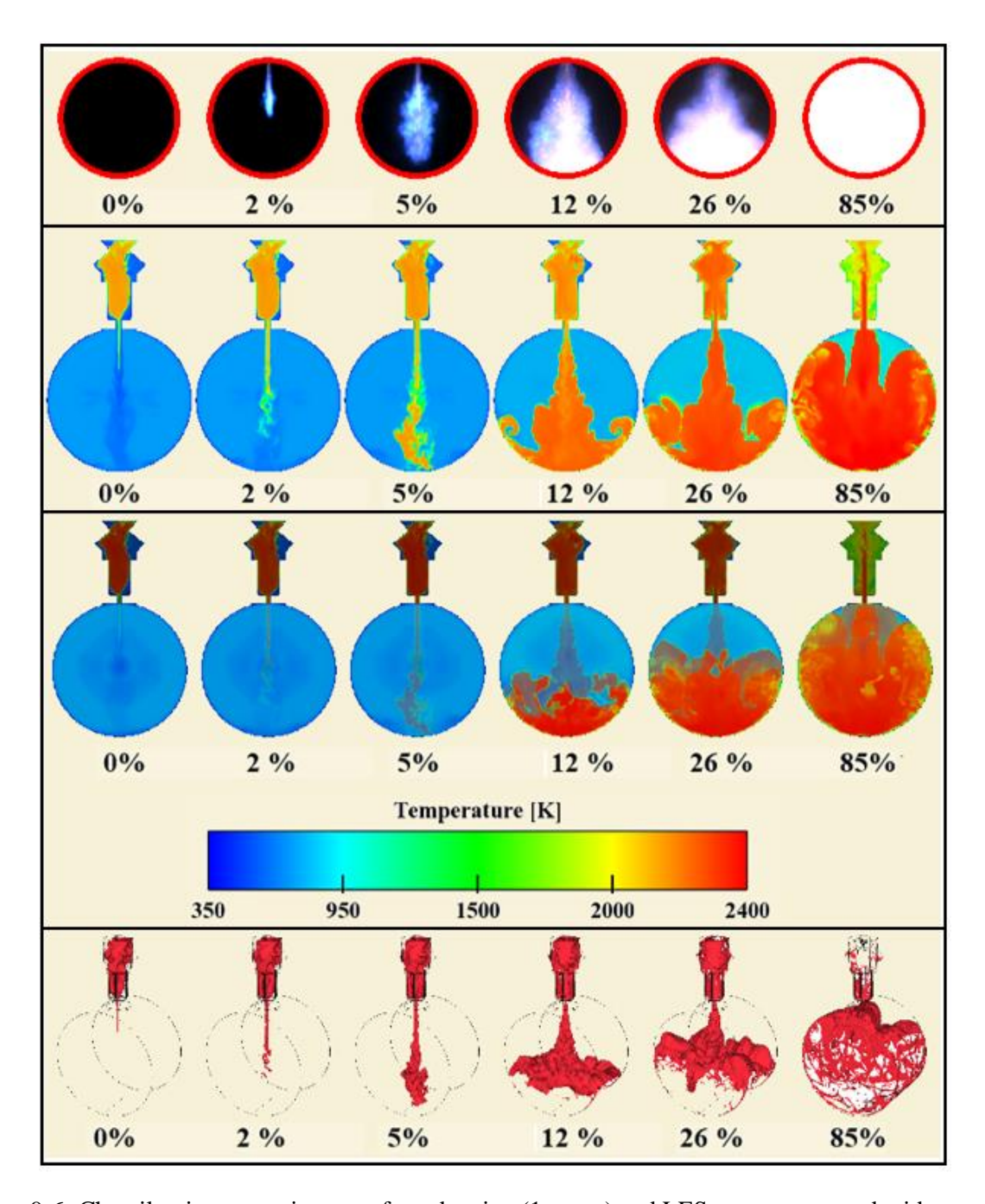


Figure 9-6- Chemiluminescence images of combustion (1st row) and LES temperature and mid-range isosurface contours (2nd, 3rd and 4th rows, respectively), d=3.0 mm, at λ =1.25.

Comparing the second and third rows of Figure 9-4 to Figure 9-6, the lateral flame propagation in the main chamber (in *x-z* plane) is not always visible in the central plane. In order to locate the flame front, the numerical results combined from multiple surfaces (as in the multiplane method) are taken into account. Since the experimental images represent all the visible light captured by

the camera, they can be thought of as the emitted light accumulated from an infinite number of cross-sectional planes inside the main chamber. As a result, the multiplane contours somewhat imitate the accumulation of data from the multiple planes, and form a more accurate representation of the flame front. They also show improved similarity with the experimental images.

The iso-surface sequence of images (4th row in Figure 9-4 to Figure 9-6) illustrates various stages of flame propagation in the prechamber (first frame), jet discharge and distribution (second and third frames), jet extinction (third frame-only for the small nozzle) and the combustion process in the main chamber (forth, fifth and sixth frames). As the volume of the burning mixture in the main chamber increases, the mixture temperature reaches above 2000 K and the area of 1200 K iso-surfaces reduces to a limited surface in the vicinity of the orifice exit. After the completion of combustion, the system cools due to heat transfer. The 1200 K iso-surfaces regenerate to cover the main chamber, as seen in Figure 9-7.

Comparing the iso-surface contours at 800 K, the mid-range temperature of 1200 K, 2000 K, and at the maximum temperature of 2400 K (which is close to the adiabatic flame temperature), it is seen that in the span of approximately 40 ms, the main chamber mixture cools and the high temperature iso-surface fades away while the mid-range temperature iso-surfaces regenerate. The temperature gradients in the domain are not visible in our experiments. Facilities employing Schlieren imaging are currently being constructed that will enable further insight into density gradients that occur during the TJI process in the future. In addition, once the main chamber charge has combusted, the pressure imbalance between the two chambers forces the reacting mixture to flow back into the prechamber, see Chapter 8. The cooling process starts from the boundaries and the mid-range and 800 K iso-surfaces regenerate on the wall of both the prechamber and main chambers while the core region of main chamber remains at 2000 K until

the end of the simulation. In addition, the 2400 K contour shows that although ignition starts in the prechamber, the end gas in the main chamber initially reaches close to the adiabatic flame temperature. From there the core region in the main chamber and some parts of the prechamber also reach 2400 K. The wall boundaries, however, never experience temperatures as high as 2400 K.

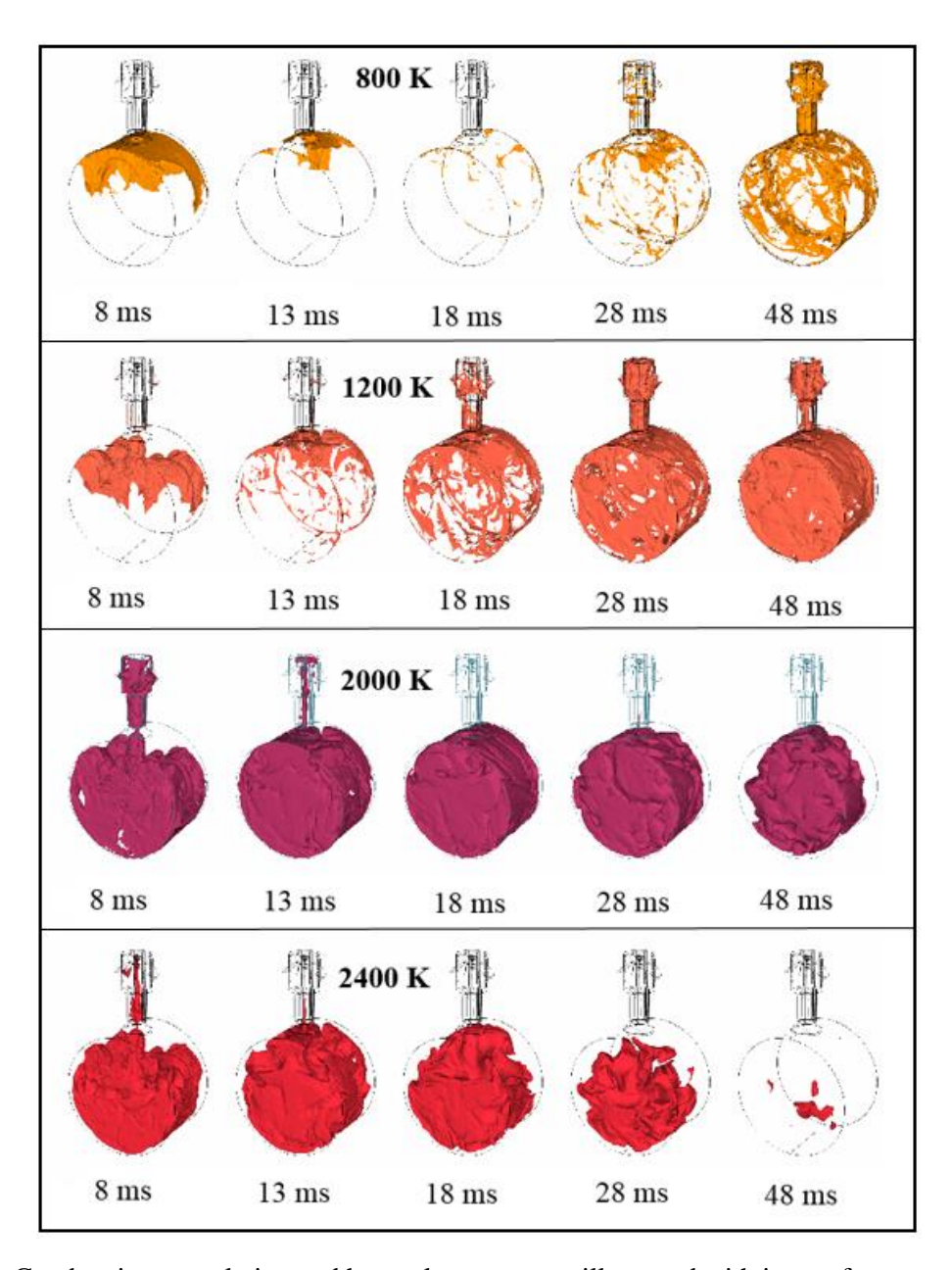


Figure 9-7- Combustion completion and heat release process illustrated with iso-surface contours, d=2.0 mm, λ =1.25.

In Figure 9-8 the OH mass fraction contours for the lean case of λ =1.25 are presented for various nozzle geometries. Electrically excited OH radicals emit visible light at high temperatures. This makes it possible to distinguish between the reacting and non-reacting regions. As mentioned earlier, the visible light in the experimental images is an accumulation of infinite number of planar slices through the main chamber. In the simulations, the contours are shown only for one plane, which passes through the nozzle. The mass of electrically exited OH radicals (OH*) cannot be calculated in the simulations. Instead, the overall experimentally measured OH mass fraction contours are shown, which are an indicator of the reacting region and flame front.

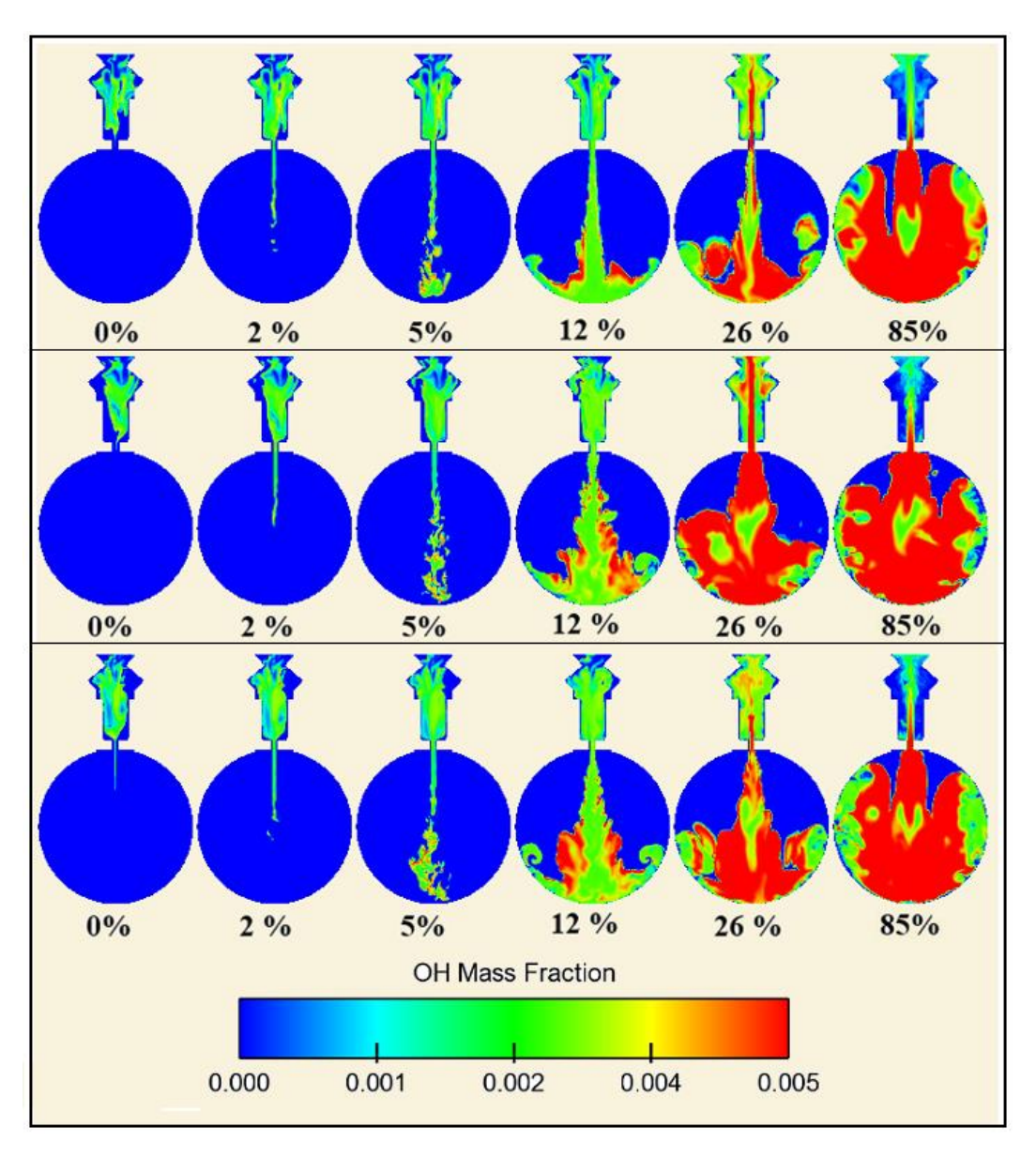


Figure 9-8- OH mass fraction contours for d=2.0, 2.5 and 3.0 mm, from top to the bottom, respectively, at λ =1.25.

9-2 Chapter Summary

A set of 3-D transient CFD simulations of TJI combustion were performed using an LES approach with a Smagorinsky sub-grid scale model. Pressure traces and temperature contours from the modeling were compared with the experimental measurements and chemiluminescence images. The orifice diameter alters the initial penetration speed and the flame propagation rate, which leads

to various levels of combustion enhancement at different stages of combustion in the main chamber. In order to have fast flame propagation and stable combustion in the main chamber, the orifice size should be considered along with the mixture stoichiometry. In general, with a larger orifice the jet has a lower penetration speed and a higher initial flame propagation speed and combustion rate. With a smaller orifice there is increased flow restriction that results in a narrow initial jet with a higher penetration speed which leads to an increase in turbulent mixing and consequently faster combustion in the later stages of ignition.

A comparison of the experimental pressure traces and modeling results showed that the numerical simulation with LES is capable of improving the accuracy of the prediction of compression pressure rise and combustion burn rate. However, the numerical peak pressure is higher than the measured values, Chapter 8. This discrepancy can be attributed to a number of factors, such as inaccuracies in the chemical kinetic mechanism especially at high pressures, the removed crevice volumes in the simulation geometry, and numerical errors. In this thesis, for the first time, a CONVERGE LES approach was used in place of a RANS approach which led to a reduction in numerical errors and allowed the evaluation of additional details of the combustion flow field. The numerical iso-surface temperature contours (1200, 800, 2000, and, 2400 K) were obtained which enabled 3-D views of the flame propagation, the jet discharge, ignition and extinction events, and the heat release process. Once the pressure inside the main chamber reaches its maximum, the system starts to cool down and the pressure decreases due to heat losses. Results showed that the rate of heat release is higher at the chamber wall boundaries. Approximately 40 ms after ignition, the temperature at the wall boundaries is 1200 K while the main chamber core region has a temperature as high as 2000 K. The modeling results enabled increased understanding of the details of the heat release process and the regeneration of mid-range temperature isosurfaces. These details which cannot be visualized in the current experimental apparatus.

Chapter 10 Summary and Concluding Remarks

This dissertation presents theoretical and modeling studies of a TJI system using various turbulent models and correlations as well as experimental tests performed with an optically accessible rapid compression machine. Although conclusions regarding the modeling and theoretical results have been presented as part of each individual chapter, remarks addressing the general aspects of this research project are addressed and presented as answers to the research questions initially presented in Chapter 1.

1- What are the orifice diameter and equivalence ratio effects on the turbulent jet structure as it enters into the main chamber and how do they influence the flame propagation, burning rate, entrainment rate, and hence combustion enhancement?

As part of this thesis, a series of tests were carried out to determine the influences of orifice diameter, d, and mixture composition, ϕ , on the jet inlet and tip speed in a turbulent jet ignition system and the rate of flame spread in the main combustion chamber. Experiments performed in the RCM revealed two direct relationships between the orifice sizes and equivalence ratios tested for this work: (1) reducing the orifice exit area below a threshold (0.6, where the threshold was assumed to be the ratio of the nozzle area to the prechamber volume) produced a decrease in the hot jet penetration speed; (2) decreasing the mixture equivalence ratio increased the hot jet penetration speed with the exception of the $3.0 \, mm$ orifice diameter case.

In Chapter 7 a series of numerical simulations were carried out to study the discharge of a hot reacting jet using the Converge code. Results were compared with the experimental measurements and the theoretical correlations discussed in Chapter 6. A correlation based on first physical principles was introduced. CFD modeling of a methane fueled TJI system was used to provide

further information on the flow field consisting of velocity, density gradient, and turbulent intensity inside the main chamber and prechamber.

From the numerical results, it was concluded that the use of a larger nozzle is more desirable as it improves jet penetration. On the other hand, a smaller orifice magnifies turbulent intensity in the main chamber and consequently is more efficient at later stages of combustion.

It was shown that as the mixture became leaner, the ignition delay time increased (0.35 ms from λ =1.0 to 1.25 and 3.5 ms from λ =1.0 to 1.5) while the burn rate and maximum peak combustion pressure decreased. In addition, by changing λ from 1.0 to 1.25 and 1.5, burn duration was increased 37% and 90%, respectively (0-100 burn durations were approximately 8.5, 11.5 and 16.5 ms for λ =1.0, 1.25 and 1.5, respectively). Considering the d=2.0 mm orifice as a reference, an increase of orifice diameter to 2.5 and 3.0 resulted in burn duration increases of approximately 4.5% and 9.5%, respectively.

A time series of the velocity in the main chamber (at specific monitor points) and the nozzle throat were recorded during the run time. The flow velocity in the nozzle throat and in the vicinity of orifice exit was highest for the smaller orifice diameter, however, near the chamber wall the large orifice jet was fastest. In addition, the maximum flow velocities occurred after the onset of the jet discharge leading to the conclusion that the flow inside the main chamber does not necessarily have its highest velocity at the moment when the hot jet becomes visible. As a result, a distinction should be made between the flow velocity and hot jet penetration speed.

2- How is the turbulent jet described based on the flow characteristic parameters such as the Reynolds number and Mach number?

The nozzle exit velocity estimated by various correlations and simulations was in the range of 100 to 300 m/s for all cases resulting in a Reynolds number of $3-6\times10^4$ ($Re=\rho vd/\mu$ where d is the nozzle diameter) and Mach number of approximately 0.3.

3- How many flow regions does the jet experience as it travels toward the main chamber end wall and does it become fully developed?

As the hot jet evolves downstream of the orifice exit, it remains in the near and intermediate field x/d regimes, and does not evolve into the far field stage $x/d \ge 25$. For the range of Reynolds numbers calculated, $\sim 20,000$ and higher, the round jets are all turbulent. More details are provided in Chapter 6.

4- Does any correlation exist in the literature to estimate the nozzle exit velocity since the velocity measurement is not viable in the main chamber?

Due to the non-viability of velocity measurements during combustion at high pressure (~50 bar) in the current RCM set-up, existing correlations have been utilized to estimate the orifice exit velocity. Data has been presented for the hot jet velocity at the nozzle exit, predicted by the similarity, inverse ratio and penetration correlations factors that remain to be investigated.

Although the correlations used have not precisely estimated the orifice exit velocity, they have provided acceptable results to calculate the Reynolds and Mach number of the hot jet. They show, unequivocally, that the TJI jet and flow is turbulent. In addition, with the conditions considered and the orifice sizes used, the nozzle will most likely not be choked and, hence, no shock or expansion waves are expected.

Finally, it was suggested that as useful as previous literature correlations may be, the fact that the TJI jets impinge on an opposite wall while also demonstrating strong lateral entrainment and spread during injection requires new and improved analyses and correlations.

5- How accurately does the numerical modeling predict the combustion process and what is the difference between the reduced and full chemical kinetic mechanisms?

3-dimensional transient CFD simulations of cases with variable orifice diameter (Chapters 6 and 7) of a methane fueled TJI system in a rapid compression machine were performed. CFD pressure curves showed close compatibility with experiments in compression stage, however, the burn rate, burn duration and maximum pressure predicted numerically were not in complete agreement with experiments.

The pressure traces of four comprehensive mechanisms and a reduced mechanism were compared with the experimental pressure data. Results showed that none of the mechanisms are in complete agreement, however they are in reasonably good agreement with the experiment in terms of burn rate, peak pressure and ignition delay prediction. Consequently, the reduced mechanism was used for the simulations.

6- What are the values of turbulent intensity, density, temperature and important intermediate species concentration such as OH and CH, in the main and prechamber?

Simulations confirmed the creation of high turbulent kinetic energy region in the main chamber as a result of cold jet discharge, facilitating the increase of mixing and improve combustion, as well as creation of a non-uniform density and turbulent intensity distribution. Maximum turbulent kinetic energy and OH mass fraction in the domain were approximately $200 \text{ m}^2/\text{s}^2$ and 4×10^{-4} ,

respectively. In addition, nozzle velocity and density that have been recorded at the monitor points were used to calculate the mass flow rate. More details are provided in Chapter 7.

To compare the temperature contours with the experimental images, the numerical pressure traces were scaled to match the start of combustion and the peak pressure with the corresponding values from the experiment to produce an accurate time basis for comparison. Modeling contours showed that the maximum temperature in the domain varies based on the mixture condition and it was as high as 2600 K for the stoichiometric case. In this thesis for the first time 3-D transient CFD simulations of TJI combustion were performed using an LES approach with a Smagorinsky subgrid scale model. Pressure traces and temperature contours from the modeling were compared to the experimental measurements and chemiluminescence images and were provided in Chapter 9. It was found that to have fast flame propagation and stable combustion in the main chamber, the effect of orifice size should be considered along with the mixture stoichiometry.

The numerical iso-surface temperature contours (1200, 800, 2000, and, 2400 K) were obtained which enabled 3-D views of the flame propagation, the jet discharge, ignition and extinction events, and the heat release process. Once the pressure inside the main chamber reaches the maximum, the system starts to cool down and the pressure decreases due to heat loss to the environment. Results showed that the rate of heat release is higher at the chamber wall boundaries. Approximately 40 ms after ignition, the temperature at the wall boundaries was estimated to be 1200 K while the main chamber core region had a temperature as high as 2000 K. The modeling results enabled increased understanding of the details of the heat release process and the regeneration of mid-range temperature iso-surfaces, details which cannot be visualized through the experiments.

7- What is the impact of auxiliary fueling the prechamber on the burn rate and the lean/dilute limit extension of the RCM?

To highlight the research achievements in addressing the dilution effect, experiments and simulation of the combustion process in an auxiliary fueled TJI system with N₂ dilution were performed.

Both the experimental and numerical limit for N₂ dilution were found to be approximately 35%. In addition, increased dilution showed a direct relationship with decelerated flame propagation and combustion rate. These results were revealed through the contours of OH radical mass fractions and the turbulent kinetic energy. Experimental results show that the peak pressure decreased by approximately 24% and 27% for 35% and 40% N₂ dilution, respectively. In addition, considering the stoichiometric case as the reference, ignition delay time for 35% and 40% N₂ dilution cases were 12 ms and 26 ms, respectively while the 4% auxiliary injection reduced the ignition delay to 2.5 ms. The 0-100% burn durations recorded during the experiments had an increasing trend of 5.3 ms, 10.3 ms and 25.5 ms for 0%, 35%, 40% N₂ dilution cases, while the 4% auxiliary injection case reduced the burn duration to 6.9 ms which was only 1.6 ms longer than the stoichiometric case. Results confirmed the idea of combustion enhancement of diluted mixtures by the prechamber auxiliary injection.

In addition, the modeling pressure traces and contours compared with measured pressure data and optical images captured by a high speed camera during experimental RCM tests. Numerical results gave insight into the combustion process inside the prechamber and provide qualitative data such as the turbulent kinetic energy which was impossible to measure during the experiments. In addition, features such as the initial cool prechamber jet as well as the backflow of unburned mixture from the main chamber into the prechamber at the later stages of combustion, which

cannot be observed experimentally, were revealed. This phenomenon demonstrates the pressure imbalance through the orifices that leads to the unsteady jet velocity through the orifice and into the main chamber.

10-1 Recommendations for Future Work

During this research, a range of TJI operating points with and without auxiliary injection and with and without N_2 dilution were performed in which the focus was mainly on the theoretical and physical study of the combustion process and flame propagation in the main chamber. In addition, the flow field characteristics and jet discharge process were investigated, all leading to a thorough understanding of the TJI process and its improvement. Over the course of completion of this work, a number of possible future areas were emerged that could potentially lead to future application of TJI.

- ➤ In the TJI experiments, a high speed color camera was used to perform combustion visualization, however, another useful method is the use of the Schlieren technique to visualize the density gradients and jet dispersion angle. Quantitative analysis Schlieren images could support the penetration speed correlation concept and show side views of the jet ignition and combustion in the main chamber.
- ➤ The possibility of using probes to measure flow velocity and thermocouples in both the pre and main chambers could be considered to enable further development of a robust TJI system prior to its application in vehicles.
- ➤ In this thesis, methane was used as the main and prechamber fuel and also in auxiliary injection in the prechamber. It is anticipated that the use of a heavier fuel in both the pre

- and main chambers or fuel variation between the chambers would greatly affect the combustion performance and the turbulent flow field due to the change in density gradients.
- For the LES simulation portion of this thesis, a Smagorinsky sub grid scale model was used to simulate the turbulent flow field of the jet. The implementation of more sophisticated models such as dynamic models [143, 144] is suggested for future simulations. In addition, simulation of liquid spray and use of spray models is suggested.

APPENDICES

Appendix A Uncertainty Analysis

To estimate the uncertainty of the desired/intermediate variables based on the contribution of the uncertainty of each parameter, a sensitivity analysis is necessary. The sensitivity analysis is performed for two parts, first the uncertainty of the temperature and ambient density at TDC is calculated, and thereafter the uncertainty of each correlation in the exit velocity estimation is evaluated.

Eq. 6-13 is used to write the initial temperature, initial pressure and compressed pressure as a mean value plus an uncertain quantity, or error, as $(T_{BDC} = \overline{T_{BDC}} + \delta T_{BDC})$, $(P_{BDC} = \overline{P_{BDC}} + \delta P_{BDC})$ and $(P_{TDC} = \overline{P_{TDC}} + \delta P_{TDC})$, respectively. Substituting these expressions into the polytropic compression process equation;

$$T_{TDC} = T_{BDC} \left(\frac{P_{TDC}}{P_{BDC}}\right)^{(1-1/\gamma)},$$
 A 1

results in the simplified form

$$\frac{\delta T_{TDC}}{\overline{T_{TDC}}} = \left(1 - \frac{1}{\gamma}\right)\varepsilon + \frac{\delta T_{BDC}}{\overline{T_{BDC}}},$$
 A 2

where;

$$\varepsilon = \frac{\delta P_{TDC}}{P_{TDC}} - \frac{\delta P_{BDC}}{P_{BDC}} - \frac{\delta P_{TDC}}{P_{TDC}} \cdot \frac{\delta P_{BDC}}{P_{BDC}}.$$
 A 3

The last term on the right hand side of Eq. A3 is neglected and larger errors are retained in the calculations. Knowing the errors, $(\frac{\delta T_{BDC}}{T_{BDC}} < 1.5\%)$, $(\frac{\delta P_{BDC}}{P_{BDC}} < 0.7\%)$ and $(\frac{\delta P_{TDC}}{P_{TDC}} < 7\%)$, the compressed temperature error is estimated as 3.5%. Equivalently, using the ideal gas equation of state,

$$\rho_a = \frac{P}{\frac{R_u}{MW_{mix}}T},$$
 A 4

the uncertainty of the density of main chamber mixture at TDC, $(\frac{\delta \rho_a}{\overline{\rho_a}})$ become

$$\frac{\delta \rho_a}{\overline{\rho_a}} = \frac{\delta P_{TDC}}{\overline{P_{TDC}}} - \frac{\delta T_{TDC}}{\overline{T_{TDC}}} - \frac{\delta P_{TDC}}{\overline{P_{TDC}}} \cdot \frac{\delta T_{TDC}}{\overline{T_{TDC}}}.$$
 A 5

The calculated value is less than 6.5 % for all cases presented in Chapter 6.

Since the experimental measurement of the jet temperature is unfeasible, it is assumed that the jet temperature for the gases entering the main chamber is equal to the adiabatic flame temperature. A considerable error ($\frac{\delta T_{adiabatic}}{T_{adiabatic}} = 10\%$) is therefore presumed for the jet temperature. Again, the ideal gas equation of state and the error expression (equations A4, A5) are used and a noticeable error in jet density, (~10%) (varying due to the air to fuel ratio of the mixture) is calculated.

Substituting all variables of Eq. 6-7 in the form of Eq. 6-13, the uncertainty calculation of the nozzle exit velocity based on the similarity analysis results in the following expression:

$$\frac{\delta v_e}{\overline{v_e}} = 2\frac{\delta x}{\bar{x}} + \frac{\delta k}{\bar{k}} + 1/2(\frac{\delta \rho_a}{\overline{\rho_a}} - \frac{\delta \rho_e}{\overline{\rho_e}}),$$
 A 6

where $\frac{\delta x}{\bar{x}}$ is the error in the penetration length measurements (<2.5%) and $\frac{\delta k}{\bar{k}}$ is the error in the constant coefficient of the correlation and is assumed to be less than 0.5%. Also, $\frac{\delta \rho_a}{\bar{\rho}_a}$ and $\frac{\delta \rho_e}{\bar{\rho}_e}$ are the errors of the ambient and jet densities, 3.4% and <10%, respectively (it should be noted that $\frac{\delta \rho_e}{\bar{\rho}_e}$ depends on the mixture condition). Exit velocity estimation errors, $(\frac{\delta v_e}{v_e})$, obtained from Eq. A6 are 11.4%, 7% and 12.5% for 2 mm, 2.5 mm and 3 mm nozzles, respectively.

Similarly, an uncertainty calculation for the non-vaporizing spray penetration correlation results in the following expression;

$$\frac{\delta v_e}{\overline{v_e}} = \frac{\epsilon 5}{f(\bar{x})},$$
 A 7

where

$$f(\bar{x}) = \frac{\bar{x}}{2} + \frac{\bar{x}}{4} \sqrt{1 + 16(\frac{\bar{x}}{\bar{x}^{+}})^{2}} + \frac{\bar{x}^{+}}{16} \ln(A),$$
 A 8

and

$$\epsilon_5 = \left\{ \frac{\bar{x}}{2} \frac{\delta x}{\bar{x}} + \frac{\bar{x}}{4} \sqrt{1 + 16(\frac{\bar{x}}{\bar{x}^+})^2} \cdot \epsilon_4 + \frac{\bar{x}^+}{16} \left[\frac{\delta x^+}{\bar{x}^+} \ln(A) + \frac{\epsilon_3}{A} + \frac{\delta x^+}{\bar{x}^+} \cdot \frac{\epsilon_3}{A} \right] \right\}.$$
 A 9

Intermediate parameters are defined as follows:

$$A = \left\{ 4\frac{\bar{x}}{x^{+}} + \sqrt{1 + 16(\frac{\bar{x}}{x^{+}})^{2}} \right\},$$
 A 10

$$\epsilon_4 = \left\{ \frac{\delta x}{\bar{x}} + \epsilon_2 + \frac{\delta x}{\bar{x}} \cdot \epsilon_2 \right\},\tag{A 11}$$

$$\epsilon_3 = \left\{ 4 \frac{\bar{x}}{\bar{x}^+} + \epsilon_1 + \sqrt{1 + 16(\frac{\bar{x}}{\bar{x}^+})^2} \cdot \epsilon_2 \right\},\tag{A 12}$$

$$\epsilon_2 = \left\{ \frac{\epsilon_1}{1 + 1/16(\frac{\overline{x}}{r^+})^2} \right\},\tag{A 13}$$

$$\epsilon_1 = \left\{ \frac{\delta x}{\bar{x}} - \frac{\delta x^+}{\bar{x}^+} - \frac{\delta x}{\bar{x}} \cdot \frac{\delta x^+}{\bar{x}^+} \right\}.$$
 A 14

Thus, $\frac{\delta x}{\bar{x}}$ is the error of the penetration length measurement. Since x^+ is a function of the density ratio and the equivalence diameter, $\frac{\delta x^+}{\bar{x}^+}$ is a function of errors in the densities of the jet and ambient fluid and the equivalent orifice diameter $(\frac{\delta d_{eq}}{\overline{d_{eq}}})$. Hence

$$\frac{\delta x^{+}}{\overline{x^{+}}} = \frac{\delta d_{eq}}{\overline{d_{eq}}} + \aleph_{1} + \frac{\delta d_{eq}}{\overline{d_{eq}}} \cdot \aleph_{1},$$
A 15

and

$$\aleph_1 = \frac{1}{2} \frac{\delta \rho_e}{\overline{\rho_e}} - \frac{\delta \rho_a}{\overline{\rho_a}} - \frac{1}{4} \frac{\delta \rho_e}{\overline{\rho_e}} \cdot \frac{\delta \rho_a}{\overline{\rho_a}}.$$
 A 16

Therefore, exit velocity estimation errors, $(\frac{\delta v_e}{\overline{v_e}})$, obtained from Eq. A3 are less than 4% for all nozzle diameters.

Appendix B Laminar Flame Speed Calculation

One-D laminar Flame Speed (LFS) calculations are performed and results for various mechanisms are shown in Figure Figure B-1. The 1D LFS solver is based on Newton's method and for the cases shown here, air-fuel ratio and temperature are equal to 1.25 and 750 K respectively. LFS calculated for all mechanisms is within the range of 0.3 to 0.7 m/s and the variations are small. The reduced mechanism follows the trend of NUI mechanism (the original mechanism before reduction process) very closely. In addition, results for the lower limit of pressure (15 bar) are in agreement with [145] in which two experimental techniques, Bunsen burner method and an expanding spherical flame method were used to study the laminar flame speeds for methane based mixtures at elevated pressures.

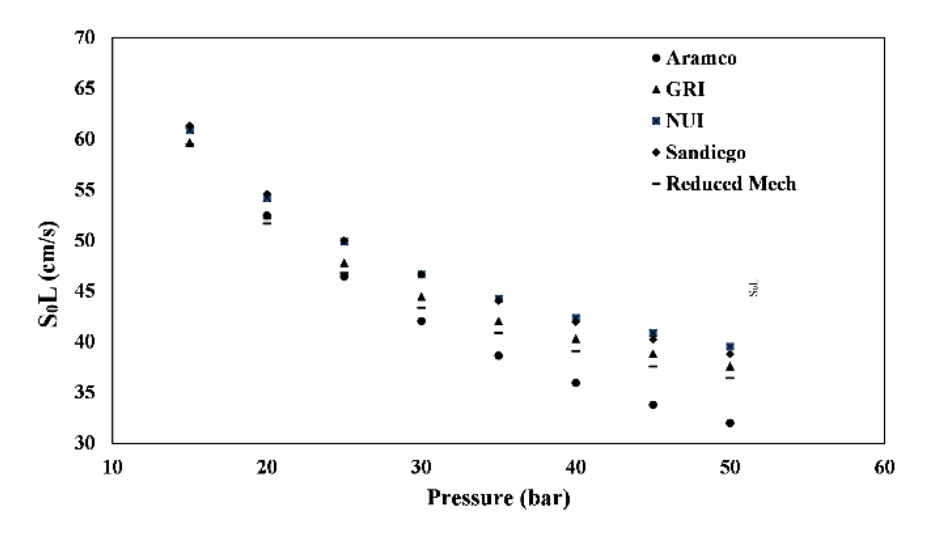


Figure B-1- Methane Laminar Flame Speed at λ =1.25 and compressed temperature of 750 K.

Appendix C Integrated Heat Release

In Converge, three common methods exist to specify the spark energy sources for engine applications. Adding the spark energy sources directly, applying specified measurements or simulation data for heat release rate and using the measured cylinder pressure trace for the entire engine cycle. In the current research, the first option is used based on the experimental energy of the spark. Throughout the simulation, the apparent heat release rate will be calculated as shown in Figure Figure C-1. Among different wall models, law of the wall is chosen due to the constant temperature of boundaries and the wall temperature was specified as 353 K, to correspond with RCM walls' temperature.

Since the engine cycle and various thermodynamic stages (i.e. intake, exhaust, compression and combustion) of an engine are different from the corresponding stages that can be seen in the RCM, the 0-10 % and 10-90 % burn rates in the RCM are provided instead of the heat release rate, see section 8-1.

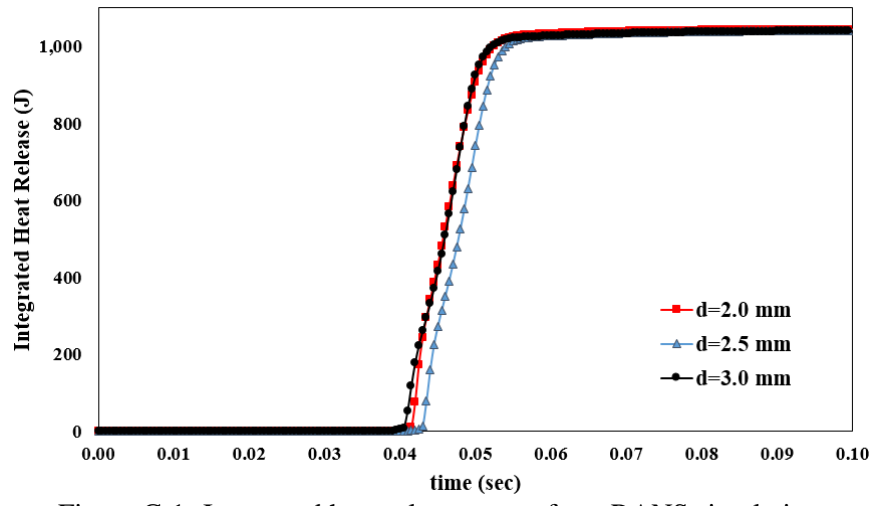


Figure C-1- Integrated heat release curve from RANS simulation.

Appendix D Crevice Volume Effect

To estimate the approximate amount of unburned mass that is trapped in the crevice volume of the TJI system and the associated pressure rise due to this unburned mass, a preliminary calculation is performed. The pressure, temperature, volume and total mass at TDC are known (temperature is calculated with the polytropic compression assumption). The crevice volume is assumed to vary from 1% of the clearance volume to up to 8%. Considering a homogeneous mixture in the domain, the mass trapped in the crevice volume is calculated as follows;

$$m_{cr} = m_{total} \left(\frac{T_{TDC}}{T_{avg}}\right) \left(\frac{V_{cr}}{V_{TDC}}\right),$$
 D 1

where T_{avg} is the average of the mixture temperature at TDC and the wall temperature. The unburned mass for different crevice volume assumptions is listed in Table D 1.

Assuming a linear trend between TDC and the peak pressure, the effect of unburned mass on pressure rise is calculated and listed in Table D 1.

Table D 1- Unburned mass and pressure rise results.

T_{wall}	T_{comp}	T_{avg}	P_{comp}	V_{TDC} (m ³)	$\%(V_{cr}/V_{TDC})$	m_{total}	$\%(m_{unburned}/m_{total})$	P_rise	P_{rise}
(K)	(K)	(K)	(bar)			(kg)		(bar)	
					1		1.38	0.67	2.09
353	755	554	16	6.43×10^{-5}	2	4.68×	2.76	1.36	4.25
					4	10^{-4}	5.51	2.8	8.75
					8		11	6	18.6

It is noteworthy to mention that if the unburned mixture trapped in the crevices is assumed to be at the wall temperature, the % ($m_{unburned}/m_{total}$) is in the range of 2.16 to 17.3% and the corresponding pressure rise is in the range of 1.06 to 10 bar. On the other hand, if the unburned mixture trapped in the crevices is assumed to be at the TDC temperature, the % ($m_{unburned}/m_{total}$) is

in the range of 1.01 to 8.09 % and the corresponding pressure rise is in the range of 0.49 to 4.22 bar.

Based on these calculations, the crevice volume contributes an error in the range of 20 to 40% (considering the average temperature of the unburned mixture) in the RANS simulation peak pressure prediction compared to the experimental peak pressure. It should be noted that this error is a function of the mixture stoichiometry condition (λ is 1.25 in these calculations), unburned gas temperature and the assumed percentage of crevice volume. Based on the above error estimation calculations, the crevice volume error is considered a significant source of error in the numerical pressure discrepancies.

BIBLIOGRAPHY

BIBLIOGRAPHY

- [1]. E. Toulson, H. J. Schock, and W. P. Attard, A review of pre-chamber initiated jet ignition combustion systems, SAE International doi: 10.4271/2010-01-2263. (2010).
- [2]. J. Meisl, R. Koch, R. Kneer, and S. Wittig, Study of nox emission characteristics in pressurized staged combustor concepts. Symposium (International) on Combustion, 25(1) (1994). 1043-1049.
- [3]. M. Christensen, A. Hultqvist, and B. Johansson, Demonstrating the multi fuel capability of a homogeneous charge compression ignition engine with variable compression ratio, SAE International doi: 10.4271/1999-01-3679. (1999).
- [4]. E. J. Tully and J. B. Heywood, Lean-burn characteristics of a gasoline engine enriched with hydrogen plasmatron fuel reformer, SAE International doi: 10.4271/2003-01-0630. (2003).
- [5]. R. Dibble, M. Au, J. Girard, S. M. Aceves, D. L. Flowers, J. Martinez-Frias, and J. R. Smith, Current research in hcci combustion at uc berkeley and llnl, SAE International doi: 10.4271/2001-01-2511. (2001).
- [6]. R. M. Heck and R. J. Frrauto, *Auto exhaust catalysis*, in *Encyclopedia of catalysis*. 2002, John Wiley & Sons, Inc.
- [7]. M. D. Amiridis, T. Zhang, and R. J. Farrauto, Selective catalytic reduction of nitric oxide by hydrocarbons. Applied Catalysis B: Environmental, 10(1–3) (1996). 203-227.
- [8]. A. Fritz and V. Pitchon, The current state of research on automotive lean nox catalysis. Applied Catalysis B: Environmental, 13(1) (1997). 1-25.
- [9]. J. D. Dale and A. K. Oppenheim, Enhanced ignition for I. C. Engines with premixed gases, SAE International doi: 10.4271/810146. (1981).
- [10]. R. M. Modien, M. D. Checkel, and J. D. Dale, The effect of enhanced ignition systems on early flame development in quiescent and turbulent conditions, SAE International doi: 10.4271/910564. (1991).
- [11]. J. D. Dale, M. D. Checkel, and P. R. Smy, Application of high energy ignition systems to engines. Progress in Energy and Combustion Science, 23(5–6) (1997). 379-398.
- [12]. B. Wolk, A. DeFilippo, J. Y. Chen, R. Dibble, A. Nishiyama, and Y. Ikeda, Enhancement of flame development by microwave-assisted spark ignition in constant volume combustion chamber. Combustion and Flame, 160(7) (2013). 1225-1234.
- [13]. A. Starikovskiy and N. Aleksandrov, Plasma-assisted ignition and combustion. Progress in Energy and Combustion Science, 39(1) (2013). 61-110.
- [14]. H. Do, S. k. Im, M. A. Cappelli, and M. G. Mungal, Plasma assisted flame ignition of supersonic flows over a flat wall. Combustion and Flame, 157(12) (2010). 2298-2305.
- [15]. P. G. Aleiferis, Y. Hardalupas, A. M. K. P. Taylor, K. Ishii, and Y. Urata, Flame chemiluminescence studies of cyclic combustion variations and air-to-fuel ratio of the

- reacting mixture in a lean-burn stratified-charge spark-ignition engine. Combustion and Flame, 136(1–2) (2004). 72-90.
- [16]. E. Murase and K. Hanada, Enhancement of combustion by injection of radicals, SAE International doi: 10.4271/2000-01-0194. (2000).
- [17]. E. Murase, S. Ono, K. Hanada, and A. K. Oppenheim, Pulsed combustion jet ignition in lean mixtures, SAE International doi: 10.4271/942048. (1994).
- [18]. E. Murase, S. Ono, K. Hanada, J. H. Yun, and A. K. Oppenheim, Performance of pulsed combustion jet at high pressures and temperatures. JSAE Review, 17(3) (1996). 245-250.
- [19]. G. Gentz, B. Thelen, M. Gholamisheeri, P. Litke, A. Brown, J. Hoke, and E. Toulson, A study of the influence of orifice diameter on a turbulent jet ignition system through combustion visualization and performance characterization in a rapid compression machine. Applied Thermal Engineering, 81 (2015). 399-411.
- [20]. W. P. Attard, N. Fraser, P. Parsons, and E. Toulson, A turbulent jet ignition pre-chamber combustion system for large fuel economy improvements in a modern vehicle powertrain. SAE Int. J. Engines, 3(2) (2010). 20-37.
- [21]. W. P. Attard, E. Toulson, A. Huisjen, X. Chen, G. Zhu, and H. Schock, Spark ignition and pre-chamber turbulent jet ignition combustion visualization, SAE International doi: 10.4271/2012-01-0823. (2012).
- [22]. G. Gentz, B. Thelen, P. Litke, J. Hoke, and E. Toulson, Combustion visualization, performance, and CFD modeling of a pre-chamber turbulent jet ignition system in a rapid compression machine. SAE Int. J. Engines, 8(2) (2015). 538-546.
- [23]. M. Gholamisheeri, B. Thelen, G. Gentz, and E. Toulson, CFD modeling of an auxiliary fueled turbulent jet ignition system in a rapid compression machine, SAE International doi: 10.4271/2016-01-0599. (2016).
- [24]. B. C. Thelen, G. Gentz, and E. Toulson, Computational study of a turbulent jet ignition system for lean burn operation in a rapid compression machine, SAE International doi: 10.4271/2015-01-0396. (2015).
- [25]. E. Toulson, A. Huisjen, X. Chen, C. Squibb, G. Zhu, H. Schock, and W. P. Attard, Visualization of propane and natural gas spark ignition and turbulent jet ignition combustion. SAE Int. J. Engines, 5(4) (2012). 1821-1835.
- [26]. W. P. Attard and H. Blaxill, A single fuel pre-chamber jet ignition powertrain achieving high load, high efficiency and near zero nox emissions. SAE Int. J. Engines, 5(3) (2011). 734-746.
- [27]. W. P. Attard and H. Blaxill, A lean burn gasoline fueled pre-chamber jet ignition combustion system achieving high efficiency and low nox at part load, SAE International doi: 10.4271/2012-01-1146. (2012).
- [28]. W. P. Attard and H. Blaxill, A gasoline fueled pre-chamber jet ignition combustion system at unthrottled conditions. SAE Int. J. Engines, 5(2) (2012). 315-329.

- [29]. W. P. Attard, H. Blaxill, E. K. Anderson, and P. Litke, Knock limit extension with a gasoline fueled pre-chamber jet igniter in a modern vehicle powertrain. SAE Int. J. Engines, 5(3) (2012). 1201-1215.
- [30]. W. P. Attard, J. Kohn, and P. Parsons, Ignition energy development for a spark initiated combustion system capable of high load, high efficiency and near zero nox emissions. SAE Int. J. Engines, 3(2) (2010). 481-496.
- [31]. W. P. Attard and P. Parsons, Flame kernel development for a spark initiated pre-chamber combustion system capable of high load, high efficiency and near zero nox emissions. SAE Int. J. Engines, 3(2) (2010). 408-427.
- [32]. W. P. Attard and P. Parsons, A normally aspirated spark initiated combustion system capable of high load, high efficiency and near zero nox emissions in a modern vehicle powertrain. SAE Int. J. Engines, 3(2) (2010). 269-287.
- [33]. J. Warnatz., U. Maas., and R.W. Dibble, Combustion: Physical and chemical fundamentals, modeling and simulation, experiments, pollutant formation. Fourth edition. Berlin; New York: Springer, 2006.
- [34]. R. Maly, Spark ignition: Its physics and effect on the internal combustion engine, in Fuel economy: In road vehicles powered by spark ignition engines, J.C. Hilliard and G.S. Springer, Editors. 1984, Springer US: Boston, MA. 91-148.
- [35]. J. Xu, F. Behrendt, and J. Warnatz, 2d-lif investigation of early stages of flame kernel development after spark ignition. Proc. COMODIA, JSME, Yokohama, (1994). 69.
- [36]. N. Peters, Four lectures on turbulent combustion. (1997).
- [37]. H. C. Watson, Internal combustion engine ignition device: United States, No. 5611307 doi. (1997).
- [38]. H. C. Watson, International patent. Application, pct/au92/00552, doi. (1992).
- [39]. C. K. Law, Combustion physics. Cambridge university press, 2010.
- [40]. R. Borghi and F. Anselmet, Turbulent multiphase flows with heat and mass transfer (1). Somerset, US: Wiley-ISTE, 2013.
- [41]. R. Borghi, Turbulent combustion modelling. Progress in Energy and Combustion Science, 14(4) (1988). 245-292.
- [42]. N. Peters, Laminar flamelet concepts in turbulent combustion. Symposium (International) on Combustion, 21(1) (1988). 1231-1250.
- [43]. S. M. Candel and T. J. Poinsot, Flame stretch and the balance equation for the flame area. Combustion Science and Technology, 70(1-3) (1990). 1-15.
- [44]. E. Toulson, Applying alternative fuels in place of hydrogen to the jet ignition process, doi. (2008).
- [45]. H. S. Johnston, Atmospheric ozone. Annual Review of Physical Chemistry, 43(1) (1992). 1-31.

- [46]. C. T. Bowman, Control of combustion-generated nitrogen oxide emissions: Technology driven by regulation. Symposium (International) on Combustion, 24(1) (1992). 859-878.
- [47]. E. Jackson and A. Granik, *The oxidation of nitrogen in combustion and explosions*, in *Selected works of yakov borisovich zeldovich, volume i*, Y.B. Zeldovich, G.I. Barenblatt, and R.A. Sunyaev, Editors. 1992, Princeton University Press. 364-403.
- [48]. C. P. Fenimore, Studies of fuel-nitrogen species in rich flame gases. Symposium (International) on Combustion, 17(1) (1979). 661-670.
- [49]. P. C. Malte and D. T. Pratt, Measurement of atomic oxygen and nitrogen oxides in jet-stirred combustion. Symposium (International) on Combustion, 15(1) (1975). 1061-1070.
- [50]. M. Shelef and R. W. McCabe, Twenty-five years after introduction of automotive catalysts: What next? Catalysis Today, 62(1) (2000). 35-50.
- [51]. S. Pischinger, T. Körfer, A. Wiartalla, J. Schnitzler, D. Tomazic, and M. Tatur, Combined particulate matter and nox aftertreatment systems for stringent emission standards, SAE International doi: 10.4271/2007-01-1128. (2007).
- [52]. C. L. DiMaggio, G. B. Fisher, K. M. Rahmoeller, and M. Sellnau, Dual scr aftertreatment for lean nox reduction. SAE Int. J. Fuels Lubr., 2(1) (2009). 66-77.
- [53]. M. C. Turkish, 3 valve stratified charge engines: Evolvement, analysis and progression, SAE International doi: 10.4271/741163. (1974).
- [54]. C. E. Summers, Internal combustion engine, in *United States,No. 1568638*, N. United States, Editor: United States doi. (1926).
- [55]. M. Mallory, Internal combustion engine: United states, doi. (1938).
- [56]. L. A. Gussak, V. P. Karpov, and Y. V. Tikhonov, The application of lag-process in prechamber engines, SAE International doi: 10.4271/790692. (1979).
- [57]. L. A. Gussak, M. C. Turkish, and D. C. Siegla, High chemical activity of incomplete combustion products and a method of prechamber torch ignition for avalanche activation of combustion in internal combustion engines, SAE International doi: 10.4271/750890. (1975).
- [58]. A. K. Oppenheim, Combustion in piston engines, technology, evolution, diagnoses and control. Springer, 2004.
- [59]. J. A. Maxson, D. M. Hensinger, K. Hom, and A. K. Oppenheim, Performance of multiple stream pulsed jet combustion systems, SAE International doi: 10.4271/910565. (1991).
- [60]. J. A. Maxson and A. K. Oppenheim, Pulsed jet combustion—key to a refinement of the stratified charge concept. Symposium (International) on Combustion, 23(1) (1991). 1041-1046.
- [61]. D. M. Hensinger, J. A. Maxson, K. Hom, and A. K. Oppenheim, Jet plume injection and combustion, SAE International doi: 10.4271/920414. (1992).

- [62]. N. Glasson, G. Lumsden, R. Dingli, and H. Watson, Development of the haji system for a multi-cylinder spark ignition engine, SAE International doi: 10.4271/961104. (1996).
- [63]. E. Toulson, H. C. Watson, and W. P. Attard, Gas assisted jet ignition of ultra-lean lpg in a spark ignition engine, SAE International doi: 10.4271/2009-01-0506. (2009).
- [64]. G. Lumsden and H. C. Watson, Optimum control of an S.I. Engine with a λ =5 capability, SAE International doi: 10.4271/950689. (1995).
- [65]. K. P. Grogan, S. Scott Goldsborough, and M. Ihme, Ignition regimes in rapid compression machines. Combustion and Flame, 162(8) (2015). 3071-3080.
- [66]. A. Shah, P. Tunestal, and B. Johansson, Effect of pre-chamber volume and nozzle diameter on pre-chamber ignition in heavy duty natural gas engines, SAE International doi: 10.4271/2015-01-0867. (2015).
- [67]. E. Murase and K. Hanada, Control of the start of hcci combustion by pulsed flame jet, SAE International doi: 10.4271/2002-01-2867. (2002).
- [68]. R. Sadanandan, D. Markus, R. Schießl, U. Maas, J. Olofsson, H. Seyfried, M. Richter, and M. Aldén, Detailed investigation of ignition by hot gas jets. Proceedings of the Combustion Institute, 31(1) (2007). 719-726.
- [69]. E. Silke, J. Simmie, and H. Curran, The effect of diluent gases in the shock tube and rapid compression machine, Lawrence Livermore National Laboratory (LLNL), Livermore, CA doi. (2007).
- [70]. M. J. Dunn, A. R. Masri, and R. W. Bilger, A new piloted premixed jet burner to study strong finite-rate chemistry effects. Combustion and Flame, 151(1–2) (2007). 46-60.
- [71]. Y. Chen and M. Ihme, Large-eddy simulation of a piloted premixed jet burner. Combustion and Flame, 160(12) (2013). 2896-2910.
- [72]. D. H. Rowinski and S. B. Pope, Pdf calculations of piloted premixed jet flames. Combustion Theory and Modelling, 15(2) (2011). 245-266.
- [73]. B. Cushman-Roisin, Environmental fluid mechanics. John Wiley & Sons Inc, 2014.
- [74]. J. D. Naber and D. L. Siebers, Effects of gas density and vaporization on penetration and dispersion of diesel sprays, SAE International doi: 10.4271/960034. (1996).
- [75]. C. G. Ball, H. Fellouah, and A. Pollard, The flow field in turbulent round free jets. Progress in Aerospace Sciences, 50 (2012). 1-26.
- [76]. H. Fellouah, C. G. Ball, and A. Pollard, Reynolds number effects within the development region of a turbulent round free jet. Int. J. Heat Mass Transfer, 52(17–18) (2009). 3943-3954.
- [77]. H. Fellouah and A. Pollard, The velocity spectra and turbulence length scale distributions in the near to intermediate regions of a round free turbulent jet. Phys. Fluids, 21(11) (2009). 115101.

- [78]. H. Fellouah, C. G. Ball, and A. Pollard, Reynolds number effects within the development region of a turbulent round free jet. International Journal of Heat and Mass Transfer, 52(17–18) (2009). 3943-3954.
- [79]. P. E. Dimotakis, The mixing transition in turbulent flows. J. Fluid. Mech., 409 (2000). 69-98.
- [80]. P. Hrycak, S. Jachna, and D. T. Lee, A study of characteristics of developing, incompressible, axi-symmetric jets. Letters in Heat and Mass Transfer, 1(1) (1974). 63-71.
- [81]. B. Hill, Measurement of local entrainment rate in the initial region of axisymmetric turbulent air jets. J. Fluid Mech, 51(4). 773-779.
- [82]. F. P. Ricou and D. B. Spalding, Measurements of entrainment by axisymmetrical turbulent jets. Journal of Fluid Mechanics, 11(01) (1961). 21-32.
- [83]. L. C. R. Johansen, E. de Benito Sienes, and P. Dahlander, Analysis of transient compressible gas jets using high speed schlieren imaging, SAE International doi: 10.4271/2013-01-0871. (2013).
- [84]. H. Hiroyasu and M. Arai, Structures of fuel sprays in diesel engines, SAE International doi: 10.4271/900475. (1990).
- [85]. M. P. B. Musculus and K. Kattke, Entrainment waves in diesel jets. SAE Int. J. Engines, 2(1) (2009). 1170-1193.
- [86]. N. Abani and R. D. Reitz, Unsteady turbulent round jets and vortex motion. Phys. Fluids, 19(12) (2007). 125102.
- [87]. H. Helmholtz, Lxiii. On integrals of the hydrodynamical equations, which express vortex-motion. Philosophical Magazine Series 4, 33(226) (1867). 485-512.
- [88]. D. C. Haworth, A review of turbulent combustion modeling for multidimensional incylinder CFD, SAE International doi: 10.4271/2005-01-0993. (2005).
- [89]. G. D'Errico, T. Lucchini, G. Hardy, F. Tap, and G. Ramaekers, Combustion modeling in heavy duty diesel engines using detailed chemistry and turbulence-chemistry interaction, SAE International doi: 10.4271/2015-01-0375. (2015).
- [90]. Openfoam. www.openfoam.org (accessed July. 2016).
- [91]. P. Boudier, S. Henriot, T. Poinsot, and T. Baritaud, A model for turbulent flame ignition and propagation in spark ignition engines. Symposium (International) on Combustion, 24(1) (1992). 503-510.
- [92]. O. Colin, A. Benkenida, and C. Angelberger, 3d modeling of mixing, ignition and combustion phenomena in highly stratified gasoline engines. Oil & gas science and technology, 58(1) (2003). 47-62.
- [93]. J. M. Duclos and O. Colin, (2-25) are and kernel tracking ignition model for 3d sparkignition engine calculations((si-7) S. I. Engine combustion 7-modeling). The ... international symposium on diagnostics and modeling of combustion in internal combustion engines, (1) (2001). 46.

- [94]. S. Falfari and G. M. Bianchi, Development of an ignition model for S.I. Engines simulation, SAE International doi: 10.4271/2007-01-0148. (2007).
- [95]. R. Herweg and R. R. Maly, A fundamental model for flame kernel formation in S. I. Engines, SAE International doi: 10.4271/922243. (1992).
- [96]. G. Mittal, M. P. Raju, and C.-J. Sung, CFD modeling of two-stage ignition in a rapid compression machine: Assessment of zero-dimensional approach. Combustion and Flame, 157(7) (2010). 1316-1324.
- [97]. G. Xu, C. Hanauer, Y. M. Wright, and K. Boulouchos, CFD-simulation of ignition and combustion in lean burn gas engines, SAE International doi: 10.4271/2016-01-0800. (2016).
- [98]. X. Yang, S. Gupta, T.-W. Kuo, and V. Gopalakrishnan, Rans and large eddy simulation of internal combustion engine flows—a comparative study. Journal of Engineering for Gas Turbines and Power, 136(5) (2014). 051507.
- [99]. K. Richards, P. Senecal, and E. Pomraning, Converge (version 2.2). Converge Science Inc.: Middleton, WI., (2014).
- [100]. E. Pomraning, K. Richards, and P. K. Senecal, Modeling turbulent combustion using a RANS model, detailed chemistry, and adaptive mesh refinement, SAE International doi: 10.4271/2014-01-1116. (2014).
- [101]. P. Chinnathambi, M. Bunce, and L. Cruff, RANS based multidimensional modeling of an ultra-lean burn pre-chamber combustion system with auxiliary liquid gasoline injection, SAE International doi: 10.4271/2015-01-0386. (2015).
- [102]. L. Brett, J. Macnamara, P. Musch, and J. M. Simmie, Simulation of methane autoignition in a rapid compression machine with creviced pistons. Combustion and Flame, 124(1–2) (2001). 326-329.
- [103]. Chemkin software. http://www.reactiondesign.com/products/chemkin/chemkin-2/ (accessed May. 2016).
- [104]. C. Allen, Advanced rapid compression machine test methods and surrogate fuel modeling for bio-derived jet and diesel fuel autoignition, doi. (2012).
- [105]. H. Schock, G. Zhu, E. Toulson, and T. R. Stuecken, Internal combustion engine, Google Patents doi. (2014).
- [106]. P. Sagaut Large eddy simulation for incompressible flows: An introduction. http://public.eblib.com/choice/publicfullrecord.aspx?p=304365.
- [107]. F. M. White, Fluid mechanics. New York: McGraw-Hill, 1986.
- [108]. G. Soave, Equilibrium constants from a modified redlich-kwong equation of state. Chemical Engineering Science, 27(6) (1972). 1197-1203.
- [109]. R. I. Issa, Solution of the implicitly discretised fluid flow equations by operator-splitting. Journal of computational physics, 62(1) (1986). 40-65.

- [110]. S. Som, P. Senecal, and E. Pomraning. Comparison of RANS and LES turbulence models against constant volume diesel experiments. in *ILASS Americas*, 24th Annual Conf. Liquid Atomization and Spray Systems.doi.(2012).
- [111]. V. Yakhot, S. A. Orszag, S. Thangam, T. B. Gatski, and C. G. Speziale, Development of turbulence models for shear flows by a double expansion technique. Physics of Fluids A, 4(7) (1992). 1510-1520.
- [112]. J. Blazek, Computational fluid dynamics: Principles and applications: (book with accompanying cd) (2). Jordan Hill, GB: Elsevier Science, 2005.
- [113]. S. B. Pope, Turbulent flows. Cambridge; New York;: Cambridge University Press, 2000.
- [114]. A. Leonard, Energy cascade in large-eddy simulations of turbulent fluid flows. Advances in geophysics, 18 (1975). 237-248.
- [115]. J. Smagorinsky, General circulation experiments with the primitive equations: I. The basic experiment*. Monthly weather review, 91(3) (1963). 99-164.
- [116]. R. A. Clark, J. H. Ferziger, and W. C. Reynolds, Evaluation of subgrid-scale models using an accurately simulated turbulent flow. Journal of Fluid Mechanics, 91(01) (1979). 1-16.
- [117]. J. W. Deardorff, A numerical study of three-dimensional turbulent channel flow at large reynolds numbers. Journal of Fluid Mechanics, 41(02) (1970). 453-480.
- [118]. R. Courant, On the partial difference equations of mathematical physics. IBM journal, 11(2) (1967). 215-234.
- [119]. P. K. Senecal, E. Pomraning, K. J. Richards, T. E. Briggs, C. Y. Choi, R. M. McDavid, and M. A. Patterson, Multi-dimensional modeling of direct-injection diesel spray liquid length and flame lift-off length using CFD and parallel detailed chemistry, SAE International doi: 10.4271/2003-01-1043. (2003).
- [120]. Uc san diego mechanism. http://web.eng.ucsd.edu/mae/groups/combustion/mechanism.html (accessed August. 2016).
- [121]. Aramco kinematic mechanism. http://c3.nuigalway.ie/index.html (accessed August. 2016).
- [122]. Gri mech. http://combustion.berkeley.edu/gri-mech/ (accessed October. 2016).
- [123]. http://c3.nuigalway.ie/naturalgas3.html (accessed September. 2016).
- [124]. N. Peters and F. A. Williams, The asymptotic structure of stoichiometric methane air flames. Combustion and Flame, 68(2) (1987). 185-207.
- [125]. S. Honnet, Detailed and reduced kinetic mechanisms in low-emission combustion processes, ed. G. Cuvilier Verlag. 2007.
- [126]. G. Mittal, M. P. Raju, and A. Bhari, A numerical assessment of the novel concept of crevice containment in a rapid compression machine. Combustion and Flame, 158(12) (2011). 2420-2427.

- [127]. T. Lu and C. K. Law, Strategies for mechanism reduction for large hydrocarbons: Nheptane. Combustion and Flame, 154(1–2) (2008). 153-163.
- [128]. B. C. Thelen and E. Toulson, A computational study of the effects of spark location on the performance of a turbulent jet ignition system, SAE International doi: 10.4271/2016-01-0608. (2016).
- [129]. J. Olofsson Lif vs. Chemiluminescence measurements for flame front studies. http://www.dantecdynamics.com/lif-vs-chemiluminescence-measurements-for-flame-front-studies.
- [130]. W. S. Rasband U.S. National institutes of health, bethesda, maryland, USA,. http://imagej.nih.gov/ij/index.html.
- [131]. S. R. Turns, An introduction to combustion, concepts and applications. McGraw Hill, 2000.
- [132]. J. Abraham, Entrainment characteristics of transient jets. Numer. Heat Transfer, (1996). Part A 30, 347.
- [133]. H. Schilichting, Boundary layer theory. McGraw Hill, New York, 1976.
- [134]. Y. Wakuri, Fujii, M., Amitani, T., Tsuneya, R., Studies of the penetration of fuel spray in a diesel engine. Bulletin of JSME, 3 (1960).
- [135]. N. Hay and P. L. Jones, Comparison of the various correlations for spray penetration, SAE International doi: 10.4271/720776. (1972).
- [136]. G. Gentz, B. Thelen, M. Gholamisheeri, P. Litke, A. Brown, J. Hoke, and E. Toulson, A study of the influence of orifice diameter on a turbulent jet ignition system through combustion visualization and performance characterization in a rapid compression machine. Appl. Therm. Eng., 81 (2015). 399-411.
- [137]. B. J. McBride, S. Gordon, and M. A. Reno, Coefficients for calculating thermodynamic and transport properties of individual species, NASA Technical Memorandum, 4513 doi. (1993).
- [138]. H. Pitsch, Unsteady flamelet modeling of differential diffusion in turbulent jet diffusion flames. Combustion and Flame, 123(3) (2000). 358-374.
- [139]. M. Gholamisheeri, B. C. Thelen, G. R. Gentz, I. S. Wichman, and E. Toulson, Rapid compression machine study of a premixed, variable inlet density and flow rate, confined turbulent jet. Combustion and Flame, 169 (2016). 321-332.
- [140]. G. Gentz, M. Gholamisheeri, and E. Toulson, A study of a turbulent jet ignition system fueled with iso-octane: Pressure trace analysis and combustion visualization. Applied Energy, 189 (2017). 385-394.
- [141]. B. W. Weber, C.-J. Sung, and M. W. Renfro, On the uncertainty of temperature estimation in a rapid compression machine. Combustion and Flame, 162(6) (2015). 2518-2528.
- [142]. E. L. Petersen, D. M. Kalitan, S. Simmons, G. Bourque, H. J. Curran, and J. M. Simmie, Methane/propane oxidation at high pressures: Experimental and detailed chemical kinetic modeling. Proceedings of the Combustion Institute, 31(1) (2007). 447-454.

- [143]. C.-J. Sung and H. J. Curran, Using rapid compression machines for chemical kinetics studies. Progress in Energy and Combustion Science, 44 (2014). 1-18.
- [144]. M. Germano, Turbulence: The filtering approach. Journal of Fluid Mechanics, 238 (1992). 325-336.
- [145]. Y. Kochar, J. Seitzman, T. Lieuwen, W. Metcalfe, S. Burke, H. Curran, M. Krejci, W. Lowry, E. Petersen, and G. Bourque. Laminar flame speed measurements and modeling of alkane blends at elevated pressures with various diluents. in *ASME 2011 Turbo Expo: Turbine Technical Conference and Exposition*.doi.(2011). American Society of Mechanical Engineers.